UNIVERSIDADE FEDERAL DE SANTA CATARINA

Juan Pablo Flórez Mera

ANÁLISE DA TRANSFERÊNCIA DE CALOR E MASSA EM UM TUBO DE CALOR EM CIRCUITO EM COBRE

HEAT AND MASS TRANSFER ANALYSIS OF A COPPER LOOP HEAT PIPE

Florianópolis
2016

Juan Pablo Flórez Mera

ANÁLISE DA TRANSFERÊNCIA DE CALOR E MASSA EM UM TUBO DE CALOR EM CIRCUITO EM COBRE

Esta Tese foi julgada adequada para obtenção do Título de "Doutor em Engenharia Mecânica", e aprovada em sua forma final pelo Programa de Pós-Graduação em Engenharia Mecânica da Universidade Federal de Santa Catarina.

Florianópolis, 21 de dezembro de 2016.
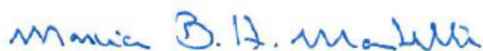
_____
Prof. Jonny Carlos de Silva, Dr.
Coordenador do Curso

_____
Prof. Márcia Barbosa Henriques Mantelli, Ph.D. – Orientador
Universidade Federal de Santa Catarina

_____
Prof. Fernando Henrique Milanese, Dr. – Coorientador
Universidade Federal de Santa Catarina

Banca Examinadora:
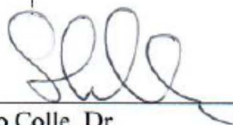
Márcia B. H. Mantelli

Prof. Márcia Barbosa Henriques Mantelli, Ph.D. – Presidente
Universidade Federal de Santa Catarina

Hélcio R. B. Orlande

Prof. Hélcio Rangel Barreto Orlande, D.Sc. - Relator
Politécnica /COPPE - Universidade Federal de Rio de Janeiro

PHDSantos

Prof. Paulo Henrique Dias dos Santos, Dr
Universidade Tecnológica Federal do Paraná

Sergio Colle

Prof. Sergio Colle, Dr.
Universidade Federal de Santa Catarina

Celso Peres Fernandes

Prof. Celso Peres Fernandes, Dr.
Universidade Federal de Santa Catarina

Kleber Vieira De Paiva

Prof. Kleber Vieira De Paiva, Dr.
Universidade Federal de Santa Catarina

ACKNOWLEDGEMENTS

"Now faith is the assurance of things hoped for, the conviction of things not seen"

Hebrews 11:1

RESUMO

O avanço tecnológico da microeletrônica permitiu o aumento da capacidade de transporte de informações dos microprocessadores e a redução do seu tamanho, tornando os computadores mais rápidos e menores. Porém, esses avanços apresentam consequências como uma maior taxa de produção de calor por efeito Joule, elevando a temperatura de operação desses componentes. Para garantir as condições de operação, são empregados dispositivos com capacidade de transferir grandes taxas de calor. Dentre estes dispositivos, se encontram os tubos de calor em circuito ou LHP's (*Loop Heat Pipes*). No segmento aeronáutico, devido ao crescente uso de equipamentos eletrônicos, as tecnologias de tubos de calor, mais especificamente de LHPs, têm sido cada vez mais utilizadas, pois são passivas, podem funcionar sem o auxílio da gravidade e transportam o calor a média e longa distância. As estruturas capilares que compõem estes dispositivos são fabricadas basicamente de materiais porosos metálicos, poliméricos ou cerâmicos. Para materiais metálicos sinterizados, diversos arranjos de materiais e estruturas têm sido testados, visando aumentar a capacidade de troca térmica do dispositivo. A grande dificuldade no emprego de materiais metálicos como o cobre é a possibilidade de se formar vapor no interior do meio poroso, bloqueando o fluxo de fluido de trabalho pelo dispositivo, causado pela elevada condutividade térmica do elemento poroso. Associada ao uso de materiais porosos sinterizados de cobre, é usada água como fluido de trabalho, por sua compatibilidade química e pelo maior número de mérito dentre os fluidos de trabalho mãos comuns. Porém, a água apresenta uma variação muito baixa da pressão de saturação com relação à temperatura, de forma que deve-se projetar evaporadores com pequenas perdas de carga e mínima transferência de calor parasita para a câmara de compensação. Se uma quantidade considerável de vapor é produzida na câmara de compensação, este permanece confinado, bloqueando total ou parcialmente o fluxo de fluido de trabalho, impedindo o fluxo de vapor no canal do evaporador e o retorno do condensado para a região de bombeamento capilar e, consequentemente, aumentando a resistência térmica total do dispositivo. Nesse trabalho foi realizada uma análise teórica e experimental da transferência de calor e massa em meios porosos sinterizados, considerando-se mudança de fase do fluido de trabalho no evaporador de tubos de calor em circuito. Modelos matemáticos para as propriedades termofísicas dos meios sinterizados de cobre, empregados

no evaporador de um LHP, foram propostos e comparados com dados experimentais. Nesta análise, foram estudados os parâmetros geométricos críticos para o projeto de um evaporador para um tubo de calor em circuito, considerando-se como parâmetro de entrada as características geométricas do material particulado utilizado na fabricação da estrutura capilar do meio poroso sinterizado do tubo de calor em circuito, assim como a temperatura de operação e a massa de fluido de trabalho.

Palavras-chave: tubo de calor em circuito, projeto de meios porosos sinterizados, controle térmico de dispositivos eletrônicos, modelagem matemática.

ABSTRACT

Technology advances in microelectronic systems lead to the development of high speed processing, with microprocessors of smaller sizes, which are ever lighter and faster. Conversely, these advances lead to the increase of the heat flux dissipation requirements. In this context, highly conductive heat transfer devices, able to remove the generated heat from electronic components, are required. Among these devices, heat pipes and loop heat pipes (LHP) are increasingly considered for the thermal management of electronic components. In aeronautics, where the use of electronic components has increased in the last decade, the heat pipes and loop heat pipes (LHP) are progressively being considered for thermal control due to the capacity to transfer large amount of heat, through short to considerable long distances, without the use of mechanical pumps or refrigeration systems. The wick structures that constitute these devices are basically made from metal, polymer or ceramic sintered porous media. Several arrangements have been tested for metal sintered porous media, in order to increase the heat transfer capacity of the LHP. The main concern of using copper is the possibility of blockage of the working fluid flow within the LHP, due to the presence of vapor inside the wick. Actually, due to the high thermal conductivity of porous media, vapor can be formed inside the wick, remaining confined, which can block fully or partially the working fluid passage along the evaporator. Associated with copper sintered porous media, water is selected as the working fluid due to its chemical compatibility with the copper and due to its large figure of merit in comparison to other working fluids. However, water presents a low variation of the saturation pressure as a function of temperature. This characteristic requires the design of evaporators with minimum pressure drop and minimum parasitic heat flows (heat leak) to the compensation chamber. Actually, an undesired heat leak to the evaporator compensation chamber may produce vapor, which may remain confined, fully or partially blocking the working fluid flow, and, consequently, increasing the total thermal resistance of the device. In this work, theoretical and experimental heat and mass transfer analyses of a copper sintered porous media, considering working fluid phase change, in a LHP evaporator, is developed. Mathematical models for the thermophysical properties of the copper sintered porous media were proposed and compared with experimental data. Analyses were performed on critical geometry parameters to LHP design, which

includes the geometry characteristics of the powder used in the sintered porous media fabrication, as well as the operating temperature and the working fluid mass.

ANÁLISE DA TRANSFERÊNCIA DE CALOR E MASSA EM UM TUBO DE CALOR EM CIRCUITO EM COBRE

Introdução

Os Tubos de Calor em Circuito (Loop Heat Pipes - LHP) e os Circuitos de Bomba Capilar (Capillary Pumped Loops - CPL) são dispositivos utilizados para transporte eficiente de calor. Uma de suas principais aplicações está no controle de temperatura de equipamentos eletrônicos, especialmente os localizados em satélites e aeronaves. Ambos são considerados variações da tecnologia dos tubos de calor clássicos, onde as regiões do evaporador e do condensador são separadas, hidraulicamente conectadas por pares de tubos, por onde circula apenas ou vapor ou líquido condensado. O bombeamento promovido pela estrutura capilar desloca o fluido de trabalho através do dispositivo e o vapor é transportado para a região do sumidouro de calor (condensador). As bombas capilares, que são estruturas responsáveis pelo bombeamento capilar do fluido de trabalho em LHPs, são fabricadas basicamente a partir de materiais porosos metálicos, poliméricos ou cerâmicos. Porém, em estruturas capilares metálicas, pode haver bloqueio do fluxo de fluido de trabalho através do meio poroso no interior do sistema de bombeamento capilar, devido à formação indesejável de vapor no seu interior. Na realidade, deseja-se que a formação de vapor ocorra em regiões próximas às paredes das bombas capilares, o qual deve escoar por ranhuras localizadas nesta região e projetadas para este fim. Porém, se o elemento poroso tem elevada condutividade térmica, pode-se formar vapor no interior deste meio, permanecendo confinado e bloqueando total ou parcialmente o fluxo do fluido de trabalho. Neste caso, o fluxo de vapor através do canal do evaporador é prejudicado, assim como o retorno do condensado para a região de bombeamento capilar. Desta forma, a resistência térmica total do dispositivo aumenta sensivelmente. Quanto menor o dispositivo, mais importante se torna este efeito.

A capacidade de transportar calor está diretamente relacionada à eficiência da estrutura porosa em proporcionar o transporte do fluido de trabalho, a qual por sua vez, depende da geometria do evaporador e de sua estrutura porosa. Neste contexto, modelos matemáticos, capazes

de predizer o comportamento térmico e hidráulico de bombas capilares, foram desenvolvidos nesta tese para o projeto de dispositivos eficientes.

Propriedades como condutividade térmica efetiva e permeabilidade do meio poroso estão intrinsicamente ligadas tanto aos limites de operação quanto às respostas térmica e hidráulica dos LHPs. Nesta tese também foram desenvolvidos modelos matemáticos que relacionam propriedades importantes do meio poroso, tais como: condutividade térmica efetiva, porosidade, permeabilidade, etc., com o diâmetro da partícula do pó de cobre utilizado na fabricação do meio poroso da bomba capilar. A curva de aquecimento empregada no processo de sinterização também é um parâmetro de entrada nestes modelos.

Finalmente, baseado nas ferramentas teóricas desenvolvidas na tese, foram projetados, construídos e testados dois tubos de calor em circuito. Os resultados experimentais apresentaram boa comparação com as predições dos modelos desenvolvidos nesta tese.

Objetivo

O principal objetivo desta tese é desenvolver uma análise teórica e experimental da transferência de calor e massa no evaporador de um tubo de calor em circuito, cuja estrutura porosa foi fabricada a partir de pó de cobre sinterizado, considerando-se mudança de fase no interior da estrutura e um fluido que satura o meio.

Metodologia

Esta tese está estruturada da forma apresentada a seguir.

Inicialmente são apresentados os princípios físicos fundamentais que regem o funcionamento de tubos de calor em circuito (LHPs). São discutidas as compatibilidades entre materiais e fluido de trabalho, assim como as condições termodinâmicas de operação. Posteriormente, uma descrição do processo de sinterização dos meios porosos estudados é apresentada. Amostras de pós de cobre metálicos que apresentam diferentes tamanhos de partículas, obtidas pelo processo de peneiramento de um pó de cobre comercial, foram empregadas na fabricação da estrutura sinterizada. Modelos matemáticos para a condutividade térmica efetiva, permeabilidade e do raio efetivo do poro do meio poroso sinterizado são propostos. Bancadas experimentais e equipamentos de medição são empregados para avaliar as propriedades

estudas e os resultados são comprados com os modelos experimentais desenvolvidos.

Na segunda parte, foca-se na modelagem térmica e hidráulica do evaporador e do LHP. Foi proposta uma expressão para calcular a relação crítica entre a espessura e o comprimento da camada de estrutura porosa no evaporador.

A descrição e a análise do procedimento de projeto do evaporador do LHP, com base nos modelos desenvolvidos são apresentadas. Um modelo matemático acoplado para determinar os campos da temperatura e da pressão é desenvolvido. As soluções analíticas das equações de conservação de massa, momento e energia utilizando o método de separação de variáveis são obtidas e a taxa de calor transferida para a câmara de compensação é calculada a partir de um balanço energético realizado sobre o modelo físico proposto. Baseados nos modelos desenvolvidos, dois LHPs foram projetados e construídos para trabalhar com água e metanol, respectivamente. Uma bancada experimental para avaliar o desempenho dos LHPs projetados é apresentada e os dados experimentais obtidos são comparados com as predições dos modelos.

Conclusões

Neste trabalho, foram desenvolvidos modelos para a previsão da distribuição de temperatura e pressão do material poroso usado como estrutura capilar, para um evaporador de LHP de forma cilíndrica. O estudo da estrutura porosa do evaporador nesta tese é composto por uma zona ativa de evaporação, isto é, um cilindro oco onde o calor da fonte de calor é transferido para a superfície de evaporação (menisco) e outro cilindro sólido que separa a câmara de compensação da a zona de evaporação.

Modelos matemáticos para a distribuição de temperatura, considerando geometria bidimensional (2D) e unidimensional (1D), foram desenvolvidos. Para o modelo de pressão, foi utilizada apenas uma abordagem bidimensional (2D). Os modelos térmico e de pressão 2D, acoplados, permitem a determinação dos parâmetros da geometria que garantem o desempenho correto do evaporador, isto é, sem a formação de bolhas de vapor dentro dos meios porosos. Deste estudo observou-se que os modelos 2D são ferramentas úteis para o projeto da estrutura porosa do evaporador do LHP, capazes de garantir um modo de operação seguro. No entanto, o modelo térmico 2D não considera a

perda de calor através da parede do evaporador, apenas através da estrutura porosa com a câmara de compensação.

Com base nos resultados 2D, que mostraram um comportamento muito próximo a fenômenos unidimensionais, tanto de distribuição de temperatura quanto de pressão, foi desenvolvido um modelo térmico 1D. Embora muito simples, este modelo, que faz uso da analogia entre circuito térmico e elétrico e permite contabilizar as perdas de calor do evaporador para a câmara de compensação e para a parede do evaporador, capturando o comportamento térmico real do evaporador. A distribuição de temperatura ao longo do condensador do LHP também foi obtida a partir deste modelo. Complementando a modelagem de um LHP, modelos de perda de pressão para fluidos, tanto monofásicos como de duas fases, também foram usados nas linhas de líquido, de vapor e no condensador.

Os campos de temperatura e pressão mostram que a interface entre o cilindro sólido e oco é a região crítica a ser controlada para garantir o perfeito funcionamento do LHP, uma vez que, quando a carga de calor é aumentada, é possível que temperaturas superiores às críticas sejam atingidas, formando assim vapor e reduzindo a taxa de transferência de calor, aumentando consequentemente a queda de pressão no interior da estrutura porosa do evaporador. Assim, avaliou-se a possibilidade de formação de bolhas no interior da estrutura porosa, em termos de temperatura e pressão, comparando estas condições com um critério de para determinar a formação de bolhas dentro da estrutura capilar (estudos de ebulição).

Uma expressão teórica do parâmetro de projeto de estruturas porosas, que determina condições satisfatórias de operação do evaporador do LHP, δ/l (espessura/comprimento do evaporador), a qual relaciona as propriedades termodinâmicas do fluido de trabalho com as propriedades termofísicas dos meios porosos, foi proposta para a determinação da espessura do evaporador. Dois LHPs foram projetados e fabricados para avaliar este critério teórico: um para operar com água e outro para operar com metanol. Os testes com os LHPs fabricados validaram o parâmetro crítico, mostrando que a equação proposta pode ser usada como ferramenta para a determinação da espessura do meio poroso em um LHP.

Para a concepção de um meio poroso sinterizado com propriedades desejáveis (porosidade, permeabilidade, raio efetivo do poro e condutividade térmica efetiva), foram propostos modelos, onde o parâmetro de entrada é o diâmetro médio de partícula utilizadas na fabricação do meio poroso sinterizado. O processo de sinterização foi

descrito utilizando modelos da literatura. Foi desenvolvido uma bancada experimental para medir as propriedades termofísicas e os dados obtidos foram comparados com valores teóricos, mostrando uma boa comparação.

Foi feita uma análise estatística para determinar o efeito principal dos parâmetros geométricos e da condutividade térmica efetiva sobre a resposta térmica da geometria de estrutura porosa proposta nesta tese. Dois tipos de pós foram selecionados para produzir quatro meios porosos diferentes, resultantes da combinação das relações entre os parâmetros δ/l e β/l, onde δ é a espessura da estrutura de porosa na zona ativa de evaporação, β é o comprimento da estrutura de porosa inferior que separa a câmara de compensação da zona de evaporação e l é o comprimento da zona ativa de evaporação. Uma análise de variância (ANOVA) para um intervalo de confiança de 95 %, mostraram que os parâmetros: condutividade térmica efetiva e relação δ/l, no intervalo $\delta/l_{\text{crítico}} < \delta/l < 1,2 \cdot \delta/l_{\text{crítico}}$, têm efeitos significativos sobre a resposta térmica (temperatura e perda de calor) da estrutura porosa do evaporador. Testes experimentais com um LHP operando com diferentes quantidades de fluidos, mostraram respostas coerentes com os inventários de fluido propostos para tubos de calor (HP) na literatura.

LIST OF FIGURES

LIST OF TABLES

NOMENCLATURE

Latin letters:

$a(z)$	[mm]	Radius
$A(z)$	[m]	Characteristic Length
A	[m^2]	Area
A_n	[m^2]	Normal area
A		Orthogonal function coefficients
B		Orthogonal function coefficients
B		Parameter of pressure drop model
C		Parameter of pressure drop model
C		Orthogonal function coefficients
C_p	[W/K]	Heat capacity
d	[m]	Diameter
d_f		Driving force
D_{os}	[m^2/s]	Coefficient of superficial diffusion
D_s		Pre- exponential coefficient of superficial diffusion
D		Orthogonal function coefficients
E		Parameter of pressure drop model
f		Single-phase friction factor
F		Parameter of pressure drop model
Fr		Froude number
g	[m/s^2]	Gravity

G	[kg/m^2.s]	Mass flux
h	[W/m^2.K]	Convection heat transfer
h_{lv}	[kJ/kg]	Latent heat of evaporation
h_e	[mm]	Height
H		Parameter of pressure drop model
k_b	[J/K]	Boltzmann's constant
k_{eff}	[W/m.K]	Effective thermal conductivity
k_l	[W/m.K]	Thermal conductivity of liquid
k_s	[W/m.K]	Thermal conductivity of solid
l	[m]	Length of wick
L		Coefficients of Fourier series
$\dot{m}$	[kg/s]	Mass flow
M		Coefficients of Fourier series
M	[kg]	Mass
N		Coefficients of Fourier series
Nc		Number of contact points
Nu		Nusselt number
P		Coefficients of Fourier series
P	[Pa]	Pressure
P_{cap}	[Pa]	Capillary pressure
P_{cc}	[Pa]	Pressure of the compensation chamber
P_e	[m]	Perimeter
Pr		Prandtl number

P_v	[Pa]	Pressure of evaporator
q	[W]	Heat
q_c	[W]	Heat transferred through the case
q_e	[W]	Heat transferred to evaporation section
q_H	[W]	Applied heat
q_ω	[W]	Net heat used to evaporate the working fluid
q_β	[W]	Heat transferred through the wick plug
q_s	[W]	Heat leak to compensation chamber
Q_s	[kJ/mol]	Energy of activation of superficial diffusion
Q		Coefficient of Fourier series
r		r- axis
r	[m]	Radius
R		Coefficient of Fourier series
R		External radius
R	[J/kmol.K]	Universal gas constant
Ra		Rayleigh number
R_e		Reynolds number
r_{eff}	[m]	Effective porous radius
R_h		Hydraulic resistance
R_h^l	[°C/W]	Thermal resistance of hemisphere liquid
r_m	[m]	Curvature radius of neck

R_p	[°C/W]	Neck thermal resistance
R_t	[°C/W]	Total thermal resistance
S		Coefficient of Fourier series
T	[K]	Temperature
T_{cc}	[K]	Temperature of the compensation chamber
T_v	[K]	Temperature of the evaporator
u	[m/s]	Velocity in z direction
u		Combined standard uncertainty
U		Expanded uncertainty
U		Coefficients of Fourier series
u_B		Standard uncertainty type B
u_m	[m/s]	Mean fluid axial velocity
v	[m/s]	Velocity in r direction
y		Y-axis
V	[m³]	Volume
V_{cc}	[m³]	Volume of the compensation chamber
V_{liq}	[m³]	Volume of liquid line
V_{loop}	[m³]	Volume of LHP minus volume of compensation chamber
V_w	[m³]	Porous volume of the capillary structure
w	[m]	Depth
W		Coefficients of Fourier series
We		Weber number

x		Quality of vapor
x		X-axis
X		Martinelli parameter
$\dot{x}$	[m/s]	Neck growing rate
y		Y-axix
Y		Ratio of the vapor-to-liquid only pressure
z		Z-axix
Z		Orthogonal function

Greek letters:

α	[m^2/s]	Thermal diffusivity
α	[rad]	Contact half-angle
β	[mm]	Wick bottom length
β	[K^{-1}]	Thermal expansion coefficient
γ		Eigenvalues
γ_s	[J]	Surface energy
Γ		Physical parameter of pressure model
δ	[mm]	Wick thickness
ε_m		Eigenvalues
ε		Porosity
ζ_m		Eigenvalues
η		Ratio $r/a(z)$

η_m		Eigenvalues
θ		Temperature variable
κ	[m^2]	Permeability
λ		a_1/a_0
λ		Eigenvalues
μ	[kg/m.s]	Dynamic viscosity
ν		Eigenvalues
ν	[m^2/s]	Kinematic viscosity
ν	[mm]	Wick total length
ξ	[mm]	Wick external radius
ρ	[kg/m^3]	Density
σ	[N/m]	Surface tension
τ		Eigenvalues
φ		Eigenvalues
φ	[mm]	Wick isolated length
ϕ		Pressure difference
χ		Eigenvalues
Ψ		Variable transformation
ω	[mm]	Wick internal radius
Ω	[m^3]	Atomic volume
Ω		Temperature variable

TABLE OF CONTENTS

1 INTRODUCTION

Advances in microelectronic systems, especially in computer related technologies, resulted in high speed processing, while the dimensions of the electronic components decreased, resulting in smaller, lighter and faster equipment. Conversely, these advances lead to the increase of the rate of heat dissipation per volume. Therefore, most of this thermal power must be removed to keep the operating temperatures within safe levels. In this context, high performance heat transfer devices, able to remove the excess of heat from electronic components, are required. Among others, heat pipes and related technologies have been increasingly considered for the thermal management of electronic devices for terrestrial and space applications.

Aeronautics is one area where the use of heat pipe technologies has augmented in the last decade, in modern airplanes are increasingly electric/electronic. Heat pipes and loop heat pipes (LHP) are gradually being considered for the thermal control of aircraft guidance and control electronic systems as well as for passenger amusement devices (e.g. video, internet, telephone, etc.).

Actually, heat pipes, and other related technologies, are able to transfer large amount of heat through short to considerable long distances, without the use of mechanical pumps or refrigeration systems, which could produce undesirable vibrations and maintenance.

Loop Heat Pipes can be considered a variation of the classic heat pipes. Their major characteristic is the separation between the evaporator and the condenser sections that are connected by tubes that conducts or liquid (condensate) or vapor. Figure 1 shows a schematic of the operation of a LHP, with a cylindrical evaporator and a finned tube condenser.
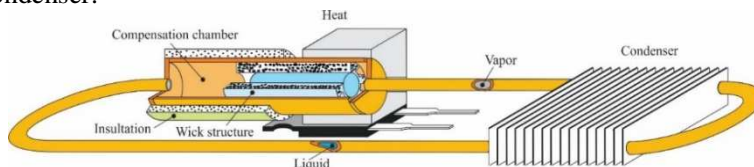
Figure 1 - Scheme of operation of a Loop Heat Pipe.

When heat is supplied to the evaporator, the working fluid within this region, which is in saturating condition, changes of phase from liquid to vapor and the resulting vapor flows to the condenser through a

vapor line. In the condenser, the heat is reject and the vapor changes phase from vapor to liquid and the condensate is conducted back to the evaporator through a liquid line, which, in turn, is connected to the compensation chamber (liquid reservoir attached to the evaporator) and, finally, to the evaporator, closing the loop.

The wick structure located in the evaporator provides the capillary pressure to pump the working fluid along the LHP. These capillary structures can be made from metal, polymer or ceramic materials. Maydanik *et al.* (2011b) show that LHPs in which wick structure is made of copper and water is the working fluid, achieved the highest capacity of heat power transfer. However, especially for this specific combination of materials, the design and fabrication of the evaporator wicks represent a challenge to the engineers, researchers and manufacturers. Due to the high thermal conductivity of porous media, vapor can be formed inside the wick, remaining fully or partially confined, blocking the working fluid inside the evaporator, resulting in the dry out of the LHP. In addition, an undesired heat leak from evaporator to the compensation chamber may increase the temperature and pressure of the working fluid, causing the collapse of the device. Besides, as the water presents high latent heat and high surface tension, a low variation of temperature can affect the pressure level of the working fluid, preventing the start-up of the device.

Actually, the heat transferred to the wick structure caused the working fluid phase change. To keep the structure full of liquid, the evaporated mass must be replenished by the porous media. Therefore, the capillary structure must have both characteristics: enough capillary pressure to guarantee the fluid pumping over the whole loop and enough permeability to allow the liquid to flow through the evaporator. Structures with small pores have high capacity of capillary pumping but reduced permeability. Overall parameters such as effective thermal conductivity, permeability and effective porous radius can predict the response of the wick structure for heat and mass transfer. One process used to manufacture these media is sintering of metallic powder. In this process, necks are formed among the contact points of the particles, providing the bonding among the particles, responsible for the mechanical and geometric characteristics of the wick. Also, through these necks, heat is conducted along the media. Therefore, the geometry of necks involves important parameters that depend on the media sintering temperature and on the size of the powder particles.

At this point, the following question arises: what is the best evaporator design that guarantees the performance of a LHP? The

design procedure must involve transport phenomena models (heat and mass transfer) and the selection of geometry of the wick structure. The resulting evaporator must satisfy the application requirements (temperature, geometry and heat transport capacity) and should guarantee that the device is able to transport the desired heat. This means that the evaporator must operate within its heat transfer limits, avoiding dry out. Models to be used as tools for the evaporator design should satisfy the first law of thermodynamic and so, must include the thermodynamic state of the working fluid. A global design scheme of an efficient LHP evaporator tool must contain the necessary models and their interactions with the operation requirements, including heat transfer limits and thermodynamic conditions, as presented in Figure 2.
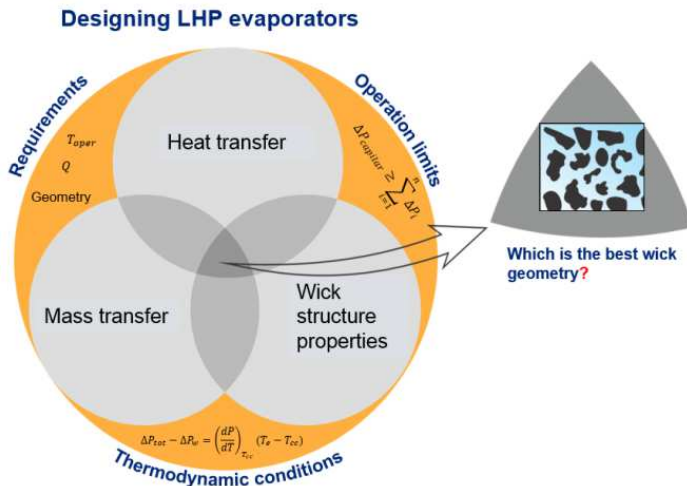
Figure 2 - Summary of the design of a LHP evaporator.

In this work, a simple geometry, easy to fabricate LHP is proposed. Theoretical and experimental heat and mass transfer models of a copper sintered porous media located in a LHP evaporator is developed. As a result, the critical design parameters of a LHP evaporator, including characteristics of the powder geometry, used in the fabrication of the wick structure, are determined. Through the characteristics of the metallic powder used, the thermophysical properties of the sintered porous media can be controlled. The performance of fabricated LHPs is compared with predictions of heat and mass transfer mathematical

models which input parameters are the thermodynamic properties of LHP component materials.

The first main focus of this thesis is on the analytical modelling the geometry characterization of the evaporator porous media, including the determination of the effective thermal conductivity, permeability and effective porous radius. Mathematical models are proposed to determine the thermophysical properties of the wick, taking the mean diameter of powder particles and the neck radius as the controlling parameters. The output of these models works as input of the thermal and hydrodynamic models that describe the thermal behavior of LHP evaporators.

Therefore, the second model is focused on analytical models, based on the conservation equations of mass, momentum and energy, which were developed for prediction of temperature and pressure fields within the porous media of the evaporator. Thermodynamic equilibrium relations are used to couple all the elements of the LHP studied. The objective of this model is to provide a tool for the design of evaporators of loop heat pipes able to transport the desired heat power at the desired temperature level.

Finally, based on the theoretical tools developed along the thesis, a LHP was designed, constructed and tested. The testing results were compared with the predictions from the model.

1.1 Objectives

1.1.1 General Objective

The main objective of this thesis is to perform a theoretical and experimental analysis of the heat and mass transfer of a LHP evaporator, which wick is made of sintering copper powder, considering phase change that happens within the porous media, considered saturated with working fluid.

1.1.2 Specific Objectives

In order to reach the general objective, the following specific objectives are proposed.

- To characterize the copper sintered porous media made from power with narrow distribution size particle.
- To determine the characteristic parameters of the powder used in the fabrication of the sintered porous media, to be used as wick structure of LHP evaporator.

- To develop a model able to predict the permeability, the effective thermal conductivity and the effective porous radius of the resulting porous media, which input parameter is the average diameter of the powder particle.
- To develop a mathematical model for predicting the heat and mass transfer within the wick structure of the LHP evaporator.
- To determine the critical geometry parameters for the design of the LHP evaporator.
- To design a LHP using the models and theoretical tools developed in this thesis.
- To evaluate the temperature of operation and the heat transfer capacity of a LHP designed, using the sintered porous media with controlled properties.

1.2 Thesis Organization

This work is presented as follows.

In chapter 1, a brief introduction of the present thesis subject and the objectives of the present work are presented.

In chapter 2, to introduce the subject of the present investigation, the LHP working principles are presented, as well as the physical characterization of the materials and the fluid used and their operating thermodynamic conditions.

In chapter 3, the descriptions of porous media and sintering processes are presented. Models for permeability, effective thermal conductivity and effective porous radius are presented. Careful sieving of a commercial powder resulted in different powders used for the fabrication of different sintered media. Several experimental set ups were constructed for this study; the test procedure is presented in details and the data obtained is compared with the theoretical results.

In chapter 4, an equation to calculate the critical relation between the length and thickness of the porous media layer in the evaporation region is proposed. Following, an experimental apparatus to evaluate LHP performance is presented and the experimental data obtained are compared with the equation predictions.

In chapter 5, the description and analysis of LHP evaporator design procedure, based on the developed models, is presented. A coupled mathematical model to determine the temperature and pressure fields are

developed. Analytical solutions of the conservation equations of mass, momentum and energy using the separation of variables method are obtained and the heat leak to the compensation chamber is calculated, from an energy balance performed over the proposed physical model. An experimental apparatus to evaluate LHP performance is presented and the experimental data obtained are compared with the model predictions.

It is important to note that the present thesis organization is "paper oriented" as several papers, corresponding to sections or chapters of this thesis were published in journals and/or presented in national and international conferences. Therefore, the literature review is not concentrated in only one chapter but divided according to the chapter subject. In Table 1, the published articles are listed and related with the chapters or sections of the present thesis. Actually, as one can note along this work, the organization within the chapters and sections follows the usual order of the related paper.

Table 1. Theses Content published in journals and conferences.

Related content	Bibliographic citation
Section 3.1	Powder Geometry Based Models for Sintered Media Porosity and Effective Thermal Conductivity. Journal of Thermophysics and Heat Transfer, v. 28, p. 1-11, 2014.
Section 3.1	Effective thermal conductivity of sintered porous media: Model and experimental validation. International Journal of Heat and Mass Transfer, v. 66, p. 868-878, 2013.
Section 3.1	Permeability Model of Sintered Porous Media: Analytical and Experimental. In proceeding: 8th International Heat Pipe Conference and the 12th International Heat Pipe Symposium in korei, June 12-16, 2016. Accept to publication in Journal Heat and Mass Transfer - Springer.
Chapter 4	Thermal Model for Sintered Cylindrical Evaporators of Loop Heat Pipes, 45th AIAA Thermophysics Conference, Aviation Forum 2015, American Institute of Aeronautics and Astronautics (AIAA), 22–26 June 2015, Dallas, Texas United States. Accept to publication in Journal of Thermophysics and Heat Transfer- AIAA.

2 HEAT PIPE TECHNOLOGIES WORKING PRINCIPLES

The objective of this chapter is to describe the physical working principles of the devices analyzed in the present thesis, more specifically heat pipes (HP) and loop heat pipes (LHP). More detailed literature reviews will be presented along the other chapters.

2.1 Heat pipes

Heat pipes (HPs) are devices with high capacity to transfer thermal energy, also known as "heat super conductors". These devices utilize the phase change of a working fluid to transfer heat from a source, like an electronic chip, transistor or computer processing unit, to a sink, such as the ambient, a fin-arrangement heat sink assisted by a fan, etc. Heat pipes are composed of a metallic case, internally lined with a porous media layer, which is filled with a working fluid. Heat Pipe is divided in three sections: evaporator, adiabatic and condenser (see Figure 3). When heat is supplied to the evaporator, the working fluid changes of phase. This vapor flows to the condenser through the internal channel. In the condenser section, heat is rejected and the saturated vapor within this section, changes of phase and the condensate flows through porous media back to the evaporator. Capillary pumping provides the driving force necessary to the condensate fluid to return to the evaporator. The capillary structure responsible for the working fluid pumping from condenser to evaporator, can be made from sintered porous media, metallic meshes or grooves.

Paiva and Mantelli (2015) developed and modeled mathematically a HP composed by diffusion welding of a sandwich of several parallel copper wires between two flat plates. Paiva and Mantelli (2015) proposed other more efficient design, using sintered porous media in the evaporator and copper wire flat plates in the adiabatic and condenser sections. This hybrid configuration increased the heat transfer capacity compared to sintered wick HPs. Operational tests in a notebook, assisted by this new technology HP, showed a reduction of 5.11 °C in the computer processor temperature, compared to the original device.

The volume of working fluid, inserted in a heat pipe, must be sufficient to saturate completely the capillary structure. Actually, high capillary pumping is obtained with small wick porous. However, small porous increase the liquid pressure drop and decrease the capacity of the liquid to flow through the porous media. Therefore, there is an optimal

wick design that combines high pumping capacity with pressure drop. Flórez *et al.*, (2012) fabricated and tested heat pipes using two layers of copper powder sintered wick structures, increasing the device heat transfer capacity. However, despite of the porous media improvements reported in the literature, the liquid pressure drop and the countercurrent liquid-vapor dragging forces limit the distance between evaporator and condenser. Loop heat pipes (LHPs) are proposed as HP technology alternative solution to increase the distance between evaporator and condenser. A description of the main principles of LHP operation is presented in the following section.
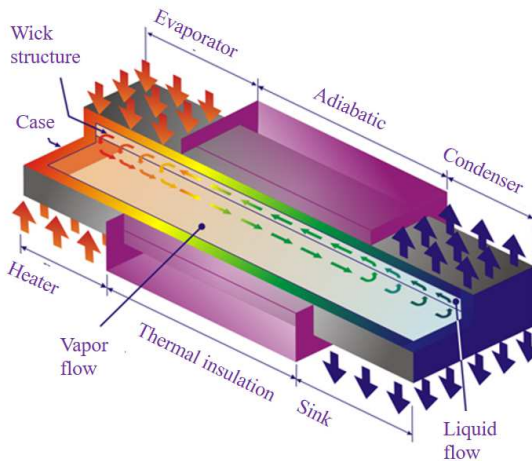
Figure 3 - Scheme of operation of a heat pipe.

2.2 Loop heat pipes

Loop heat pipe (LHP) is a variation of classic HPs. The main characteristic is these devices lies in the separation between the evaporator and condenser sections, that are connected by tubes where vapor from the evaporator and condensate liquid from the condenser are separately transported. In Figure 4, a flat plane evaporator LHP is shown.

In LHP, all the wick structure and therefore the pumping capacity of the device is located in the evaporator. This gives a higher geometrical flexibility for device. The vapor produced in the evaporator, where heat is delivered, is transported to the condenser section by vapor tubes, with a low level of perturbation. In the condenser section, in steady state

conditions, all the heat transported is delivered to the heat sink. It must be noted that the capillary structure across the entire extension of HPs actually limits the distance which the heat is able to be transported between the source and the sink. In LHPs, this distance can be increased and so the heat transport capacity.
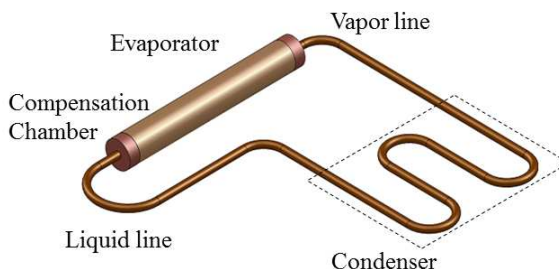
Figure 4 - Loop heat pipe.

One major characteristic for LHPs is the presence of a working fluid reservoir that ensures the constant supply of working fluid to the capillary pumping system. This reservoir is located beside the evaporator section and is commonly denominated as "compensation chamber" and, therefore, is joined thermally and hydraulic to the evaporator across a channel. LHP evaporator usually has geometry flat or cylindrical, as shown in Figure 5.

2.2.1 Working Fluid

Several factors must be considered in the selection of the working fluid to be used in heat pipes and loop heat pipes. According to Peterson (1994a), the range of temperature, vapor pressure, thermal conductivity, compatibly with material of wick structure, case, stability and toxicity are important aspects to be considered in the selection of the fluid in the design and fabrication stage. Reay and Kew (2006) presented data that describes the compatibility for same working fluid with different materials, typically used in heat pipes, which are summarized in Table 2. By compatibility, one understands the chemical reaction among the capillary structure, the casing material and the working fluid, which can cause the production of non-condensable gases.
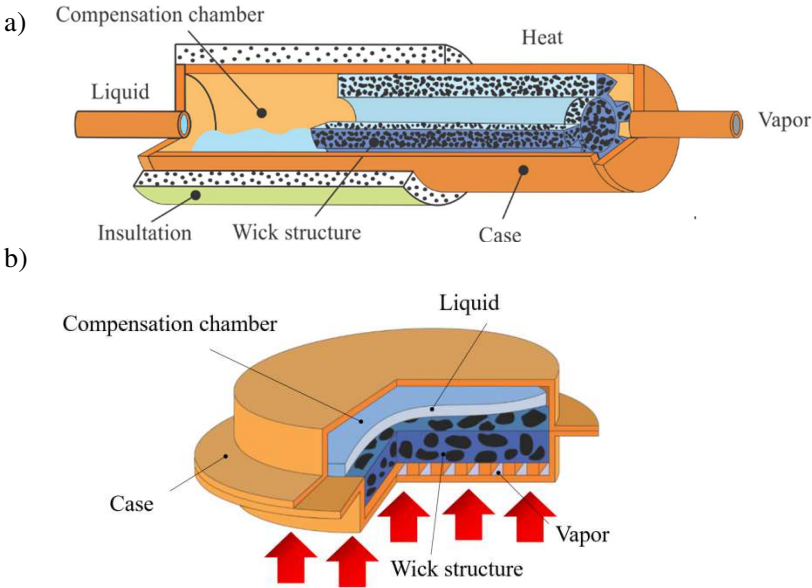
Figure 5 - Evaporator geometry a) cylindrical, b) flat.

Table 2. Fluid compatibility with wick and case materials.

Wick structure Material	Working fluid			
	Water	Acetone	Ammonia	Methanol
Copper	RE	RE	---	RE
Aluminum	GGC	RL	RE	NR
Stainless steel	GGT	PC	RE	GGT
Nickel	PC	PC	RE	RL
Fibra Refrasil	RE	RE	RE	RE

Source: Adapted from Dunn and Reay (1978).
RE, recommended by past successful usage; RL, recommended by literature;
PC, probably compatible; NR, not recommended; GNT generation of gas at
elevated temperatures, when oxide present.

Ku (1999) considers that the mass of working fluid M in cool condition, that is, without applied thermal load in the evaporator and condenser, at minimum temperature level must satisfy the following equation:

$$M = \rho_{l,c}\left(V_{loop} + \beta V_{cc}\right) + \rho_{v,c}(1 - \beta)V_{cc}, \qquad (2.1)$$

where V_{loop} is the total volume of LHP minus the volume of the compensation chamber, β is the fraction of compensation chamber occupied by liquid and $\rho_{l,c}$, $\rho_{v,c}$ are the densities of liquid and vapor, evaluated at minimum operation temperature. Also, the mass of fluid can be estimated at condition of the high temperature, using the equation:

$$M = \rho_{l,H}\left(V_{liq} + V_w + (1 - \alpha)V_{cc}\right) + \rho_{v,H}\left(V_{gr} + V_{vap} + V_{con} + \alpha V_{cc}\right), \qquad (2.2)$$

where V_{liq} is the volume of liquid line, V_w is the porous volume of the capillary structure, $\rho_{l,H}$ and $\rho_{v,H}$ are the densities of liquid and vapor, α is the fraction of free volume (not filled with liquid) in the compensation chamber. Once α e β are properly selected, the volume of compensation chamber can be calculated. In extreme conditions, LHP have to contain the amount of fluid equivalent to volume of liquid at maximum temperature in which the device starts the operation. This is mass can be calculated by:

$$M \leq \rho_{l,max}\left(V_{loop} + V_{cc}\right), \qquad (2.3)$$

where $\rho_{l,max}$ is the density of liquid at maximum LHP operation temperature. In literature, the LHP liquid load is related to its total volume. Singh *et al.*, (2009) tested a LHP with flat evaporator that operated normally with a working fluid volume ranging between 50 % and 80 % of the total volume of the device. The LHP presented dry out for fluid load below 50 % and the active area of condenser was not enough to remove the heat for a fluid load above 80 %.

2.2.2 Thermodynamic process

The thermodynamic states of the working fluid within a LHP can be represented in a pressure-temperature (PT) and pressure-specific volume diagram (Pv), as shown in Figure 6a and 6b, respectively. In the evaporator, the liquid evaporates at the meniscus (1). Actually, the

liquid-vapor meniscus, formed in the external surface of the wick structure, provides the capillary pressure drop, represented by the pressure difference between points (8) and (1) (Figure 6a), responsible for the liquid pumping along the LHP. The resulting vapor (2), which is in the superheated state, leaves the evaporator and flows through the vapor line duct (2-3). Also, the tube temperature levels decrease if the duct loses heat to the ambient. This happens if the tube external wall is not well thermally insulated and the ambient temperature is lower than the tube temperature. At point (3), vapor enters the condenser where heat is removed. Phase change starts when the vapor saturation state temperature is achieved. This is supposed to happen in the first section of the condenser (4-5). When the liquid leaves the condenser (6), the liquid is subcooled. Then, the condensate liquid flows through the liquid line and enters the compensation chamber (7). Then, the liquid flows through the porous structure (8) where it warms up, due to the heat input in the evaporator, reaching the liquid-vapor interface (1) in the meniscus, in the saturate conditions, closing the cycle. The fluid transportation within vapor and liquid lines generates pressure drops. A schematic representation of the LHP operation is shown in Figure 6c.

When the liquid reaches the liquid-vapor interface (8), the liquid is at the saturation pressure, corresponding to the local evaporator temperature. Actually, the heat transferred through the wick structure solid matrix is the responsible for the working fluid phase change. Therefore, saturation states 7 and 8 are thermodynamically linked and must satisfy the following equation (FAGHRI, 1995; KU, 1999; MAYDANIK *et al.*, 2011):

$$\Delta P = \frac{dP}{dT}\bigg|_T \Delta T, \qquad (2.4)$$

which also can be written as:

$$\frac{P_v - P_{cc}}{T_v - T_{cc}} = \frac{dP}{dT}\bigg|_{T_{cc}}, \qquad (2.5)$$

where P_v and T_v are the pressure and temperature of the evaporator, while P_{cc} and T_{cc} are pressure and temperature of the compensation chamber, respectively. The term dP/dT is the slope of the pressure-temperature saturation line at T_{cc} and this rate depends on the working fluid.
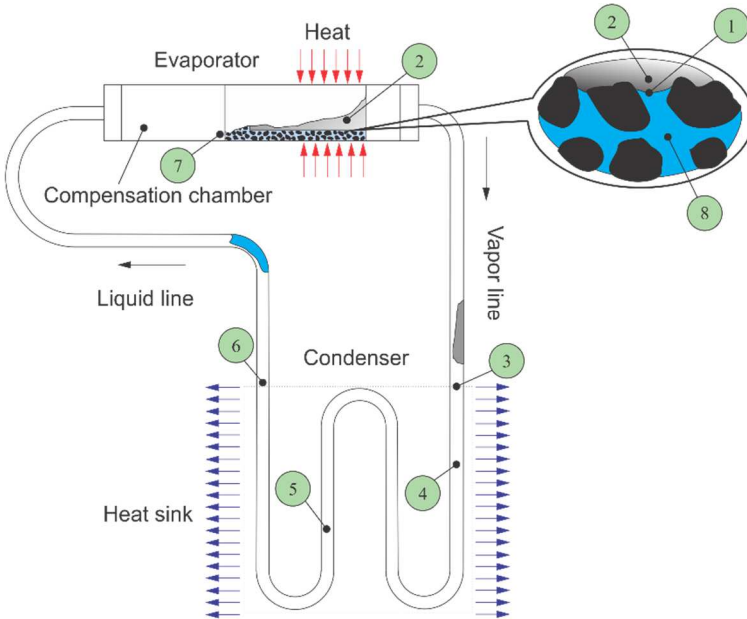
Figure 6 - a) Pressure-temperature diagram of LHP, b) Pressure- specific volume diagram, c) Schematic representation LHP operation.

2.3 Conclusions

In this chapter, the physical phenomena that drive the heat transport capacity of HP and LHP were presented. The understanding of the working principles is fundamental for the several models developed and presented in the subsequent chapters of this thesis.

3 CHARACTERIZATION OF SINTERED POROUS MEDIA: MODEL AND DATA

In the present thesis, sintered porous media are used as capillary structures in the fabrication of the evaporator in LHP. This structure provides higher capillary pump that usual mesh or grooved wick structures. In this chapter, an analysis of the fundamental parameters involved in sintered wick fabrication process as well as the effective thermophysical properties of the resulting porous media will be present. The study is focus on wick structures obtained using copper powder. Each subsection is formed of an introduction where definitions and literature review is presented. Consistently, a mathematical model is proposed with the objective of relate the properties study with the mean particle diameter as parameter of enter. Experimental setups fabricated and used in the measured of each property also are described. Finally, the results and conclusions are discussed, both proposed, and literature models are compared with experimental data.

3.1 Sintered process

Sintering is one of the techniques used to process particulate materials, aiming among other purposes, the fabrication of porous media. Thümmler and Oberacker (1993) describe the sintering as thermally activated material transport, which happens in a bulk of compacted powder, where the specific surface area is reduced by the growth of the contact between the particles. The neck size depends on parameters such as: rate of heating, time, temperature of sintering, particle material and mechanisms of mass transport.

The grain growth and the densification occur by means of the mass transport mechanism. Swinkels and Ashby (1981) divide the sintering process according to the transport mechanisms: surface diffusion, diffusion in the grain boundary and evaporation (see Figure 7). The grain boundary diffusion occurs due to defects in grain (vacancies, gaps and inconsistencies). According to these same authors, these transport mechanisms contribute to the growth of the neck but only the boundary and lattice diffusion contribute to the densification of the material. The sintering process can be divided in the following stages: formation and growth of the necks, densification and particulate material grain growth. Thümmler and Oberacker (1993) state that micro welding in the contacting areas within particulates form micro bridges (necks), which

size depends on the compression pressure. During the sintering, the shape of the sintered material does not change very much after compression.
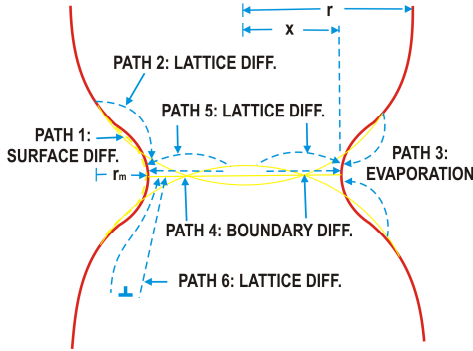
Figure 7 - Mass transport mechanism in sintering process.

Ashby (1981) affirms that the superficial diffusion is the dominant mechanism for copper powder sintering and propose the following expression to determine the neck growing rate, given by $\dot{x}$:

$$\dot{x} = 2D_s\delta_s \frac{\gamma_s\Omega}{k_B T} d_f^3 \tag{3.1}$$

where

$$D_s = \delta_s D_{os} e^{-\frac{Q_s}{RT}} \tag{3.2}$$

and where γ_s is surface energy, D_s is surface diffusion coefficient, D_{os} is the coefficient of the superficial diffusion, Q_s is energy of activation of the superficial diffusion, δ_s is effective superficial thickness, Ω is the atomic volume, k_B is the constant of Stefan-Boltzmann and T is temperature. d_f is considered as the driving force of the sintering process and can be calculated from the expression:

$$d_f = \left[\left(\frac{1}{r_m} - \frac{1}{x}\right) + \frac{2}{r}\right]\left(1 - \frac{x}{r}\right) \tag{3.3}$$

The factor $(1\text{-}x/r)$ is inserted to guarantee the validity of the model when the value of x approaches the sphere radius (ASHBY, 1981). An

expression relating the meniscus radius (neck curvature, r_n), the radius of spherical particles r and the neck radius x is:

$$r_m = \frac{1}{2}\frac{x^2}{1-x} \qquad (3.4)$$

3.2   Porosity

This section presents a mathematical model that relate the sintered porous media porosity with the particle average diameters and sintering temperatures, aiming its application in the design of capillary structures for heat pipes and loop heat pipes. Copper is the material employed in the present study, as it has been used as a typical wick material due to its good chemical compatibility with water (probably the most used working fluid in heat pipes) and due to the facility of manufacturing.

The literature recognizes that the porosity is an important parameter for modeling and designing heat pipes and loop heat pipes (FAGHRI, 1995; FLOREZ; NUERNBERG; PAIVA, 2012; MAYDANIK *et al.*, 2011; PETERSON; 1994) and usually links porosity with the effective thermal conductivity and permeability, especially for sintered porous media (ATABAKI; BALIGA, 2007).

Powder, with disperse particle size distribution, were separated through successive sieving to obtain narrow bands of particle sizes. Several sintered porous media made from these powders were fabricated and the porosity measured. The circularity of particles was measured to evaluate the influence of particle shapes in the resulting porous media. Experimental data is used in the comparison with the theoretical models.

3.2.1 Physical model

The powder particles from which the porous media is made are modeled as spheres of uniform radius r. Several packing configurations can be observed, when the same diameter spheres are in contact. In Figure 8, four packing configurations according to German (1989), are presented. These arrangements are employed to determine the theoretical porosity of a sintered porous media. The porosity is defined as the ratio between the empty volume (voids) and the total volume of a tridimensional box unit cell. The unit cell represents the particle packing and voids throughout the porous media for regular packing

arrangements. The unit cell edge corresponds to the line connecting the center of two adjacent spheres. In some arrangements, a sphere can be allocated in the center of the box. The spherical particles are mechanically bounded by means of a neck formed during the sintering process. The number of contact points in the box is determined according to neighbor spheres and depends on the packing arrangement considered. The edge angles of the "unit cell box" faces are represented in Figure 8.

a)   b)   c)   d)
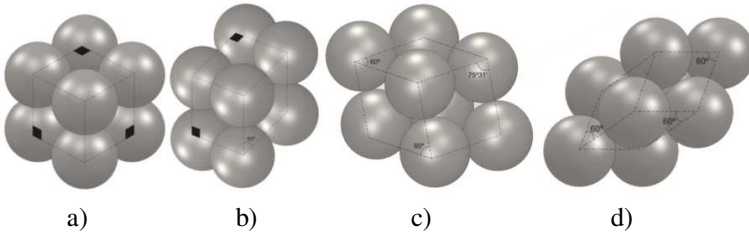
Figure 8 - Packing model. a)Cubic, b)Orthorhombic, c)Tetragonal, d)Rhombohedric.

The following hypotheses were adopted:
- Sintering process shrinkage is not considered. In the initial sintering stage, neck growth occurs and superficial mass diffusion is the dominant mass transfer mechanism (KANG, 2005).
- The sintered porous media is considered isotropic; thus the porosity is the same in all directions.
- Cubic packing scheme is adopted for modeling the porosity (Figure 8a).

3.2.2 Mathematical model

The porosity is calculated as the ratio between the void and bulk volumes of the unit cell. The void volume is calculated by subtracting from the volume of one cell, the volume corresponding to one sphere (two hemispheres) and half the volume of the necks (one neck for each sphere contact, according to packing scheme considered). Table 3 presents the literature expressions for the determination of the unit cell volume for each packing arrangement and the number of contacting spheres.

Table 3. Characteristics of packing of uniform spheres.

Packing	Volume of unit cell	Number of contact points Nc
Cubic	d^3	6
Orthorhombic	$\frac{\sqrt{3}}{2}d^3$	8
Tetragononal-sphenoidal	$0.75d^3$	10
Rhombohedral	$\frac{1}{\sqrt{2}}d^3$	12

Source: Adapted from Cooke and Rowe (1999).

For example, to calculate the porosity for a cubic packing arrangement, where each sphere particle has 6 neighboring particles, the porosity is calculated using the following expression:

$$\varepsilon = \frac{V_t - V_s - \frac{N_c}{2}V_n}{V_t} \tag{3.5}$$

where V_t is bulk volume, V_s is the solid volume and V_n is the neck volume determined as:

$$V_n = \pi \int_{z_1}^{z_2} r(z)^2 dz - \frac{1}{3}\pi h^2 (3r - h) \tag{3.6}$$

where the first term represents the volume of a revolving solid about its longitudinal axis of radius $r(z)$ over the interval $[z_1, z_2]$ and the second term represents the portion of the volume of a sphere, cut off by a plane in z_1 and z_2 heights. Supposing $r(z)$ constant, the neck geometry approaches to that of a disk of radius r_n:

$$r(z) = r_n \approx \frac{x}{2} + \frac{r}{2}\left(\frac{x - r_m}{r - r_m}\right) \tag{3.7}$$

On the other hand, h is defined as:

$$h = \frac{z_2 - z_1}{2} \tag{3.8}$$

This parameter can be expressed in terms of r and r_m, yielding:

$$h = r\left(1 - \frac{r}{r + r_m}\right) \tag{3.9}$$

Therefore, the Equation (3.6) can be written as:

$$V_n = 2\pi h r \left[\frac{x}{2} + \frac{r}{2}\left(\frac{x + r_m}{r + r_m}\right)\right]^2$$
$$- \frac{\pi}{3}\left[r\left(1 - \frac{r}{r + r_m}\right)\right]^2 \left(3r \right. \tag{3.10}$$
$$\left. - r\left(1 - \frac{r}{r + r_m}\right)\right)$$

Using this expression and the well know expressions for the determination of the sphere and cube volumes, one can easily determine the porosity using the Equation (3.5). This model can be adjusted by adding information of particle shape such as the circularly factor. The powder particle shape depends basically of the manufacture process. The powder copper used in this work is obtained by atomization process in water. In this process, the particles obtained presents irregular form. Images obtained by electronic microscopy of the copper powder show that smaller particles present circularly factor closed of 1 and decreases as size increases.

3.2.3 Experimental procedure

Atomized copper powder was employed during this study. Copper sintered porous media was selected as the object of the present study due to its chemical compatibility with water and its facility of manufacture as mentioned above. This material was employed in fabrication of samples, where the porosity and effective thermal conductivity were measured and presented in this study. Tests were conducted to determine the content of copper in the composition of the particulate material and a percentage of 95.45 ± 1 % of copper were observed. According to the ASM (1990) tables for pure copper and its alloys, the composition of the powder is similar to the copper alloy C21000, which has the thermal conductivity of 234 W/(K·m) at 20 °C. Physical properties of copper, provided by Swinkels and Ashby (1981) and shown in Table 4, where employed in the present work.

Particles of different sizes were obtained from successive mechanical vibration siftings of atomized copper powder obtained in the market and known commercially as PAM. The sieving process was conducted in equipment in batches with 300 g mass of powder PAM, during three hours. A set of sieves of mesh ASTM 100,150,250,275,300, 400 and 500 were employed.

The characterization of the particle size was made by laser granulometry, using the Fraunhofer diffraction method and the equipment Mastersizer 2000. Figure 9 presents the particle size distribution for PAM copper powder.
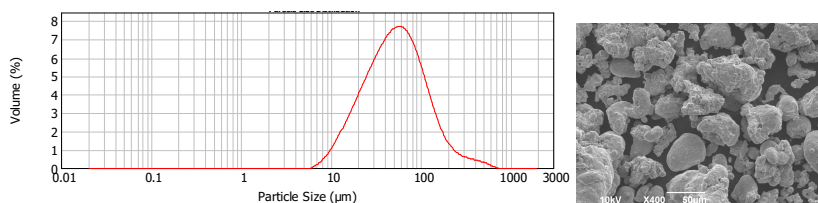
Figure 9 - Copper powder PAM. a) Particle size distribution by Fraunhofer diffraction method. b) Electronic microscopy image of powder x400.

Table 4. Physical properties of copper.

Properties	
Surface energy [J/m²]	1.72
Atomic volume [m^3]	2.56×10^{-10}
Pre-exponential coefficient, surface diffusion [m^3/s]	6×10^{-10}
Energy of activation of superficial diffusion [kJ/mol]	205
Melting temperature [K]	1356
Boltzmann´s constant [J/N]	1.38×10^{-23}

Sourde: Adapted from Swinkels and Ashby (1981).

Image analyses was employed to determinate the porosity of each sample. The image processing can be basically separated into four steps: image acquisition, preprocessing, segmentation, pattern recognition, and quantification. Mathematically, a monochrome digital image is represented by a function $f(x,y)$ of luminous intensity of gray levels of each point(pixel) image. The software counts the number of black (solid particles) and white (voids) pixels, allowing the calculation of porosity, according to the percentage area of each phase in the image. The software ImagemJ® was used to determine the porosity. The tested

samples have cylindrical geometries, with radio of 20 mm and thickness of 3 mm (see Figure 10). Each sample was made using a loose powder sintering process. The sample was deposited inside a cast made by stainless steel 304, as cooper has no chemical interaction with stainless steel, which facilitates the copper sample removal from the stainless steel casing. The sintering process was conducted in a vacuum (0.1 Pa, approximately) furnace with a controlled atmosphere of commercial H_2. The heating rate was 5 K/min until the sintering temperature is achieved, in which level the samples stayed for more than 3000 s. The specimens were embedded in acrylic resin by vacuum impregnation, to preserve the porous structure integrity. Without the impregnation process, the porous structure could be deformed, during the polishing step. The porous media samples were submitted to a metallographic process, to get a flat surface free of scratches, so that the acquisition of appropriate images by optical microscopy (OM) was possible. Surface Preparation was performed in two operations, following the recommendations of ASM (1990): rough polishing, where 400, 600, 1200 and 4000 grit, with water as the vehicle and a wheel speed of approximately 200 rpm were employed; and finish polishing, where finer alumina (Al2O3) 0.3-µm on napped cloths are used. After polishing, the specimen is rinsed in water and dried with warm air. This process was used to obtain a better digital image quality as surface scratches produce inaccuracies when porous media properties are measured employing image analysis. The digital image analysis was performed with a reflected light microscope at the Characterization Materials Laboratory (LCM/UFSC - Brazil). Digital images were taken from 20 different regions of each sample, using objective lenses at magnifications of 50, 100 and 200 times. The measuring uncertainties were calculated from the standard deviation of the 20 measurements.
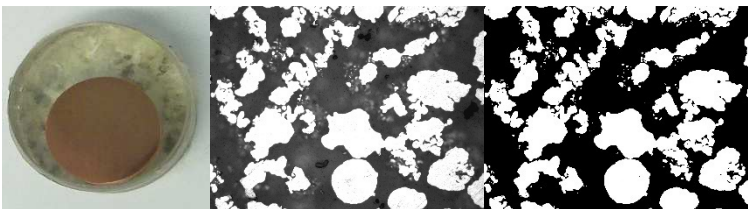
Figure 10 - Measurement of porosity. a) Sintering sample. b) Optical microscopy image of powder PAM x200. c) Binary image.

3.2.4 Results and conclusions

Figure 11 presents the particle size distribution and the binary images corresponding to each of the particles studied in this work. As already mentioned, the size of the particles was obtained by sifting atomized copper powder, resulting in particle sizes classified as A, B, C, D, E and F, in increasing mean particle diameter order. The Figure 11 x-axis represents the equivalent spherical diameter of particles (in micrometers) and the y-axis represents the percentage (in volume) particles corresponding to the x-axis entry. The distribution functions of all types of powder analyzed showed a similar behavior, following a typical normal distribution. However, powder A presents a bimodal distribution. Actually, the present paper authors believe that this effect is due to the agglomeration of particles, as small particles present high free energy due to the high superficial area in relation to its volume, which produces particle cohesion. Figure 11 also presents, in the right side, binary images of the porous media made of the powder characterized at the left side. These images were obtained from an optical microscopic and processed by the software ImagenJ®. As already mentioned, in these images, white represents the sintered powder and black the pores. Binary images show that increasing the particle diameter also increases the porosity of sintered media. One should note that these media were sintered at a temperature of 850 ºC.

Figure 12 presents a comparison between the experimental data and the predictions of the porosity proposed model, considering the four-packing structure as shown in Figure 8, as a function of the particle mean diameter. One can note that the experimental porosity tends to an approximately constant value for particles of diameter larger than 50 μm. For porous media made from small particles (diameter smaller than 50 μm), the porosity decreases, reaching a value of 0.30. Form this figure one can also note that the model based on sphere packing tends quickly to a constant porosity value, as the influence of the necks volume decreases as the particle increases and so, the packing void volume tends to a constant number which leads the porosity to reach a value of around 50 % for the cubic arrangement model. Observing Figure 12 one can conclude that cubic packing is the best theoretical particle arrangement configuration, as it presents the best comparison with data, with an average difference between data and model of about 18.8 %.
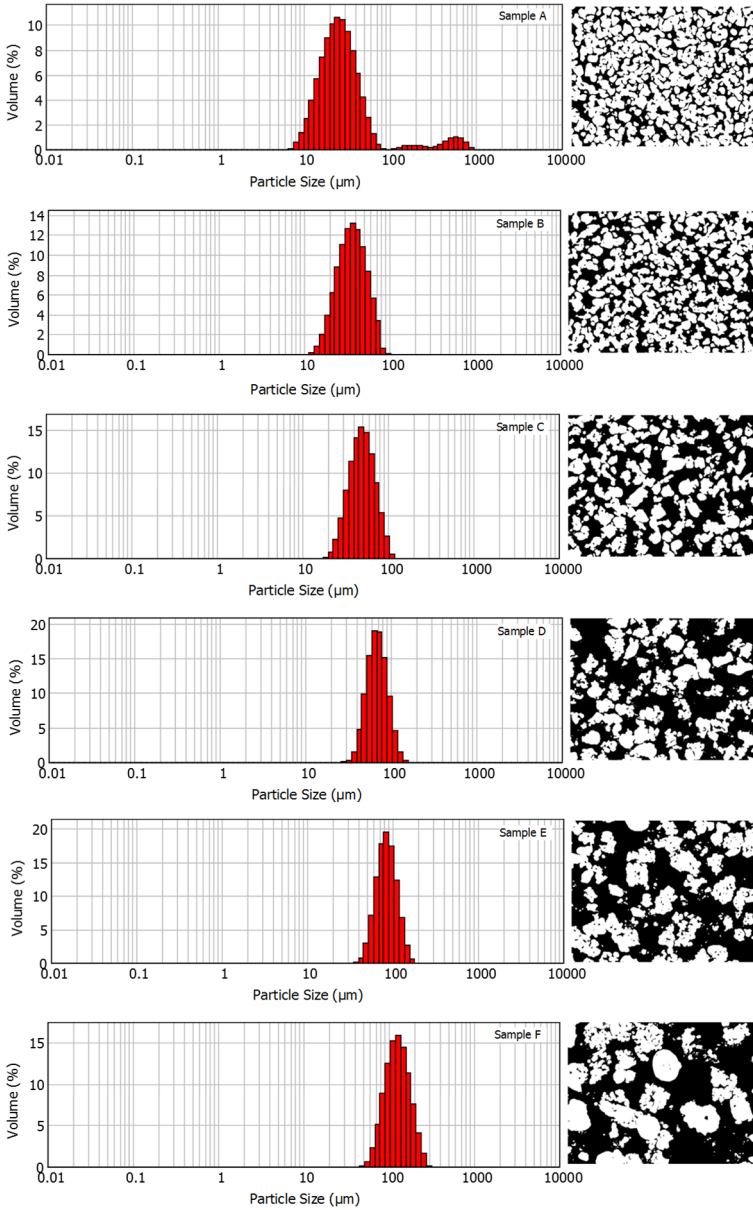
Figure 11 - Particle size distribution from Fraunhofer diffraction method for powders A, B, C, D, E and F (from top to bottom, left side) and binary image of sintered copper powder x200 (right side).

The image obtained from electronic microscopy MEV, for powder PAM, shows a particle circularly factor of 0.74. The circularly factor changes with the particle size as shown in Figure 13a.

In Figure 13a, a plot of the porosity as a function of the average particle diameter, in micrometers, for powders A, B, C, D, E and F is presented. Powder A showed a circularly factor of 0.85 while other powder was approximately 0.71. Actually the particles are non-circular and so, the perfect sphere lattice model may not be an accurate physical model for the porosity of the media. Therefore, the theoretical model may be adjusted to include the effect of particle non-circularity by a correction factor of 0.71 in equation (3.5). The present author acknowledge that the circularly factor may not be representative of all atomized particles as their geometry can change with the powder fabrication parameters, but, on the other hand, they are comfortable in proposing this circularity correction factor, as the particle images observed in this work are very similar to those published in literature (LAWLEY, 1992).
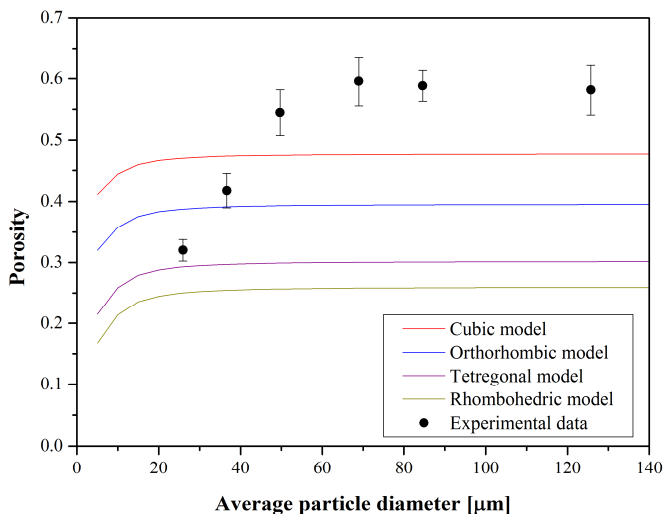
Figure 12 - Porosity models without circularly factor.

Figure 13b presents the adjusted theoretical model inserting a circularly factor in term associated to sphere volume in Equation (3.5). In this figure one can see that the data now compares well with the cubic

and orthorhombic packing models, for diameters larger than 50 µm. Other important aspect in packing particles to consider is the variation of the particle diameters in the powder used for sintering. Small particles with diameters equal or smaller than the interstices left by the larger particles can be accommodated within these interstice spaces, reducing porosity. Also particle geometric characteristics such as roughness, prevent the spreading of particles during the powder deposition, resulting in media with scattering formation.

a)

b)
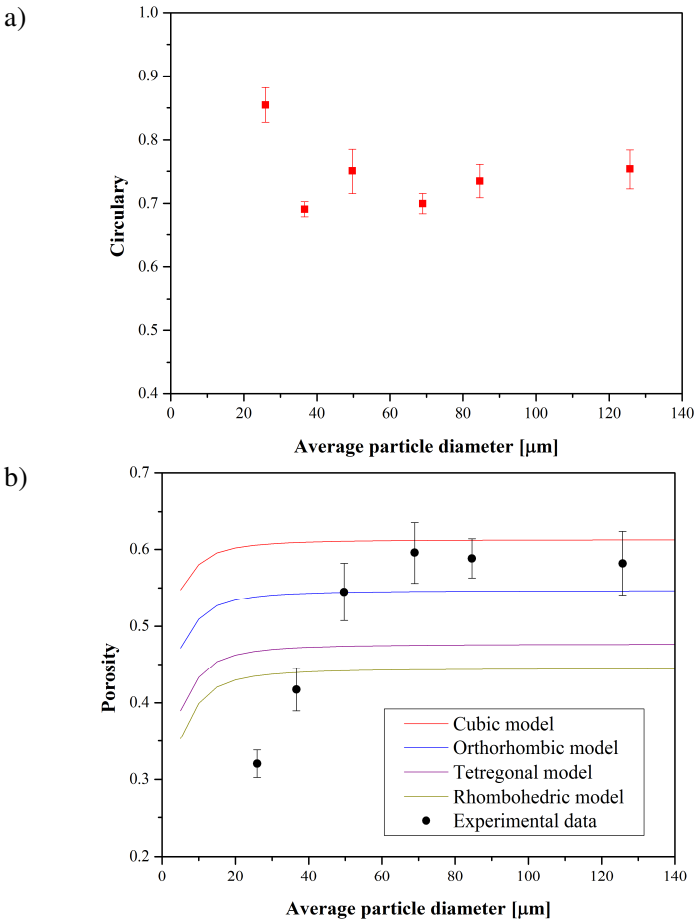
Figure 13- a) Circularly factor measured to samples of powder copper. b) Adjusted porosity model by circularly factor.

3.3 Effective thermal conductivity

Effective properties are usually used to define the physical characteristics of the porous materials. The effective thermal conductivity, for instance, is determined considering the thermal conductivity of the constituent phases of the material, i.e, the solid phase (matrix) and the fluid phase (liquid or gas).

Much of the heat transfer work in the literature treats all porous media equally, independently of the technology employed for their fabrication. Actually, there is a large difference among porous media produced by different technologies, as observed in sintered and bed packed metal powder. Usually, a distinction is made between the thermal conductivity of densified (or sintered) and not densified porous media. Carson *et al.* (2003) and Atabaki and Baliga (2007) verified that the thermal conductivity of a non-sintered material is much smaller than that of sintered materials.

In literature, an interesting model for the effective thermal conductivity based on experimental data was proposed in the PhD thesis of Alexander (1972) for metal felts, sintered powders, layers of wire cloth and unconsolidated beads. Sintering is also used in screens to produce heat pipe capillary structures. Atabaki and Baliga (2007) took literature models for non-sintered porous media (just packing spheres) and, by comparing with experimental test data, proposed a correlation for sintered porous media.

Although Birnboim, Olorunyolemi and Carmel (2001), in their numerical study related the effective thermal conductivity with the fabrication process and modeled porous media as spheres in thermal contact, it can be affirmed that, in general terms, the literature theoretical models lack to associate the effective thermal conductivity with process fabrication parameters, such as: sintering temperature, particle size and geometry of the ceramic powder particles.

In this work, the physical association among effective thermal conductivity, porosity and mean diameter of the particle used for the fabrication of sintered porous media is analyzed. The analogy with electrical circuits was used to model the effective thermal conductivity, which physical model consists of two hemispherical particles joined by a neck, with a fluid layer around them. Thermal resistances are associated with the heat transfer paths of the unit cell, so that an expression of the effective thermal conductivity is obtained.

Powder, with disperse particle size distribution, were separated through successive sieving to obtain narrow bands of particle sizes. Several sintered porous media made from these powders were fabricated and the porosity measured. The circularity of particles was measured to evaluate the influence of particle shapes in the resulting porous media. Experimental data is used in the comparison with the theoretical models.

3.3.1 Physical model

The physical model adopted to determine the theoretical effective thermal conductivity of a sintered porous media is displayed in Figure 14. The model is based on the thermal analysis of a unit cell, which represents the whole porous media. The actual porous media can be reproduced by stacking several of these cells in a vertical arrangement and replicating this pile in a horizontal array, forming a three-dimensional structure, according to several possible packing models as shown in Figure 8. As it will be explained later, in the present work, this cell applied to a cubic arrangement (Figure 8a). The cell is formed by two metal hemispheres of radius r. The hemispheres represent half of a solid metal particle of the powder from which the porous media is made. These radiuses are considered equal and equivalent to the powder mean radius. The hemispheres are joined by means of a neck formed during the sintering process. A stationary liquid film, in a hollow hemisphere shape, is considered around the hemispheres. x is the radius of the neck, given by the distance between the sphere contacting point and the neck outer radius, in the plane tangent to the contacting point. r_m is the radius of the meniscus formed by the neck, in the plane which contains the center of the spheres (see Figure 14). The rectangular coordinate system origin is located in the center of one of the hemisphere with the abscissa crossing both the sphere centers. The empty space between adjacent cells is filled with stagnant liquid film in such a temperature level which allows one to neglect the heat exchanged with the solid hemispheres and within the liquid film.

a)

b)
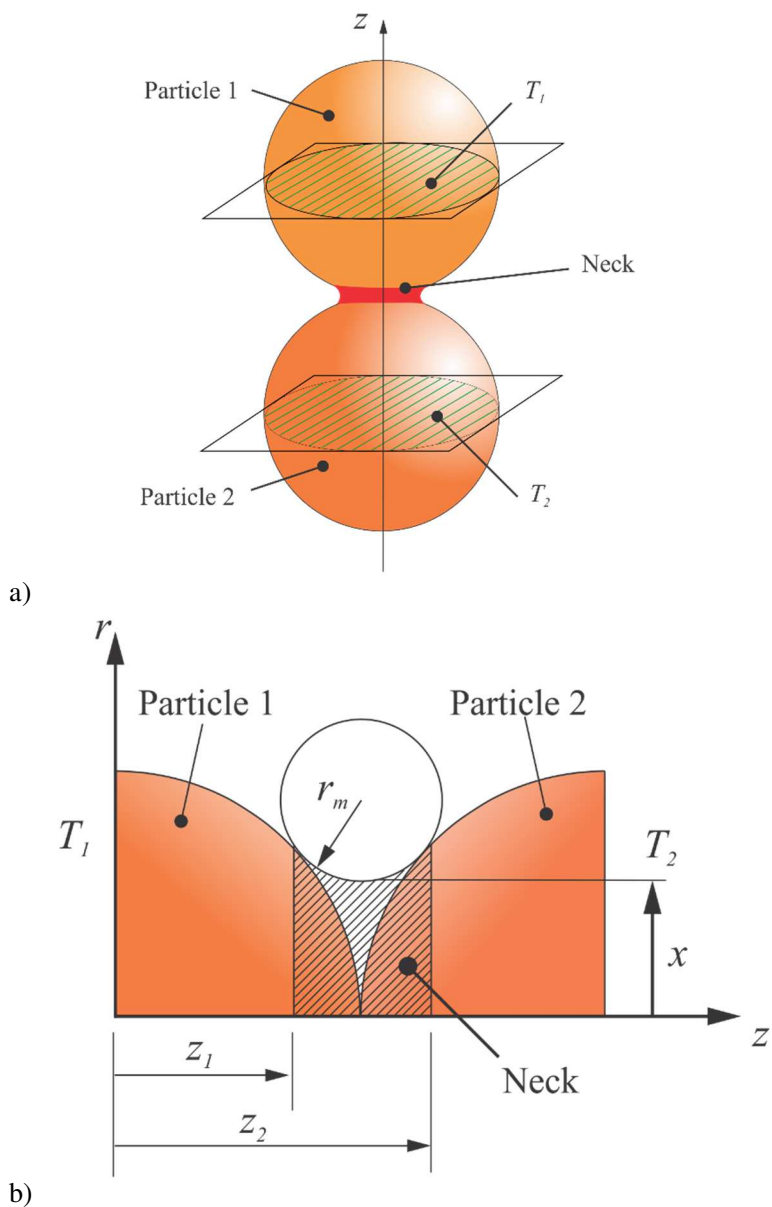
Figure 14 - Effective thermal conductivity: a) two powder particle spheres in contact, b) physical model. .

All the geometric parameters must be determined as a function of r, which represent the size of the particles that compose the powder used for the porous media fabrication. These diameters are obtained from the statistical treatment of the distribution dimensions of particles. The radius of neck is calculated from the sintering curve theory. The effective thermal conductivity of porous media is calculated from a heat balance, where the following hypotheses were adopted:

- Steady state.
- Planes perpendicular to the plane shown in Figure 14 are isothermal.
- Thermal equilibrium in the solid-fluid interface.
- Solid and fluid constant properties.
- The fluid layer surrounds and wets completely the particles. The fluid layer is considered stagnant; therefore, convective effects are neglected.
- Prescribed temperatures T_2 and T_1, where $T_2 > T_1$, are imposed to the two borders of the cell (see Figure 14)
- All powder particles have spherical shape, have the same radius and are statistically represented by the mean diameter.
- The neck has circular shape in the plane perpendicular to the heat flux.
- Compaction external forces and phase change are not considered.

3.3.2 Mathematical model

The analogy between thermal and electrical circuits is used to model the effective thermal conductivity of the elementary cell just described. The resulting thermal circuit, consisting of two resistances in parallel, is present in Figure 15. In this figure, the thicker arrow refers the lower resistance path where larger amount of heat is transferred, while the thinner arrow refers to the large resistance path, where lower amount of heat is transferred. The first path is associated with the resistance due to the conduction heat transfer through the hemispheres (constriction resistance R_h^s), in series with the neck R_p^s resistance. The other path is associated with the static fluid surrounding the spheres (R^l) and includes the resistance of the disk formed by the fluid in the neck (R_p^l). This last

resistance is considered negligible. The *s* superscript refers to solid and *l* to liquid. The overall resistance of this circuit is determined by:

$$R_t = \cfrac{1}{\cfrac{1}{R_{h1}{}^s + R_{h2}^s + R_p^s} + \cfrac{1}{R^l}} \tag{3.11}$$
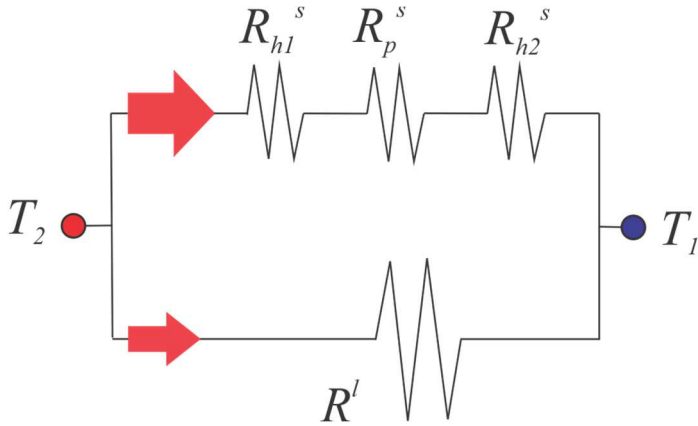
Figure 15 - Thermal equivalent circuit modeling the effective thermal conductivity.

Flórez *et al.* (2013) measured the effective thermal conductivity of sintered copper porous media saturated with water, air and at vacuum. They concluded that the liquid resistance is much larger than the solid resistance and, therefore, the liquid resistance path can be removed from the circuit, resulting in:

$$R_t = R_p{}^s + R_h{}^s \tag{3.12}$$

The effective thermal conductivity can be estimated, based on the linear approximation of the Fourier equation. For a unit cell, one gets:

$$k_{eff} A \frac{(T_2 - T_1)}{L} = \frac{(T_2 - T_1)}{R_t} \tag{3.13}$$

which gives:

$$k_{eff} = \frac{L}{AR_t} \qquad (3.14)$$

The one-dimensional Fourier Equation (3.15) is also employed for the calculation of the thermal resistances of the neck region, for both liquid and solid phases, assuming that q_z is constant and $A(z)$, the cross section area, is variable, which gives:

$$q_z = -kA(z)\frac{dT}{dz} \qquad (3.15)$$

This expression can be integrated in the form:

$$q_z \int_{z_0}^{z} \frac{dz}{A(z)} = -k \int_{T_0}^{T} dT \qquad (3.16)$$

This integration of the Equation (3.16) results in:

$$q_z = \left(\frac{-k}{\int_{z_0}^{z} \frac{dz}{A(z)}}\right)(T_2 - T_1) \qquad (3.17)$$

The term in parentheses in the Equation (3.17) represents the inverse of neck thermal resistance:

$$R = \frac{\int_{z_0}^{z} \frac{dz}{A(z)}}{-k} \qquad (3.18)$$

Based on the geometry, the following expression for the neck radius as a function of its geometric parameters is proposed:

$$r_p^s(z) = \sqrt{r_m^2 - \{z - [(r + r_m)\cos\alpha_1]\}^2} + r_m + x \qquad (3.19)$$

The thermal resistance of the neck solid phase becomes:

$$R_p^s = \frac{1}{\pi k_s} \int_{z_1}^{z_2} \frac{dz}{\left(r_p^s(z)\right)^2} \qquad (3.20)$$

where $z_1 = r_1 \cos\alpha_1$ and $z_2 = r_1(2 - \cos\alpha_1)$ are the lengths in z direction, measured from the sphere center (see Figure 14).

Considering $r(z)$ and substituting it by r_m in the equation (3.20), the neck resistance can be presented as:

$$R_p^s = \frac{2h}{\pi k_s (r_m)^2} \qquad (3.21)$$

Substituting Equations (3.7) and (3.9) in this expression, one has the following equation for the neck resistance:

$$R_p^s = \frac{8r \left(1 - \frac{r}{r+r_m}\right)}{\pi k_s \left[x + r \left(\frac{x+r_m}{r+r_m}\right)\right]^2} \qquad (3.22)$$

The constriction thermal resistances of the full (solid) and shell (liquid) hemispheres (R_L^s and R_L^l, respectively) were calculated employing the model presented by Yovanovich *et al.* (1978), developed for the conduction heat transfer between solid or hollow spheres in contact. In this model, the heat flux enters the elementary cell by the left flat circular area of radius r maintained at temperature T_1 and it is released to the right area maintained at temperature T_2 (see Figure 14). The heat delivered to the hot hemisphere is constricted to the neck region when passing to the other hemisphere and then spread in the cold hemisphere. The same happens to the liquid shell. The lateral walls of the elementary cell are considered insulated. The solid and hollow sphere constriction thermal resistances are obtained from the exact temperature distribution solution of the heat equation in spherical coordinates, as a function of directions r and φ, solved by Yovanovich *et al.* (1978). Their solution is given in terms of a series. Bahrami *et al.* (2006) presented a simplified expression for Yovanovich *et al.* (1978) solution, valid for a specific range of contact angles. In this thesis, a study similar to that presented by Bahrami *et al.* (2006) was performed, but for a wider range of the solid contacting angles. The following expression for the constriction resistance is obtained:

$$R_h^s = \frac{0.56}{k_s x} \tag{3.23}$$

Actually, the value of the constant proposed by Bahrami *et al.* (2006), instead of 0.56, was 0.5.

Substituting Equations (3.22) and (3.23) in the overall thermal resistance, Equation (3.12), one gets:

$$R_t = \frac{0.56}{k_s x} + \frac{8r\left(1 - \frac{r}{r+r_m}\right)}{\pi k_s \left[x + r\left(\frac{x+r_m}{r+r_m}\right)\right]^2} \tag{3.24}$$

From Equation (3.13), the total resistance can also be defined as $R_t = L/k_{eff}A$. The porosity can also be defined in terms of areas (for constant thickness porous media) as:

$$\varepsilon = \frac{A_t - A_s}{A_t} \tag{3.25}$$

So that the total thermal resistance is:

$$R_t = \frac{2r_1(1 - \varepsilon)}{k_{eff} A_s} \tag{3.26}$$

Matching Equation (3.24) and (3.26), a non-dimensional effective thermal conductivity of the sintered porous can be determined:

$$\frac{k_{eff}}{k_s} = \frac{2(1 - \varepsilon)}{\pi r} \left(\frac{0.56}{x} + \frac{8r\left(1 - \frac{r}{r+r_m}\right)}{\pi \left[x + r\left(\frac{x+r_m}{r+r_m}\right)\right]^2} \right)^{-1} \tag{3.27}$$

This Equation will be used latter to compare with literature data that include porosity as entry parameter.

3.3.3 Experimental procedure

The effective thermal conductivity in the different types of powder obtained from sieving of PAM copper powder was measured using a thermal conductivity analyzer C-thermal Tci. According to manufacturer of device, Thermal Conductivity Analyzer employs a model transient heat transfer to calculate the thermal conductivity. A cylindrical sample is placed on the plane sensor. A known current is applied to the sensor's spiral heating element, providing a small amount of heat, which warms up the interface between the sensor and the sample, inducing a variation in the voltage readings of the sensor. Then, the rate of increase in the sensor voltage is used to determine the thermal properties of the sample. A photography and scheme of the experimental setup is presents in the Figure 16. Cylindrical samples with 25 mm of diameter and 5 mm of thickness was used to measure the effective thermal conductivity. To guarantee the plane face in the sample, it was sanded until obtained a planes superficies. The samples also were saturated with distillated water.
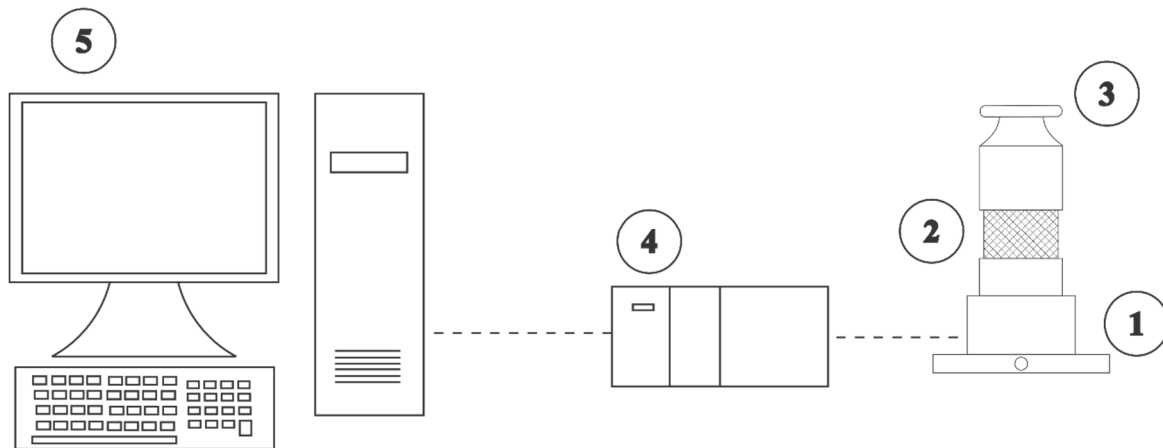
Figure 16 - Schematic of Thermal conductivity analyzer measurement setup. 1. Sensor, 2. Sample, 3. Calibrated mass; 4. Data acquisition system, 5. Computer.

3.3.4 Results and conclusions

In this subsection, the effective thermal conductivity measured to the different powers is presented and compared to theoretical model. The experimental data obtained by Flórez *et al.* (2013) are also analyzed. The Equation (3.27) expresses non-dimensional effective thermal conductivity as a function of the neck radius and porosity. Substituting the porosity given by Equation (3.5) into Equation (3.27), one can have the effective thermal conductivity becomes a function of powder particle radius only.

In Figure 17, the neck radius is plotted against the average particle diameter, for two different temperatures of sintering. In this figure, it is possible to observe that the neck is more sensitive to variations of the neck radius for small diameter particles, where a slope curve change is observed for particles diameters about 20 to 30 µm. One can also see that the sintering temperature influences the neck formation: the higher the temperature, the higher the neck radius. Also, the differences between the neck radiuses for media sintered at these two temperatures levels varies from zero do around 15 %.
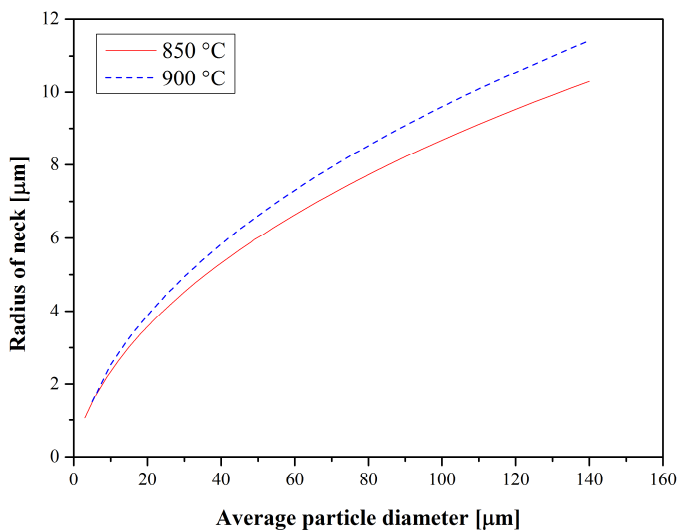
Figure 17 - The neck radius against mean particle diameter.

Figure 18 presents the comparison between the effective thermal conductivity calculated from the theoretical model presented in this work and with two sets of experimental data (run 1 and 2) obtained for copper sintered porous media fabricated in Labtucal at 850 °C from powders PAM (around 50µm) and PAC (around 20 µm), saturated by distilled water, obtained by Flórez *et al.* (2013). The results of the effective thermal conductivity measured in the samples obtained from sieved of PAM copper powder showed the dependency of the effective thermal conductivity with particle size and neck compared to the proposed models (cubic and Orthorhombic). The results of effective thermal conductivity for particle diameter lower than 60 µm present a difference that increases as the average article diameter decreases. The higher difference was obtained to the effective thermal conductivity measured to copper powder with average particle diameter of 22.23 µm, it was a 45.7 % above of the value predicted by the proposed models. The lower difference of 6.8 % was to sample with the average particle diameter equal to 68.81 µm when compared to the orthorhombic model.
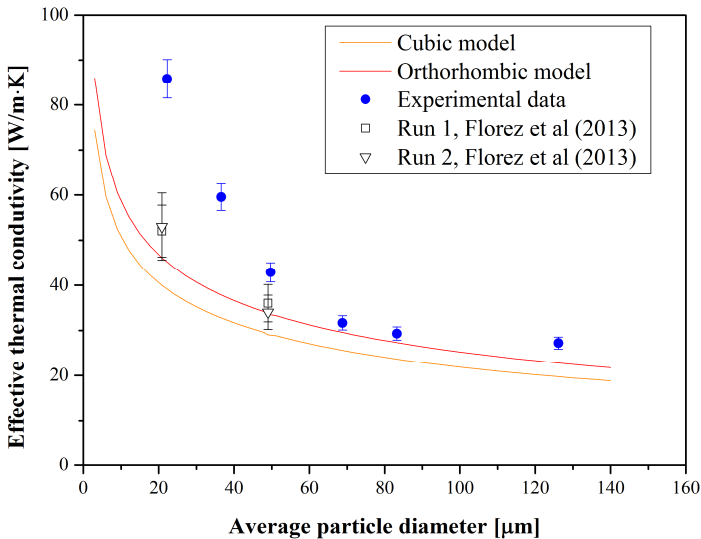
Figure 18 - Effective thermal conductivity model against average particle diameter.

Even, in Figure 18, the results of the effective thermal conductivity based in cubic and orthorhombic packing arrangement show best

comparison with experimental data: for cubic model, the highest difference is 23.3 % and for the orthorhombic model, it is 11.5 %. One should note that the theoretical orthorhombic model curve is within the experimental uncertainty reported by the present author in Flórez *et al.* (2013), represented by vertical bars in this graphic. Note that, in this figure, the porosity model which provides the input parameter for the effective thermal conductivity model was not corrected by the circularity factor, as non-circular spheres where not taken into account in the physical model, which schematic is shown in Figure 14.

One can see that experimental data obtained by Flórez *et al.* (2013) showed the best comparison with the proposed models than the results obtained for the porous media fabricated from sieved powder. This behavior can be explained due to following reasons. In the measurement using the thermal conductivity analyzer C-thermal Tci, one face of the sample in contact with the sensor was sanded. The original surface is modified closing the porous with the extract material. The measured method using by thermal conductivity analyzer C-thermal Tci is a flesh method. The response of the sample for a pulse of energy is modeled as a conductive heat problem in transient state. Then, the properties are determined as the parameter solution of the inversed problem. Hence the effective thermal conductivity measured can be modified due to reduction of the porosity of the surface of the sample analyzed.

In the other hand, the measurement method used in the experimental work by Flórez *et al.* (2013) was the comparative method where the samples are not modified by application the pressure or sanding.

Theoretical non-dimensional effective thermal conductivity and porosity against non-dimensional neck radius *x/d* are presented in the Figure 19. It can be observed that the porosity decreases as the *x/d* diameter increases, this effect is more pronounced for large values of *x/d*, while, for *x/d* ranging from 0.07 to 0.2, the porosity value is almost constant. On the other hand, the effective thermal conductivity shows a close to linear behavior with the particle diameter increase. Actually, the neck radio growth improves the heat transfer because there is more available area to transfer the heat. These results were calculated using the effective thermal conductivity for the theoretical model based on cubic and orthorhombic packing arrangements, for sintering temperature of 850 ºC.

Figure 20 presents a comparison between experimental data and the effective thermal conductivity calculated from the model proposed in this work, considering the porosity resulting from cubic packing. This

figure also shows a comparison with literature models. It is important to highlight that the input parameter for the effective thermal conductivity of sintered porous media in literature models (ALEXANDER, 1972; ATABAKI; BALIGA, 2007) is the porosity, which has to be measured after the media is fabricated, since no literature model predicts the porosity as a function of the fabrication parameters. Instead, in the present model, the input parameter is the mean powder radius, data usually provided by the powder supplier.
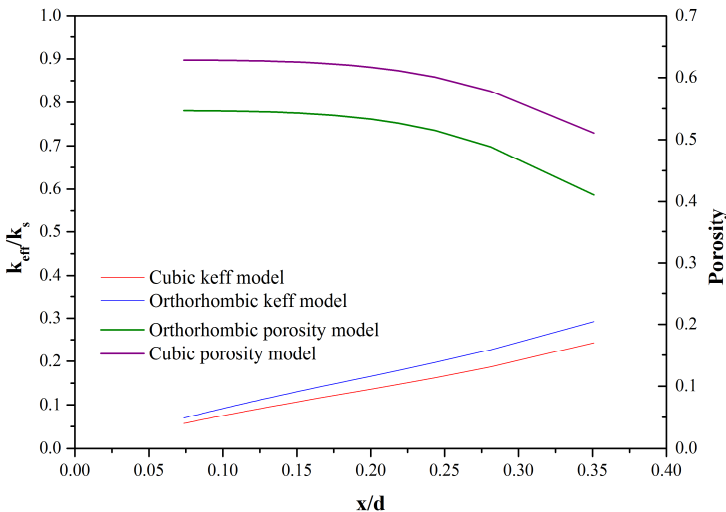
Figure 19 - Non-dimensional effective thermal conductivity and porosity against neck radius.

It is interesting to note that, in the present model, porosity zero means that only the presence of the solid is observed, while porosity one means that only fluid phase is considered. So, there no sense in working with these two limits. In the present model, the porosity has a higher, bound limited by the selection of the packing arrangement. Therefore, the plots are limited to porosities ranging from 0.2 (achievable for powder with a large dimension spectrum and/or sintered at higher temperature levels) to around 0.6, the highest theoretical porosity for regularly arranged spheres, with no necks. This is supported by the observation of the experimental data presented in Figure 12, where the porosity achieves a maximum value, which is kept constant, regardless of the increase in the diameter of the particle.
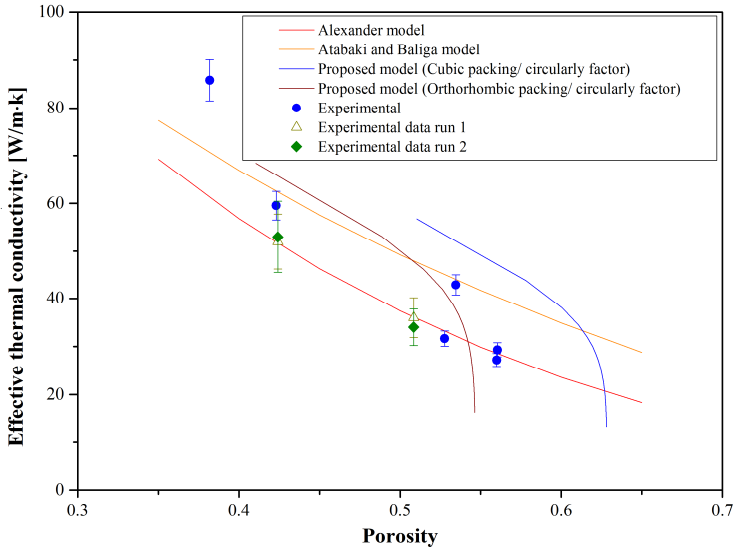
Figure 20 - Effective thermal conductivity versus porosity for experimental data and values calculated from literature models for porous media saturated with water.

The difference between the present effective thermal conductivity models ad data ranges from 14.7 % to 23.3 %. The Alexander (1972) model presents the best comparison with experimental data, which ranges between -4 % and -6.8 %. The model of Atabaki and Baliga (2007) also shows a good comparison with the data, varying from 23.6 and 40 %. Actually, the present model compares very well with Atabaki and Baliga (2007) model for low porosity porous media but the comparison deteriorates as the porosity tends to the physical model limit (porosity around 47 %), due to the reasons described in the last a paragraph.

Again one should remember that, in Figure 20, to determine the present model effective thermal conductivity as a function of porosity, two models were used: one to obtain the x–axis data (porosity) and other for the y-axis parameter, or the effective thermal conductivity, both using the mean particle radius as input parameter. On the other hand, for the literature model, the input parameter is obtained by the direct measurement of the porosity. Therefore, the good comparison between data and present model and among the present and literature models,

show that the models presented can be applied for the prediction of the porosity and of the effective thermal conductivity of sintered porous media.

3.4   Permeability

One of the most important properties for porous media is the permeability. The knowledge of permeability enables the prediction of the flow rate for a pre-determined pressure drop or, on the other side, the prediction of the fluid pressure necessary to achieve a specific flow rate.

Actually, permeability is associated with the porosity of the porous structure and with the powder particle diameter. This relation is known as Blake – Kozeny's Equation (KAVIANY, 1995). Other permeability models such as Carman Kozeny and Rumpfe-Gupte are also used in heat pipes predictions. These models determine the permeability from porosity and particle diameter parameters (FAGHRI, 1995). Several works in literature are focused in the improvement of this model.

Byon and Kim (2013) investigated experimentally and analytically the effects of the particle size distribution and of the packing structure. In this study, they considered two distinct types of porous media: mono-dispersed and bi-dispersed. The effect of the particle structure was represented by two geometry parameters: the particle arrangement and the particle bonded area, which depends on the sintering condition. The effect of the particle arrangement was studied for three unit-cell configurations: face centered cubic (FCC), body centered cubic (BCC) and simple cubic (SC). The effect of the bonded area (between sphere particles) and of the particle radius were also considered. They modified Blake Kozeny's equation using two correction factors for the particle size: (the mean particle diameter and the mean cluster size) and obtained a correlation for permeability of bi-dispersed medium.

Another commonly used relation is Darcy's Law that relates the pressure drop to the flow velocity. Endo *et al.* (2009) used the analogy between electrical circuit and Darcy's Law to obtain the permeability parameter. This author considered several particle diameters and the resulting packing bed was divided into small cubic regions, defined as unit cells. The unit cells have different electrical resistances, which were connected in a combination of series and parallel paths. Ohm and Kirchoff's law were used in the solution of the equivalent thermal circuits, resulting in the hydraulic resistance model. Then, numerical method was employed in order to obtain the permeability of the bed packing. Experiments were done using several porosity glass beds, polypropylene

particles and silica particles, of different sizes and shapes. Their experimental data were in good agreement with the results of theoretical calculations.

Yang *et al.* (2014) simplified an expression that determines the permeability for isotropic porous media as a function of the tortuosity, porosity and pore size, obtaining an equation that depends only of porosity and pore size. Therefore, this analytical study discusses the effect of these two morphological parameters on the permeability. Permeability of inverse wick (media in which porosity is larger than that found in conventional sintered particle wick, due to the sacrificial template used during the sintering particles process) was investigated numerically by Ngo and Byon (2016). As Blake – Kozeny's and Kozeny – Carman's equations cannot be applied for materials with very high porosity, these authors performed a non-linear regression analysis in order to embrace all configurations of wicks (KAVIANY, 1995). As a result, correlations based on numerical simulation were obtained for different packing structures. Two modified Kozeny–Carman equations were proposed: one for conventional wicks and another for inverse wicks.

From this literature review, one can see that several parameters are necessary to predict the permeability of sintered porous media. In this section, an analytical model for prediction of the permeability of sintered porous media, made from particles of approximately the same dimensions, is presented. In this approach, the fluid flow through the gaps within spheres in contact of a simplified arrangement geometry is modeled. Sintered porous media is modeled as an arrangement of spherical particles, with several packing configurations.

3.4.1 Mathematical model

The powder particles from which the porous media is made are modeled as spheres of uniform radius *r*. Several packing configurations can be observed, when the same diameter spheres are in contact. In Figure 21a, two packing configurations according to German (1989) are presented: simple cubic and orthorhombic. These arrangements are employed to determine the theoretical permeability of a sintered porous media.

Any arrangement of same diameter spheres shapes channels with non-circular cross sections within where fluids subjected to pressure differences flow, following a pattern of consecutive constrictions and expansions. Figure 21b shows the schematic of cross the sections of the

ducts formed by spheres in simple and orthorhombic cubic packing arrangement.
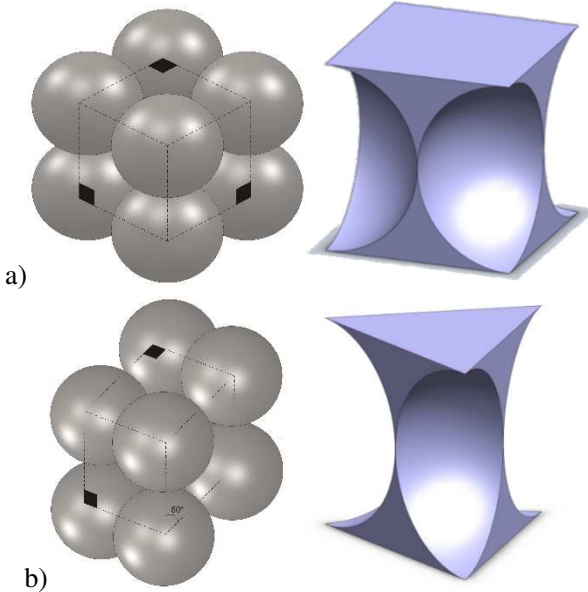
Figure 21 - Channels physical model a) Cubic b) Orthorhombic.

In this work, the permeability was modelled using the Darcy's law. Henry Darcy made an experiment based on the flow of water though a pipe packed with sand. He noticed that the velocity u is uniform and proportional to the negative of pressure gradient (AKBARI; SISTON; BAHRAMI, 2010). This relation, known as Darcy's law is enunciated as:

$$-\frac{dP}{dx} = \frac{\mu}{\kappa} u_D \qquad (3.28)$$

where κ is the permeability of the media (m^2), μ is the dynamic viscosity of fluid and dP/dx is the pressure gradient in the direction of x-axis. In the present case, the fluid mass flow $\dot{m}$ within the bulk space among the spheres can be expressed as:

$$\dot{m} = \rho A_n u_D \qquad (3.29)$$

where A_n is the transversal area at inlet of channel for each packing system considered and u_D is Dacy's velocity. Substituting Equation (3.28) in

(3.29) and integrating in the x direction along the L length, the mass ratio becomes:

$$\dot{m} = \frac{\rho A_n \kappa}{\mu} \frac{\Delta P}{L} \qquad (3.30)$$

From the analogy of Darcy's law with Fourier's law, the hydraulic resistance of the mass flux through a cross section can be defined as:

$$R_h^D = \frac{\mu L}{\rho A_n \kappa} \qquad (3.31)$$

Another expression for the hydraulic resistance through ducts can be obtained from the solution of the internal flow, according to the particle arrangement. Akbari *et al.* (2010) obtained an expression for the hydraulic resistance, based on converging-diverging laminar fully developed flows. From the solution of conservation of mass and momentum equations, the unit cell pressure drop in z-axis direction can be obtained, with the adoption of the following hypothesis:

- Steady state conditions.
- Two dimensional (r,z) cylindrical coordinated problem.
- Laminar regime.
- Fully developed velocity profile.
- Isotropic wick structure.
- Particle material is represented by spheres of an average radius.
- The working fluid is incompressible.
- Constant properties.
- Non-slip condition of the fluid on the walls.
- Gravity effect is negligible.

Therefore, the conservation of mass equation takes the following form, where u and v are the axial and radial velocities, respectively:

$$\frac{1}{r} \frac{\partial}{\partial r} (rv) + \frac{\partial u}{\partial z} = 0 \qquad (3.32)$$

The Navier-Stokes equation in r and z are:

$$\rho\left(v\frac{\partial u}{\partial r} + u\frac{\partial u}{\partial z}\right) = -\frac{\partial P}{\partial z} + \mu\left\{\frac{1}{r}\frac{\partial}{\partial r}\left[r\frac{\partial u}{\partial r}\right] + \frac{\partial^2 u}{\partial z^2}\right\} \qquad (3.33)$$

$$\rho\left(v\frac{\partial u}{\partial r} + u\frac{\partial u}{\partial z}\right) = -\frac{\partial P}{\partial r} + \mu\left\{\frac{\partial}{\partial r}\left[\frac{1}{r}\frac{\partial(rv)}{\partial r}\right] + \frac{\partial^2 u}{\partial z^2}\right\} \qquad (3.34)$$

These partial differential equations are subject to the boundary conditions:

$$u(R, z) = 0, v(r, z) = 0, R = a(z), P(r, 0) = P_0 \qquad (3.35)$$

where $a(z)$ is the radio of the equivalent cross section liquid flow area, which depends on the geometry of the sphere arrangement, to be discussed in the next section. The axial and radial velocities profiles, proposed by Akbari *et al.* (2010) are respectively:

$$u(r, z) = 2u_{m,0}\left[\frac{a_0}{a(z)}\right]^2\left[1 - \left(\frac{r}{a(z)}\right)^2\right] \qquad (3.36)$$

Integrating the Equation (3.33) for P in z and calculating the average pressure in $z = 0$ (a_0) and $z = r$ (a_1), Akbari [9] obtained an expression for the pressure drop in z-axis direction:

$$\Delta P = \frac{16\mu u_{m,0}L}{a_0^2}\left[\frac{\lambda^3 + \lambda + 1}{3\lambda^2} + \frac{\tilde{m}(1 + \lambda)}{2\lambda^5}\right] \qquad (3.37)$$

where $\tilde{m} = r'(z)$, $\lambda = a_1/a_0$ is ratio between the minimum and the maximum radius. Again, from analogy between the hydraulic flow and electrical circuit, the following hydraulic resistance can be defined:

$$R_h^{ns-z} = \frac{\Delta P}{\dot{m}} \qquad (3.38)$$

which is equivalent to a flow in a single converging-diverging tube. These fluid flow phenomena was considered as equivalent to the constriction-expansion observed in real channels, formed within spheres of a unit cell. The mass ratio $\dot{m}$ that flows across of the unit cell is defined as:

$$\dot{m} = \rho \mu_{m,0} \pi u a_0^2 \tag{3.39}$$

where $u_{m,0}$ is mean velocity evaluated in $z = 0$. Substituting the Equations (3.30) and (3.38) in (3.39) yields:

$$R_h^{ns-z} = \frac{16\mu a_1}{\rho \pi a_0^4} \left[\frac{\lambda^2 + \lambda + 1}{3\lambda^2} + \frac{\tilde{m}(1+\lambda)}{2\lambda^5} \right] \tag{3.40}$$

Matching Equations (3.31) and (3.41), the permeability k can be isolated, resulting in the expression:

$$k = \frac{\pi L a_0^4}{16 A_n a_1} \left[\frac{\lambda^2 + \lambda + 1}{3\lambda^2} + \frac{\tilde{m}(1+\lambda)}{2\lambda^5} \right] \tag{3.41}$$

Actually, the application of this model requires transformation of non-circular ducts into circular tubes using characteristic lengths. In the following section, several procedures are proposed to convert non-circular sections into equivalent circular channels.

3.4.2 Characteristic dimensions

In the present work, non-circular ducts are modelled as circular, using several specific characteristic dimensions, such as the hydraulic ratio and the characteristic length $\sqrt{A}$, as proposed by Bahrami *et al.* (2006). These dimensions vary along the liquid flow channel. The summary of the equivalent hydraulic diameter expressions (d) is presented in the Table 5.

Table 5. Hydraulic diameter models.

Bahrami *et al.* (2006)	$d_b(z) = \sqrt{A(z)}$ (3.42)
Fox and MacDonald (2001)	$d_h(z) = 4\dfrac{A(z)}{Pe(z)}$ (3.43)

- *Cubic Packing*

From simple geometry analysis, several expressions can be obtained to calculate the fluid flow cross section area as function of the *z* direction. In Figure 22, a cross section area of a simple cubic packing in a specific z-axis point is shown.
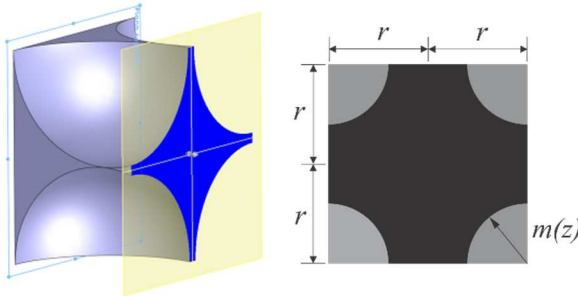
Figure 22 - Cross section area for sphere cubic packing arrangement, which varies along the channel.

The transversal irregular cross section geometry is considered as a circular duct using the well-known hydraulic diameter concept. In Table 6, two expressions for the equivalent radius for the cubic packing arrangement are presented, where $m(z)$ is a geometric parameter, defined as:

$$m(z) = r \sqrt{1 - \frac{(z-r)^2}{r^2}} \tag{3.44}$$

and where r is the average particle radius of the powder material of the porous media.

Table 6. Hydraulic radius for Cubic Packing.

Hydraulic model		
Bahrami *et al.* (2006)	$a(z) = \dfrac{\sqrt{4r^2 - \pi m^2}}{2}$	(3.45)
Fox and MacDonald (2001)	$a(z) = \dfrac{4r^2 - \pi m^2}{4(r-m) + \pi m}$	(3.46)

- Orthorhombic Packing

Similarly, the ducts formed by the channel voids, with variable cross section area, formed among spheres in orthorhombic packing arrangement, can be considered as circular ducts, using the equivalent hydraulic diameter expressions, taken from the literature and given in Table 7.

Table 7. Hydraulic radius for Orthorhombic Packing.

Hydraulic model		
Bahrami *et al.* (2006)	$a(z) = \dfrac{1}{2}\sqrt{\sqrt{3}r^2 - \dfrac{\pi m^2}{2}}$	(3.47)
Fox and MacDonald (2001)	$a(z) = \dfrac{2\left(\sqrt{3}r^2 - \dfrac{\pi m^2}{2}\right)}{6r + m(\pi - 6)}$	(3.48)

Figure 23 shows a schematic of the liquid flow cross section area in such orthorhombic arrangement in any point of the *z*-axis direction.
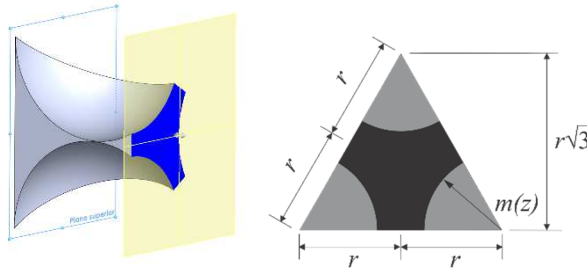
Figure 23 - Cross section area for the sphere orthorhombic packing arrangement, which varies along the channel.

Using the Maple software, the circular equivalent channels could be plotted, for each packing configuration, employing the hydraulic diameter concept. Four different geometrics were obtained, all of them are used in the mathematical permeability model for sintered porous

media, proposed in this work. In Figure 24, the circular duct with convergent – divergent section are shown.
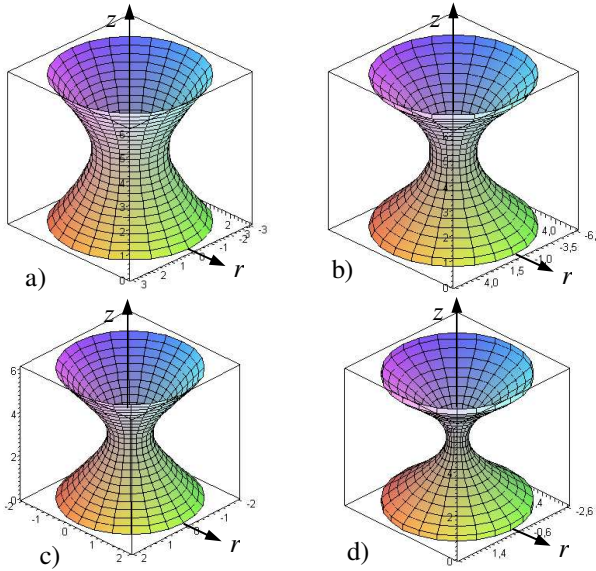
Figure 24- Equivalent channels. a) Cubic packing by Bahrami et al. (2006), b) Cubic packing by Fox and MacDonald (2001), c) Orthorhombic packing by Bahrami et al. (2006), and d) Orthorhombic packing by Fox and MacDonald (2001).

3.4.3 Experimental procedure

The permeability of the porous media was indirectly measured through the following expression, based on Darcy's law:

$$\kappa = \frac{\mu \dot{m}}{\rho A} \left(\frac{\Delta P}{L}\right)^{-1} \qquad (3.49)$$

where A is the cross-section flow area, ρ and ΔP represents the density and pressure drop, respectively, and L is length in the direction of the flow within the porous material. In this work, to measure the permeability, an equipment was designed and built according to Darcy's experiment. Figure 25 shows a sketch and a photography of the apparatus.
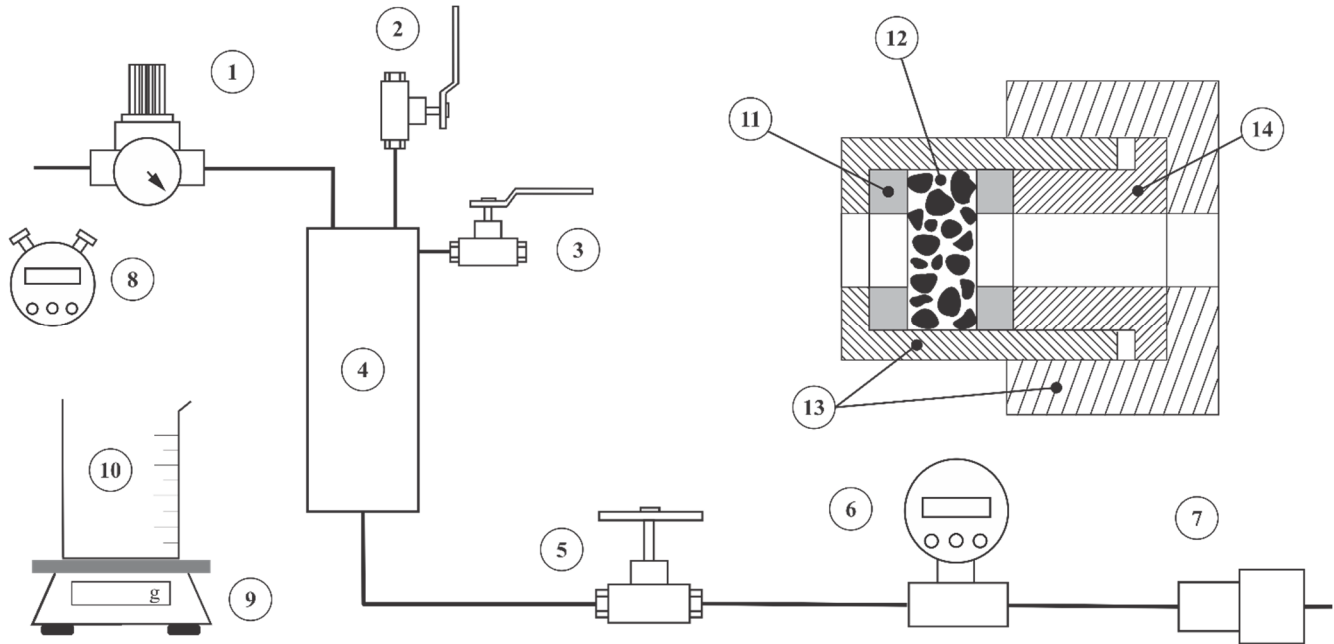
Figure 25 - Experimental equipment. a) Schematic of permeability measurement setup: 1.Air pressure gauge, 2.Charge fluid valve, 3.Control level valve, 4.Tank, 5.Mass rate control valve, 6.Digital manometer, 7.Test section, 8.Cronometer, 9.Balance, 10.Beaker, 11.Rubber gasket, 12.Sample, 13.Case and 14.Polymer gasket. b) Photography of permeability apparatus.

The measurement setup is composed of three main sections. The first one consists of a distilled water tank and an air pressure transducer, responsible for keeping the water flow in constant fluxes. The second section consists of a working fluid valve, which allows the controlling of the water mass fluxes during the permeability measurement, and a digital manometer Zürich-Z10B that measures the water pressure before entering the sample. In the third section, the sample is positioned between the two rubber gaskets by a holder and pressed against a stainless steel case. Between the second and the third sections, there is a tube, which length is more than 7.5 times higher than the diameter of duct, to guarantee the developed flow at inlet region of the sample (FOX; MCDONALD, 2001). The mass flow rate is calculated from the measurement of the water mass accumulated in a Becker recipient for a time period of 30 seconds, registered by a digital chronometer. The permeability of copper powder sintered cylindrical samples was measured. The properties of the distilled water, evaluated at 25 °C, were obtained from literature thermodynamic tables (CENGEL; BOLES, 2006). Particles of different sizes obtained from successive mechanical vibration siftings of atomized copper powder were employed in fabrication of samples and the permeability were measured.

3.4.4 Data analysis and results

In this section, the analysis of the permeability measured according to procedure explained previous section is presents. The experimental porosity used to compare the permeability calculated from the literature model is presented in the Table 8.

Table 8. Experimental porosity.

Type classified	Mean particle diameter[μm]	Experimental porosity [%]
A	22.23	38.19 ± 1.45
B	36.59	42.31 ± 2.86
C	49.72	53.46 ± 3.87
D	68.81	52.77 ± 1.30
E	83.25	56.04 ± 1.44
F	126.16	56.00 ± 3.00

- Present model comparison with data

Figure 26 shows a comparison between the experimental data and the permeability calculated from the model proposed, for each sintered porous media experimentally studied. The *x*-axis represents the average particle diameter of the metal powder used to fabricate the sintered porous media tested and the *y*-axis represents the permeability. One can conclude, observing Figure 26, that the results of the permeability model, based on the cubic packing arrangement, where the hydraulic diameter is taken as the square root of the cross area, shows the best comparison with experimental data. However, the difference between this model and experimental data vary from 19 % to 143 %. This large difference can be explained by simplifications such as the hypothesis of perfect particle spherical shape and of their ordered arrangement. In this work, the fabrication method used to produce the powder was atomization of copper in liquid flow, which does not produce particles completely spherical (LAWLEY, 1992).
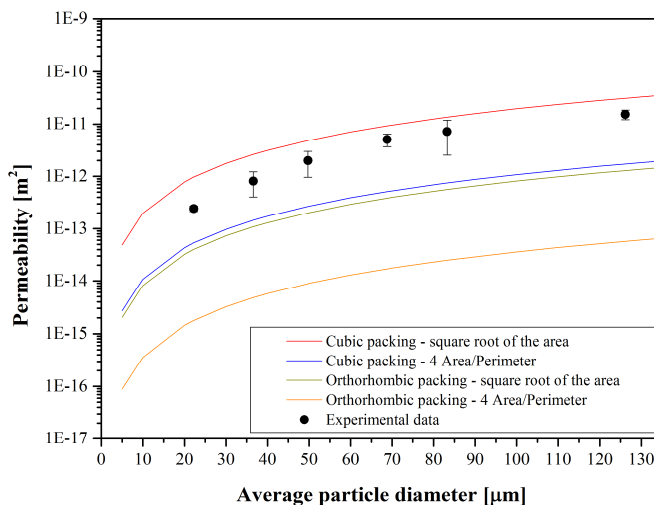
Figure 26 - Permeability results compared with the proposed models.

The permeability calculated using the proposed model has the same order of magnitude of the experimental data, which is a very good result, considering the magnitude of the permeability and the inherent difficulty in measuring and modelling such small physical parameters. In Figure 26, one can also observe the similar behavior trends followed by the

theoretical results and the experimental data. It suggests that the model based on a converging-diverging tube is a good approximation for the liquid flow into a porous media, in low Reynolds number regimen.

The other models proposed based in cubic (hydraulic diameter calculated form $4A/P$) and orthorhombic (hydraulic diameter calculated form $4A/P$ and the square of across area) packings present higher differences when compared with experimental measurement, that can be up to 400 % larger than the data.

- Comparison with literature models

Figure 27 shows a comparison between the experimental data and the permeability calculated from the proposed and literature models. Note that the permeability calculated from literature models require the porosity and the average particle diameter as input parameters, while, in the present model, only the particle dimension is the input data. In Figure 27, one can see that both literature and proposed models show similar behaviors. However, the smaller difference of the permeability estimated by models was 53 % and the largest was 400 % (Carman-Kozeny), when compared to experimental data.
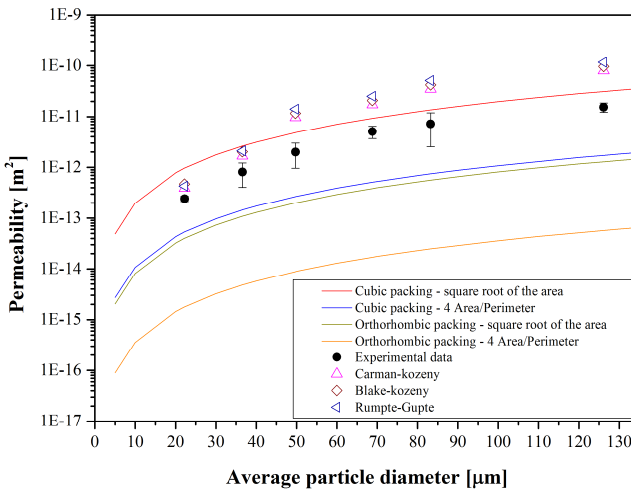
Figure 27 - Permeability results comparing the proposed and literature models, based on porosity and average particle diameter.

Actually, in literature of LHPs, these models (Karman-Kozeny, Blake-kozeny and Rumpte-Gupte) are used to calculate the permeability of

sintered porous (FAGHRI, 1995; KAVIANY, 1995). A good evaluation of the impact that the uncertainty in the determination of the permeability can have over the prediction of LHP behavior can be observed from the calculation of the pressure drop for water flow within sintered porous media with fixed geometry, which can be obtained from the equation:

$$\Delta P = \frac{L}{\kappa A} \frac{\mu \dot{m}}{\rho_l}$$

(3.50)

This expression was applied for the presently tested device. In equation 22, μ is the dynamic viscosity, ρ is the density of water, L is the porous media thickness (8 mm), A is the cross section area (cylindrical sample of 8 mm of diameter) and $\dot{m}$ is the mass flux of 1.91×10^{-3} kg/s. The pressure drop calculated using several permeability models, including the one proposed in the present work, is present in Figure 28, where one can see that the simple cubic packing model, based on the square root of the area, presents the best comparison with pressure drop data. The smallest difference observed is 16 % while the largest is 59 %. One can also note that, for all models, the difference between data and data increases for intermediate average particle diameter of the particles. Actually, this behavior follows the same trends observed in Figure 26 for the same range of particle diameter, where the permeability comparison between data and models also decreased.
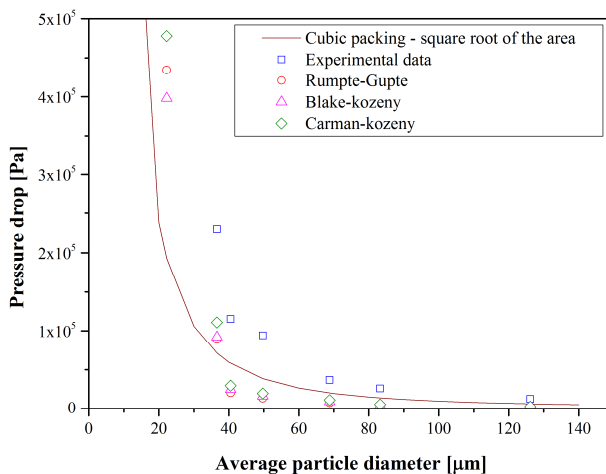
Figure 28 - Pressure drop results compared to the proposed and literature models.

Actually, one can consider as a reasonable prediction of the permeability if the model is able to calculate the permeability within the actual order of magnitude. Although, in Figure 26, the difference between the permeability predicted by the literature models and experimental data was of more than one order of magnitude, the largest pressure drop difference between prediction and data lies between 70 and 100 %.

3.5   Effective porous radius

Pores can be classified according to size: very large are called caverns and very small are called micropores or ultramicropores (KAVIANY, 1995). Pores of different size can be found inside the porous medium due to the process of manufacturing. Pore size is connected with other properties as permeability, porosity, effective thermal conductivity. The pumping capability of a wick in a loop heat pipe is expressed as function of the pore radius. The Laplace-Young (GENNES; BROCHARD-WYART; QUÉRÉ, 2004) equation indicates the capillary pressure of the wicks generated by the liquid-vapor interface and is known as:

$$\Delta P_{cap} = \frac{2\sigma}{r_p}$$

(3.51)

where σ is the working fluid surface tension, r_p is the pore radius and θ is contact angle formed between solid and liquid. In order to characterize the wicks more simply, the equation is replaced by:

$$\Delta P_{cap} = \frac{2\sigma}{r_{eff}}$$

(3.52)

where r_{eff} is the effective pore radius.

In the literature, the effective pore radio is measured experimentally using the Equation (3.52). Singh et $al.$ (2009) determined experimentally wick properties as permeability, pores radius, porosity and effective thermal conductivity. In order to measure pores radius, a transparent PVC tube was bent in the form of a U. Due to equality between air pressure and surface tension force of the water, bubbles emerge and allow to measure pore radius.

Giraudon *et al.* (2016) also used hydrostatic pressure to measure pore radius. Furthermore, they developed a model for the most appropriate porous structure characteristics taking into account some parameters as thickness, porosity, permeability, pore radius and thermal conductivity. The model predicts the final wick characteristics as a function of the manufacturing parameters.

Tang *et al.* (2013) examined the permeability and capillary pressure in normal sintered and grooved wicks. They also studied the effects of powder size, wick type and gravity in these tests. For capillary rate-of-rise tests, an infrared thermal was employed which enables to observe the moving front of liquid.

Holley and Faghri (2006) measured permeability and effective pore radius using the rate-of-rise test of sintered metal powder and carbon paper samples. For the rise of liquid in a wick, capillary pressure is assumed to be in balance with hydrostatic pressure and pressure loss associated with friction, taken from Darcy's Law.

Li *et al.* (2010) developed a method to investigate the capillary pumping amount changing curve recorded by experiment. For this, tree parameters were considered: capillary pumping amount (the maximum of working fluid that can be pumped into the porous wick), capillary pumping time (the time that the porous wick needs to reach saturation from the beginning of the capillary pumping) and capillary pumping rate (the velocity that the porous wick reaches saturation). They discovered that capillary pumping amount changing curve could be described with an exponential increase equation. The effect of porosity on capillary pumping was also studied. They conclude that capillary pumping rate increases with the increasing of the porosity.

Another quantity commonly measured is representative pore radius that represents the pore radii at which 50 % of the non-wetting liquid intrusion volume occurs. Li *et al.* (2010) found differences between representative pore radii and effective pore radii. This difference is attributed to the variation in contact angle made by the wetting liquid on the solid surface in experiments, possibly induced by contaminations. Palakurthi *et al.* (2015) studied the relationship between effective and representative pore radii using numerical experiments that allow to eliminate the effect of contact angle variations by keeping the contact angle constant. They conclude that the disparity between effective and representative pore radii do not arise from the contact angle variations.

3.5.1 Mathematical model

To model of effective porous radius is used the concept of hydraulic diameter proposed to calculate the permeability in the section 3.4. From geometrical transformation, similar expressions defined to $a(z)$ are evaluated in $z = 0$ and $z = r_p$. Therefore, the effective pore radius is defined as:

$$r_{eff} = a(z) \qquad (3.53)$$

where $a(z)$ is the hydraulic diameter evaluated for each packing arrangement (cubic and orthorhombic).

3.5.2 Experimental procedure

The effective pore radius tests are based in the measured of the pressure capillary required to equilibrate a meniscus of some specified size and shape. The bubble point test proposed by Dunn and Reay (1978) , where pressurized gas is applied to one side of a wick saturated with liquid. Thus, the gas pressure is gradually increased and the capillary pressure is measured at the point when bubbles form on the opposite side of the wick sample. Another test used by Faghri (1995) is the risen meniscus, where the liquid level rises in a wick sample until the capillary and hydrostatic pressures are equilibrated.

To determine of effective porous radius was fabricated an experimental set up bases in the bubbles method according to Paiva (2011). The apparatus is composed for an argon gas cylinder where a pressure valve is coupled. Other, second valve controls the mass rate. Following, a pressure sensor (Omega PX409-015DWUV) is used to measure the pressure gas in the internal side of the sample. Finally, an acquisition system data (National Instruments NISCXI-1000) is used to register the gradually increased of pressure. The design and photographic of experimental apparatus is present are presented in the Figure 29.

Copper sintered samples with cylindrical shape was fabricated and coated laterally with an epoxy resin. After, which the resin dried, the sample is attached into a silicone hose. The opposite side of the sample is filled with distillated water. The argon gas released across of sample until the gas pressure exceeds the hydrodynamic pressure and bobbles start appear. The measure process is repeated by 5 times.
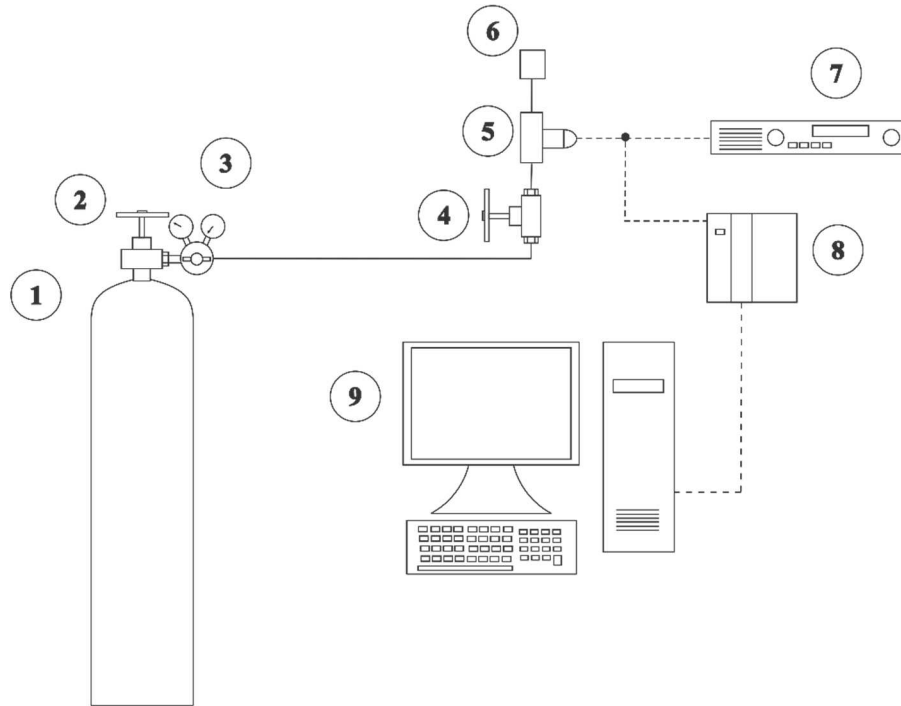
Figure 29 - Schematic of critical radius measurement setup. 1. Argon gas cylinder, 2.Gas pressure gauge, 3. Pressure regulator; 4.Mass rate control valve, 5.Diferential manometer, 6.Test section, 7.exicted power source, 8 Data acquisition system. 9 Computer.

3.5.3 Analysis and results

Figure 30 shows a comparison between the experimental data and the effective porous radius, calculated from the proposed models. One can see that both Bahrami and Fox cubic packing hydraulic diameter curves (superposed) have reasonable comparisons with the experimental data. Due to the adopted physical model, the two hydraulic equivalent diameters are equal for $z=0$. Using $0.21d_p$ as the effective porous radio, as suggested in the literature (SINGH; AKBARZADEH; MOCHIZUKI, 2009), actually overestimate the pump capacity, as one can see by the light green curve in Figure 30.
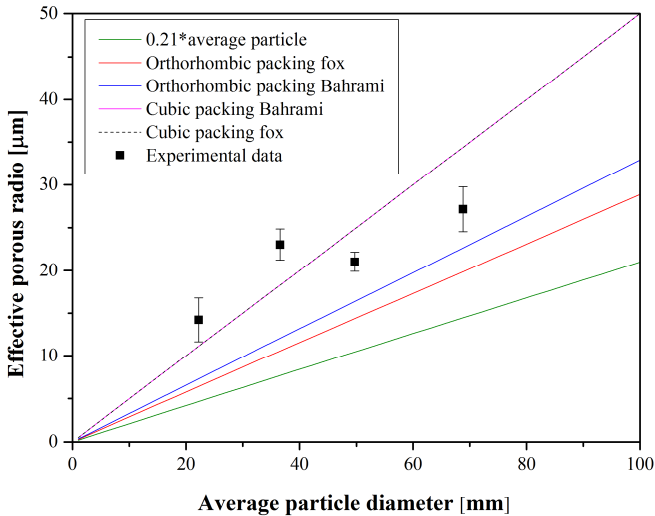
Figure 30 - Effective porous radio results compared to proposed, based on hydraulic diameter and average particle diameter.

3.6   Conclusions

In this chapter, several models based on the mean particle diameter as parameter input were proposed to estimate the porosity, effective thermal conductivity, permeability and effective porous radio of sintered porous media. The sintering process was described and mechanisms and models of literature were presented. Experimental apparatus were developed to measure the thermophysical properties and data were compared to theoretical values obtaining good comparison. These

models allowed to obtain the theoretical limit where the thermophysical properties analyzed are adequate and it becomes in a design tool.

In Figure 31, a summary of the thermophysical properties as functions of the average particle diameter and the experimental data are presented. The theoretical curve and experimental data for the effective thermal conductivity and permeability show opposite behavior, while the effective thermal conductivity decreases as the average particle diameter increases, the permeability and the effective porous radio increase as average particle diameter increases. The effective thermal conductivity and the permeability curve have a cross point that can be considered a limit between desirable and undesirable design values for this property. In the active zone of the evaporator is necessary that the wick structure have a high permeability to flow the working fluid with the lowest pressure drop. The effective thermal conductivity linked to geometry should allow that the highest heat power achieves the evaporation surface and avoid the heat transferred to the compensation chamber. Then, according with the Figure 31, the material properties chosen must be one with average particle diameter higher than 20 µm. However, one can be seen that capillary pressure depends on the effective porous radio, hence, small porous provide high capillary pumping. To determine the viability of a geometry and material for a wick structure of a LHP evaporator, the thermal and hydraulic response should be analyzed simultaneously.
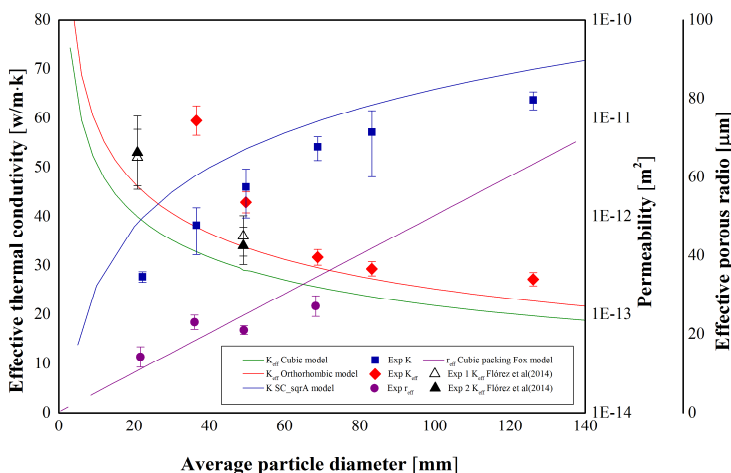
Figure 31 - Thermophysical properties as functions of the average particle diameter and the experimental data.

In the chapter 5, two type materials with 36 and 51 μm will be studied using a statistical analysis to determine the effect of the thermophysical properties and the geometrical of wick on the thermal and hydraulic responses for a power and operating temperature prescribed.

4 EVAPORATOR MODEL FOR LOOP HEAT PIPES

In this chapter, models for designing the geometry of cylindrical LHP evaporators and for predicting their thermal behavior are developed. In the first section, an expression based on scale analyses is proposed to determine a critical design factor, which relates the thermophysical properties of wick structure, the fluid properties and thermodynamic operation conditions with the geometrical parameters. Analytical models based on the solution of the mass, momentum and energy conservation equations in cylindrical coordinates were developed to analyze and avoid the dry-out of the liquid in evaporator wick structure. The temperature and pressure fields and the heat and mass flux were also obtained. Thermal and electrical analogy circuit model was used to estimate the operation temperature of the LHP. In this work, several literature models were used to calculate the thermal performance and pressure drop along the LHP, for comparison purposes.

4.1 Heat Transfer analysis

Several LHP heat transfer models are found in the literature. Launay *et al.* (2008) proposed an analytical mathematical model based on an equivalent thermal circuit. Singh *et al.* (2009) presented a theoretical model based on a heat balance (first law of thermodynamics) performed for a LHP with a cylindrical evaporator, similar to the one studied by Ku (1999), a cylindrical evaporator LHP with a primary and a secondary porous media layers. Kaya *et al.* (1999) proposed models for the thermal behavior of LHPs based on known geometric and thermophysical properties of materials and working fluids. Other models proposed are based on solutions of the continuity and energy equations, for simplified sections of the porous media within the evaporator.

Cao and Faghri (1994) presented analytical solutions for the liquid pressure and velocity fields and for the temperature distributions. Their physical model consisted of a porous media section, heated by solid fins. Darcy´s equations were employed to solve the velocity fields. Their analytical temperature results compared well with numerical data. However, the temperature field obtained did not allow for the determination of the heat transferred to the compensation chamber (heat leakage), which disturbs the thermal performance of the device. A numerical solution for the temperature distribution of a section of the

porous media, heated by a fin, was also presented by Demidov and Yatsenko (1994). They observed that the vapor front in the evaporator starts in the contacting surface between the heater wall and the wick structure: high heat fluxes may cause the onset of vapor bubbles that may grow and coalesce, eventually covering the entire contacting surface.

Siedel *et al.* (2005) developed an analytical model to determine the thermo-hydraulic behavior of LHPs. They combined energy balance equation with two-dimensional (2D) temperature field equations for a cylindrical evaporator, including the wick structure and casing. The values of the temperature-sensitive thermophysical parameters were taken for temperatures observed experimentally. This model presented good agreement with numerical simulation results and with experimental data.

Santos (2010) solved numerically thermal and hydraulic models for ceramic wick of evaporators of LHPs and CPLs. He studied theoretically a porous media composed by two layers of media with different thermal conductivities. Experimental tests were performed for two working fluids: water and acetone. Li and Peterson (2011) developed a three-dimensional (3D) model to analyze the heat and mass transfer of a flat evaporator of a LHP. Simulation results show good agreement with the operational temperature experimental data. Sintered copper powder was the wick structure used in the studied evaporator.

Chernysheva and Maydanik (2012) presented a 3D mathematical model for a flat sintered copper porous media evaporator, filled with water. The geometries of vapor exit channel, compensation chamber and porous structure were considered in their model. Actually, due to the evaporator mounting design, only a small fraction of the area, available for the heat exchange between evaporator and heat source, was used and so, the surface contact temperature did not follow the trends observed in the rest of the compensation chamber. Therefore, the formation of vapor was not uniform and it concentrated mainly on the central contact area between the evaporator and the heat source, showing low evaporation in the peripheral regions.

The performed literature review shows that the several works concerning analytical and numerical predictions of the thermal performance of LHPs do not deal with the evaporator geometry studied in the present work. In addition, no available model provides a criterion to be used for the design of the porous media thickness. In this work, theoretical and experimental analyses of the temperature and pressure distribution within working fluid filled porous media are presented. It is

shown that the resulting model can be used as a tool for designing LHP evaporators. The general model for determination of the operation temperature is presented. In the next chapter, two evaporators were designed and fabricated using the tools developed in this work. The experimental data obtained were analyzed and used as "study cases".

4.1.1 Physical model

The model proposed in this work is based on a copper LHP, with cylindrical shaped evaporator, as shown in Figure 32. The evaporator has two regions: the compensation chamber, with no porous media, and the capillary pump region, of length l, internally recovered by a copper powder sintered wick layer, of thickness δ. A porous media plug of length φ separates these regions (see Figure 32). The higher the pressure difference between the compensation chamber and the liquid-vapor meniscus interface, the better the system works. Therefore, the objective of the plug is, while allowing the liquid to reach the wick structure in the heated region of the evaporator, to decrease the heat leakage to the compensation chamber, avoiding its temperature increases, which would decrease the pressure difference and so disturb the LHP thermal performance, eventually stopping the system operation. In other words, the heat loss to the compensation chamber increases the working fluid temperature, decreasing the difference between the temperatures of the compensation chamber and of the evaporator meniscus. As a result, the working fluid pressure difference between these same regions of the LHP decreases (see Maydanik *et al.* (2011b)). The configuration studied in this work, is similar to the novel oval evaporator proposed by Maydanik *et al.* (2011b), which has been successfully tested and considered as an alternative to the conventional evaporators, because they allow for the use of copper and water. Actually, cooper is a material usually avoided due to its high thermal conductivity that causes large heat losses to the compensation chamber. Besides, water is also avoided because, despite of having good thermal properties such as high latent heat of vaporization and surface tension, it presents low pressure sensibility to temperature variations, for low operation temperatures (below 70 ºC). A simplified sketch of the evaporator is shown in Figure 33. This evaporator works similarly as the conventional ones: the condensate enters the evaporator through the liquid line and reaches the compensation chamber, crosses the porous media plug, reaching the capillary pumped region which external wall receives the heat power

input. In this work, the influence of the porous media layer δ and of the geometric parameters φ and l, in the thermal performance of capillary pumps in LHPs, are studied.
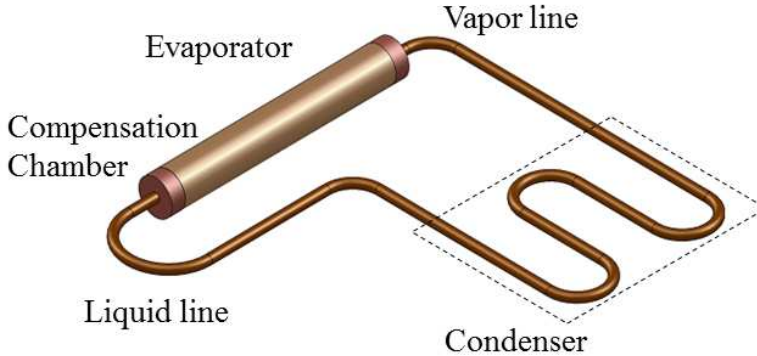
Figure 32 - Sketch of the LHP studied.

As already noted, heat power is delivered to the external area of the evaporator capillary pumping region, crossing the wall and reaching the wick structure. The wick must be designed so that the phase change occurs only in the liquid vapor meniscus (FAGHRI, 1995). In order to work properly, vapor must not be trapped within the porous media. As the vapor thermal conductivity is much lower than liquid´s, the thermal resistance of the evaporator can increase sensibly with the presence of vapor. In addition, vapor can cause working fluid pressure to increase and oscillate within the wick, disturbing the LHP behavior. Therefore, the wick design should provide proper permeability and porosity, to allow the liquid to flow through the media and adequate thermal conductivity, to avoid the vapor to be formed within the layer, out of the meniscus.

Therefore, the most probable location of the onset of undesirable vapor bubbles is in the interface between the porous media and the casing wall, in the evaporator external wall heated region. So, if one is able to avoid the vapor formation in this interface, no vapor bubbles are expected in any other evaporator region. In other words, the design of the device should guarantee, for the specific power input under consideration, that the temperature of the wick-casing wall interface is kept lower than the phase change temperature for liquid saturation pressure inside the wick.
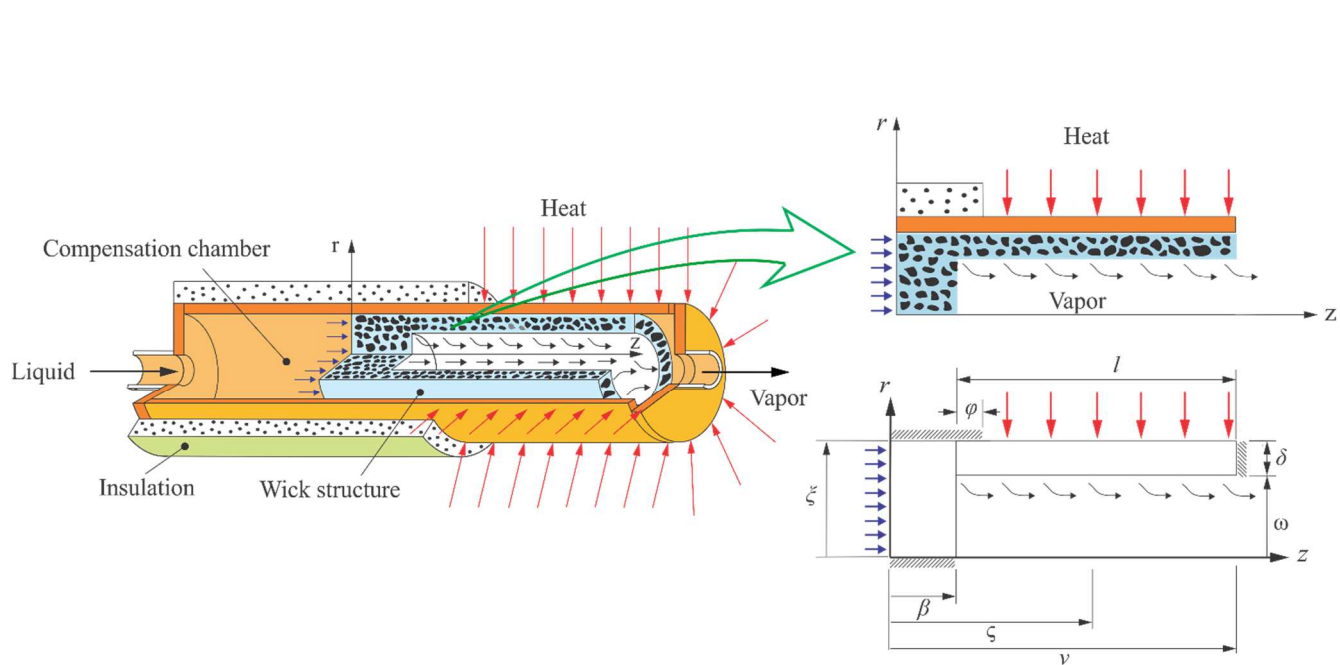
Figure 33 - Schematic of the evaporator.

4.1.2 Evaporator geometry analyses

In actual applications, LHPs must be designed to satisfy several operation requirements, including working temperatures, capacity of transferring heat for pre-established distances (between evaporators and condensers) and geometric limitations, due to the volume or area available for setting up the device.

The main criterion adopted to design the geometry (length and diameter) of the present studied LHP cylindrical evaporator is to provide, to the heat source, enough external area to capture the heat to be transferred. In addition, although pressure drops along the evaporator is not a subject treated in this work, the length of the evaporator must satisfy the capillary pumping requirements of the LHP. Actually, one should note that this wick must be thin enough to avoid the phase change to happen inside the structure and large enough to provide working fluid flow and capillary pumping capacity. However, it is not found in the literature any mathematical expression to be used in order to select the appropriate wick thickness δ. The present work develops an expression, based on geometric and thermophysical properties of the working fluid and porous media, which can be used as a criterion for the selection of the appropriate thickness of the porous media (wick) structure.

From the conservation of mass principle applied to the wick structure, the following relation can be obtained:

$$\dot{m}_i = \dot{m}_o \qquad (4.1)$$

where $\dot{m}_i$ and $\dot{m}_o$ represents the wick structure inlet and outlet working fluid mass flow rates, respectively. Two different velocity components are relevant in this model. The u axial velocity is related to the liquid flowing within the porous media and can be obtained from Darcy´s equation. The normal v velocity is related to the mass of liquid evaporated in the vapor-liquid interface and dependents on the heat flux that reaches that interface. Using these velocities, Equation (4.1) can be rewritten as:

$$\rho_l u A_n^z = \rho_l v A_n^r \qquad (4.2)$$

where A_n^z and A_n^r are the fluid flow normal areas, in the z and r directions and ρ_l is the liquid.

From Darcy´s law, one gets:

$$\frac{\partial P}{\partial z} = -\frac{\mu_l}{\kappa} u \qquad (4.3)$$

where μ_l is the fluid viscosity and κ is the permeability of the media.

From this equation, one can solve for the velocity to get:

$$u = -\frac{\kappa}{\mu_l}\frac{\partial P}{\partial z} \qquad (4.4)$$

It can be noted that this relation take into account the pressure drop within the wick structure.

The velocity v can be obtained from a mass balance on the meniscus liquid-vapor interface, assuming that all the heat supplied in the evaporator is used for the liquid-vapor phase change, in the meniscus interface. So, one gets:

$$\dot{m} = \frac{q}{h_{lv}} \qquad (4.5)$$

where h_{lv} is the latent heat of vaporization and q is the heat applied. Substituting the right side of Equation (4.2) in the above expression, one gets:

$$\rho_l v A_n^r = \frac{q}{h_{lv}} \qquad (4.6)$$

From the one-dimensional conduction heat transfer Fourier law, and considering k_{eff} as the effective thermal conductivity of the porous media, one gets:

$$q = -k_{eff} A_n^r \frac{dT}{dr} \qquad (4.7)$$

Substituting Equation (4.7) in Equation (4.6) yields:

$$v = -\frac{k_{eff}}{\rho_l h_{lv}}\frac{dT}{dr} \qquad (4.8)$$

Substituting Equations (4.4) and (4.8) in Equation (4.2), one gets:

$$\rho_l A_n^z \frac{\kappa}{\mu_l} \frac{dP}{dz} = \rho_l A_n^r \frac{k_{eff}}{\rho_l h_{lv}} \frac{dT}{dr} \qquad (4.9)$$

The following parameters are expected to have the order of magnitude of:

$$\Delta z \approx l, \Delta r \approx \delta, \Delta P \approx dP, \Delta T \approx dT, A_n^z \approx \delta w \text{ and } A_n^r \approx lw \qquad (4.10)$$

Substituting in Equation (4.9), and rearranging, one gets the following relation between the wick thickness and its length:

$$\left(\frac{\delta}{l}\right)^2 \approx \frac{k_{eff}}{\rho_l h_{lv}} \frac{\mu_l}{\kappa} \left(\frac{\Delta P}{\Delta T}\right)^{-1} \qquad (4.11)$$

Actually, the compensation chamber and the evaporator present slightly different saturated states, due to the temperature differences observed along the LHP. These saturation states are thermodynamically linked and must satisfy the relation (FAGHRI, 1995; KU, 1999; MAYDANIK *et al.*, 2011):

$$\Delta P = \left.\frac{dP}{dT}\right|_T \Delta T \qquad (4.12)$$

which, also, can be written as:

$$\frac{P_v - P_{cc}}{T_v - T_{cc}} = \left.\frac{dP}{dT}\right|_T \qquad (4.13)$$

where P_v and T_v are the pressure and temperature of the evaporator, while P_{cc} and T_{cc} are pressure and temperature of the compensation chamber, respectively. The term dP/dT is the slope of the pressure-temperature saturation line at T and this rate depends on the working fluid. High dP/dT values result in larger pressure gradients within the evaporator and so in larger evaporator capillary pumping capacity, resulting in larger temperature difference between the compensation chamber and the rest of the LHP. Therefore, it is evident that dP/dT characteristics of the working fluid must be considered in the geometry design of LHPs. The reference temperature T, for which the derivative is taken, can be adopted as the compensation chamber temperature, as suggested by Ku (1999), or as the average between the evaporator and compensation chamber temperatures, as proposed by Faghri (1995). In

the present work, the evaporator temperature is adopted as the reference operation temperature. Then, from Equation (4.13), the term $\Delta P/\Delta T$ can be expressed by:

$$\left(\frac{\Delta T}{\Delta P}\right) \approx \left(\frac{dP}{dT}\bigg|_T\right)^{-1} \tag{4.14}$$

Finally, Equation (4.11) can be written as:

$$\overbrace{\left(\frac{\delta}{l}\right)^2}^{geometry} \approx \underbrace{\frac{k_{eff}}{\kappa}}_{wick\ properties} \overbrace{\frac{\mu_l}{\rho_l h_{lv}}}^{fluid\ properties} \underbrace{\left(\frac{dP}{dT}\bigg|_T\right)^{-1}}_{Thermodynamic} \tag{4.15}$$

This equation provides a non-dimensional expression, involving geometry, capillary structure plus working fluid thermophysical properties and thermodynamic state of the working fluid, which can be used for the design of the wick structure thickness. The last term of Equation (4.15) can be calculated using the Clausius - Clapeyron Equation. In this work, the derivate of the pressure as function of the temperature is obtained from the FAGHRI (1995) polynomium.

One should note that the present model is useful not only to the LHP evaporator geometry under investigation in this work but also to conventional evaporators (FAGHRI, 1995; KU, 1999), see Figure 34, where Equation (4.15) can be used to determine the ratio between the evaporator wick thickness and its length l (δ/l), which guarantees the LHP start up.
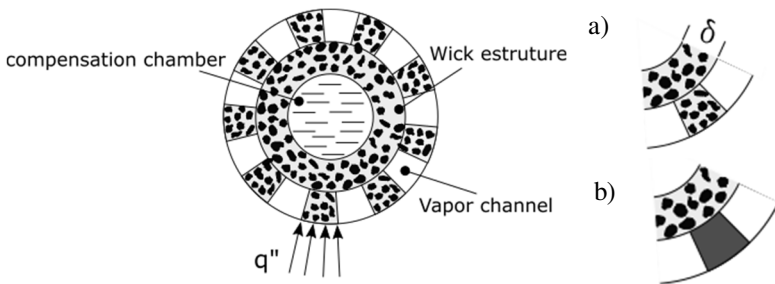
Figure 34 - Typical cross section of convectional evaporator of loop heat pipes a). Wick structure fin, b) solid fin.

4.2 Loop heap pipe evaporator mathematical models

As already mentioned, the porous media have two objectives: to provide a controlled means for working fluid evaporation and at the same time, to provide the capillary pumping necessary for conducting the fluid along the device. Therefore, the evaporator must be designed to guarantee that the heat delivered is able to reach the working fluid liquid–vapor meniscus formed, in the present configuration, in the most internal layer of the porous media. Also, the design should avoid vapor formation within the wick structure.

Therefore, thermal models for the temperature distribution within evaporator wick structure, able to predict the power transferred through the wick structure and the hot spots and hydraulic models, able to determine the pressure distribution (and so the pumping capacity of the evaporator) are important design tool of efficient LHP evaporators.

In the first part of this section, heat conduction models, to determine the temperature distribution and the heat transferred for the evaporator of LHPs are developed and presented. In the second part, hydraulic models able to predict the pressure distribution are developed and shown. These models are used in the design of evaporators of LHPs as discussed in the next chapter.

4.2.1 Wick structure thermal models

In the section, the wick, of thickness δ and length l which includes the heated and insulated lengths φ of the capillary pumping structure, and wick plug length β are modeled (see Figure 33). Two-dimensional cylindrical coordinates were adopted, with the z axis located in the axis of cylindrical wick and the r axis located radial to the wick thickness direction, resulting in the physical model shown in Figure 35.

The following hypotheses were adopted:
- Steady state conditions;
- Isotropic wick structure;
- Solid and liquid uniform thermophysical properties;
- The evaporator (T_v) and compensation chamber (T_{cc}) temperatures are prescribed, in saturation state, where $T_v > T_{cc}$.
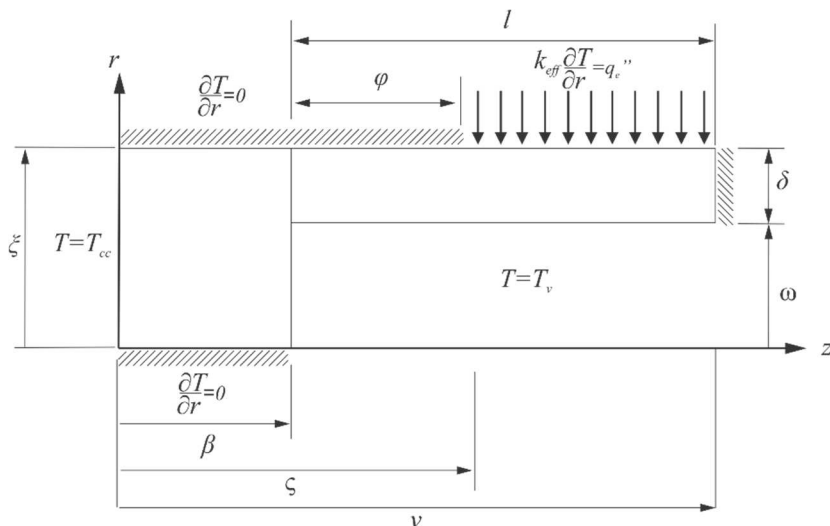
Figure 35 - Sketch of the evaporator thermophysical model.

The sketch of the heat transfer physical model, presented in Figure 35, shows the following boundary conditions:

- Prescribed temperature (T_l), at $z=0$. The working fluid within the compensation chamber, in its saturated state, contains both liquid and vapor phases.
- Thermal insulation at ($\partial T/\partial r = 0$), at $z=v$. This boundary condition means that the heat transfer is negligible at end of the evaporator wall.
- For $r = \xi$, thermal insulation ($\partial T/\partial z = 0$) for $0 < z < \beta$. This assumes that whole heat supplied in the heated surface is transferred or to the wick meniscus and or to the compensation chamber. The heat transfer in the wick plug and vapor regions interface is negligible.
- Heat flux is known ($k\,\partial T/\partial r = q''$, for $\varsigma < z < l$).
- Prescribed temperature (T_v), at $= \omega$. This temperature corresponds to the saturated temperature of the vapor produced in the meniscus interface.
- Liquid-vapor phase change happens only at the meniscus formed in the interface between liquid and vapor, in the wick structure ($r = \omega$) (FAGHRI, 1995).

- Heat is supplied to the evaporator external wall and reaches the liquid-vapor interface, due to the high thermal conductivity of the porous media solid matrix (FAGHRI, 1995). The physical mechanism is shown in Figure 36.
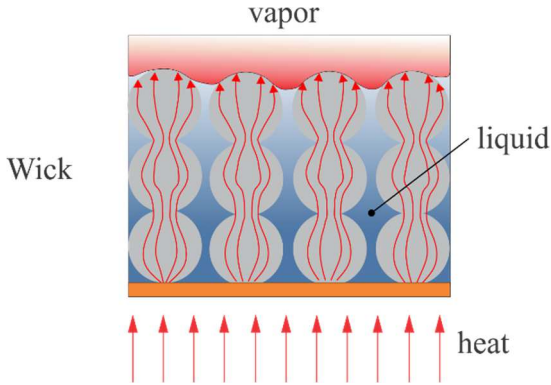
Figure 36 - Sketch of the evaporator thermophysical model.

- All the heat transferred by the wick structure to the liquid-vapor interface is used for changing the phase of the working fluid. Also, the evaporation thermal resistance is much lower than the conduction thermal resistance of the sintered porous media, which effective thermal conductivity is k_{eff}.

In this 2D model, the heat transfer through the evaporator case was neglected, in behalf of the design safety. A percentage of the heat flux is transferred through of case, but, by considering that the whole heat passes only through the wick structure, the maximum possible temperature is determined. As the actual temperature is lower than the calculated one, the liquid is colder that the saturation temperature, which is in favor of safety. Therefore, only the heat leak to the compensation chamber through the plug wick was considered. Adiabatic boundary condition at $z = \beta$ for $0 < r < \omega$ was assumed as the heat transfer in this face is small and so no evaporation is expected at this interface. This assumption considers that the whole working fluid flows through of surface at $z = \beta$ for $\omega < r < \xi$, and so, the maximum pressure drop is obtained.

Due to the non-uniformity of the evaporator geometry (one solid and another hollow cylinders), the problem was split in two, (region 3 for the hollow, and 1 and 2 for the solid cylinders) as shown in Figure 37. The solid cylinder problem is also divided in two sub-domains, 1 and 2 at $r=\omega$. The interface at z= β and $\omega < r < \xi$ (subdomain 2 e 3, see Figure 37) couples the solid and hollow cylinders. The boundary conditions in this interface is the following: first a heat flux is assumed for the solid cylinder, then the model resulting temperature distribution T_β (r), at z= β, $w < r < \xi$, is considered as the prescribed temperature distribution boundary condition for the hollow cylinder.
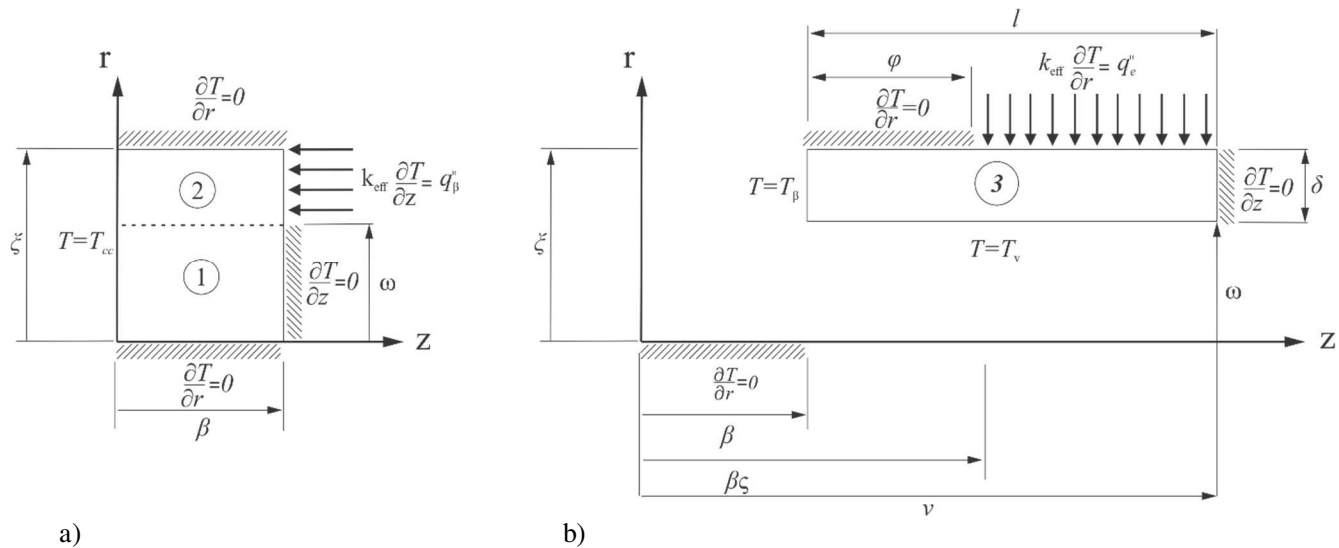
Figure 37 - Decomposition process of the thermal problem into two cylindrical geometries. a) Porous media plug, b) Evaporation section.

4.2.1.1 Solid cylinder

Equation (4.15) was used to design the wick geometry. However, the temperature distribution of the wick structure can be determined through the solution of Laplace´s equation, subjected to appropriate boundary conditions, using the separation of variables method (ARPACI; LARSEN, 1984).

Laplace´s equation solution can be simplified if the boundary conditions are homogeneous. For this purpose, the following temperature variable is proposed:

$$\theta = T - T_c \qquad (4.16)$$

resulting in:

$$\frac{\partial^2 \theta}{\partial r^2} + \frac{1}{r}\frac{\partial \theta}{\partial r} + \frac{\partial^2 \theta}{\partial z^2} = 0 \qquad (4.17)$$
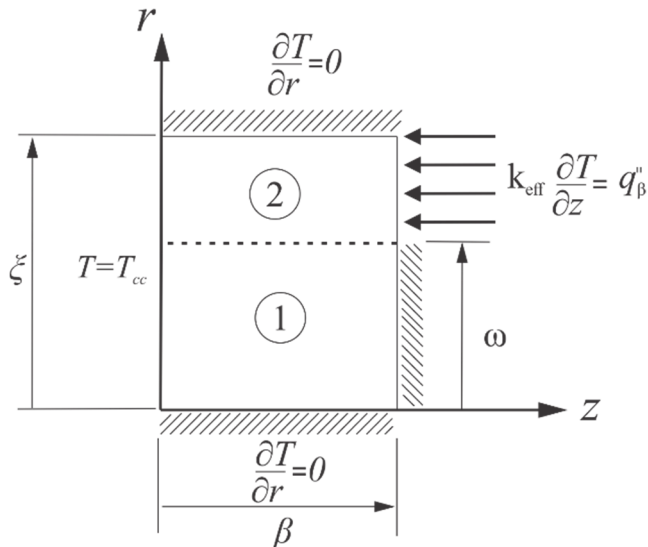
Figure 38 - Sketch of the evaporator plug thermophysical model.

In Figure 38, the sketch of the evaporator plug (solid cylinder) physical model, which, as already mentioned, is split into two regions (1 and 2), using the new temperature variable and so with the resulting homogeneous boundary condition in $z = 0$, is presented.
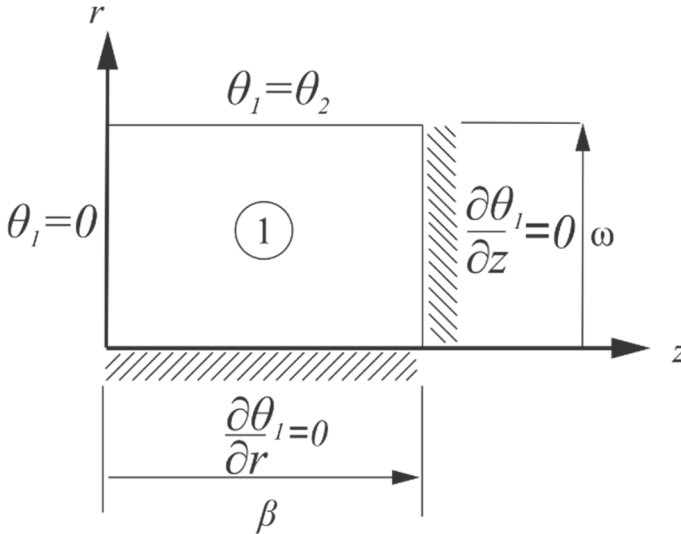
Figure 39 - Boundary conditions applied for the thermal problem 1.

In Figure 39, subdomain 1 of Figure 37 is presented. This conduction heat transfer problem can be formulated as

$$\frac{\partial^2 \theta_1}{\partial r^2} + \frac{1}{r}\frac{\partial \theta_1}{\partial r} + \frac{\partial^2 \theta_1}{\partial z^2} = 0 \quad in \ 0 < r < \xi , 0 < z < \beta \quad (4.18)$$

Subjected to the following boundary conditions:

$$\frac{\partial \theta_1(0,z)}{\partial r} = 0 \qquad (4.19)$$

$$\theta_1(\omega,z) = \theta_{2a}(\omega,z) \qquad (4.20)$$

$$\theta_1(r,0) = 0 \qquad (4.21)$$

$$\frac{\partial \theta_1(r,\beta)}{\partial z} = 0 \qquad (4.22)$$

According to Poulikakos (1994), the general solution for this problem is:

$$Z = A\cos(\lambda_m z) + B\sin(\lambda_m z) \qquad (4.23)$$

$$R = CI_0(\lambda_m r) + DK_0(\lambda_m r) \qquad (4.24)$$

Combining the equations yields

$$\theta_1(r,z)_1 = \sum_{m=1}^{\infty} L_m I_0(\lambda_m r)\sin(\lambda_m z) \qquad (4.25)$$

where

$$\lambda_m = \frac{(2n-1)\pi}{2}\frac{1}{\beta} \qquad (4.26)$$

On the other hand, it is displayed in the Figure 40, the physical model for the subdomain 2 conduction heat transfer problem.
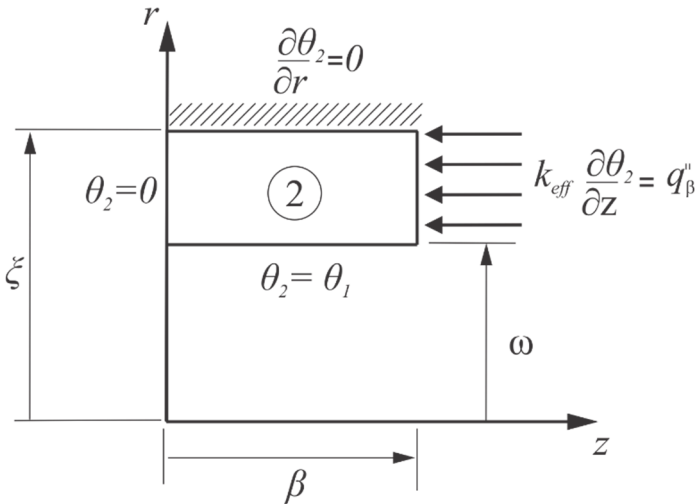
Figure 40 - Boundary conditions applied for the thermal problem: due to the non-uniform boundary conditions, the problem is split in two.

Similarly, the problem 2 is also modeled using the Laplace equation:

$$\frac{\partial^2 \theta_2}{\partial r^2} + \frac{1}{r}\frac{\partial \theta_2}{\partial r} + \frac{\partial^2 \theta_2}{\partial z^2} = 0 \quad in \ \omega < r < \xi, 0 < z < \beta \quad (4.27)$$

With boundary conditions:

$$\frac{\partial \theta_2(\xi, z)}{\partial r} = 0 \tag{4.28}$$

$$\theta_1(\omega, z) = \theta_2(\omega, z) \tag{4.29}$$

$$\theta_2(r, 0) = 0 \tag{4.30}$$

$$\frac{\partial \theta_2(r, \beta)}{\partial z} = \frac{q_\beta{}''}{k_{eff}} \tag{4.31}$$

Due to the fact that this problem contains two non-homogeneous boundary conditions, the superposition method is applied and the problem is again divided in two, Problems 2a and 2b, each one with just one non-homogeneous boundary condition (see Figure 41).

$$\frac{\partial \theta_{2a}}{\partial r} = 0$$

$$\frac{\partial \theta_{2a}}{\partial z} = 0$$

$$\theta_{2a} = 0$$

(2a)

$$\theta_{2a} = \theta_1$$

$$\xi$$

$$\omega$$

$$\beta$$

$$+$$

$$\frac{\partial \theta_{2b}}{\partial r} = 0$$

$$k_{eff} \frac{\partial \theta_{2b}}{\partial z} = {}^{"}q_{\beta}$$

$$\theta_{2b} = 0$$

(2b)

$$\theta_{2b} = 0$$

$$\xi$$

$$\omega$$

$$\beta$$
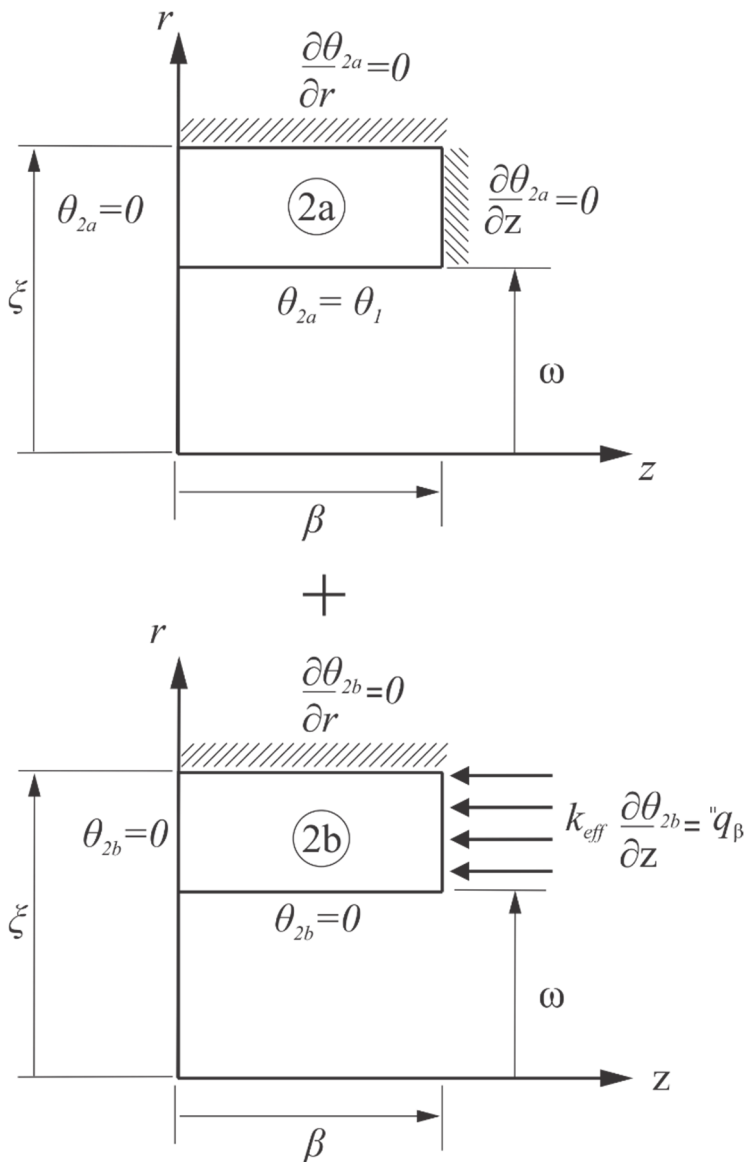
Figure 41 - Decomposition process of the thermal problem 2 solved by superposition.

The formulation of problem 2a according to the Figure 41 is

$$\frac{\partial^2 \theta_{2a}}{\partial r^2} + \frac{1}{r}\frac{\partial \theta_{2a}}{\partial r} + \frac{\partial^2 \theta_{2a}}{\partial z^2} = 0 \quad in \; \omega < r < \xi, 0 < z < \beta \qquad (4.32)$$

Subject to the boundary conditions:

$$\frac{\partial \theta_{2a}(\xi, z)}{\partial r} = 0 \qquad (4.33)$$

$$\theta_{2a}(\omega, z) = \theta_1(\omega, z) \qquad (4.34)$$

$$\theta_{2a}(r, 0) = 0 \qquad (4.35)$$

$$\frac{\partial \theta_{2a}(r, \beta)}{\partial z} = 0 \qquad (4.36)$$

The general solution for this problem 2a is:

$$Z = A cos(\zeta_m z) + B sin(\zeta_m z) \qquad (4.37)$$

$$R = CI_0(\zeta_m r) + DK_0(\zeta_m r) \qquad (4.38)$$

Applying the boundary conditions (Equations (4.33), (4.34), (4.35) and (4.36)) and combining the Equations (4.37) and (4.38), the following solutions is obtained:

$$\theta(r, z)_{2a} = \sum_{m=1}^{\infty} M_m \left[\frac{K_1(\zeta_m \xi)}{I_1(\zeta_m \xi)} I_0(\zeta_n r) + K_0(\zeta_n r) \right] sin(\zeta_m z) \quad (4.39)$$

where

$$\zeta_m = \frac{(2m - 1)}{2}\frac{\pi}{\beta} \qquad (4.40)$$

Similarly, the formulation of problem 2b, which schematic of the physical model is shown in Figure 41 is:

$$\frac{\partial^2 \theta_{2b}}{\partial r^2} + \frac{1}{r}\frac{\partial \theta_{2b}}{\partial r} + \frac{\partial^2 \theta_{2b}}{\partial z^2} = 0 \quad in \; \omega < r < \xi, 0 < z < \beta \qquad (4.41)$$

subjected to the boundary conditions:

$$\frac{\partial \theta_{2b}(\xi, z)}{\partial r} = 0 \tag{4.42}$$

$$\theta_{2b}(\omega, z) = 0, \tag{4.43}$$

$$\theta_{2b}(r, 0) = 0 \tag{4.44}$$

$$\frac{\partial \theta_{2b}(r, \beta)}{\partial z} = \frac{q_\beta''}{k_{eff}} \tag{4.45}$$

The general solution for this problem is:

$$Z = A\cosh(\eta_m z) + B\sinh(\eta_m z) \tag{4.46}$$

$$R = CJ_0(\eta_m r) + DY_0(\eta_m r) \tag{4.47}$$

Substituting the boundary condition, Equations (4.42), (4.43), (4.44) and (4.45) and combining the las two equations, one get the following transcendental equation:

$$\frac{Y_0(\eta_m \omega)}{J_0(\eta_m \omega)} = \frac{Y_1(\eta_m \xi)}{J_1(\eta_m \xi)} \tag{4.48}$$

Therefore, the following temperature distribution equation is obtained:

$$\theta(r, z)_{2b} = \sum_{m=1}^{\infty} N_n \left[-\frac{Y_0(\eta_m \omega)}{J_0(\eta_m \omega)} J_0(\eta_m r) + Y_0(\eta_m r) \right] \sinh(\eta_m r) \tag{4.49}$$

where the η_m parameters are the roots of Equation (4.48), given by:

$$N_m = \frac{\frac{q_\beta''}{k_{eff}}}{\eta_m \cosh(\eta_m \beta)} \frac{\int_\omega^\xi \left[-\frac{Y_0(\eta_m \omega)}{J_0(\eta_m \omega)} J_0(\eta_m r) + Y_0(\eta_m r) \right] r \, dr}{\int_\omega^\xi \left[-\frac{Y_0(\eta_m \omega)}{J_0(\eta_m \omega)} J_0(\eta_m r) + Y_0(\eta_m r) \right]^2 r \, dr} \tag{4.50}$$

The two domains, 2a and 2b, are coupled through the $r = \omega$ interface, or:

$$\theta(r,z)_{2a} = \theta(r,z)_{2b} \tag{4.51}$$

Substituting Equations (4.25) and (4.39) in the Equation (4.51), one gets:

$$\sum_{m=1}^{\infty} L_m I_0(\lambda_m r) \sin(\lambda_m z)$$
$$= \sum_{n=1}^{\infty} M_n \left[\frac{K_1(\zeta_m \xi)}{I_1(\zeta_m \xi)} I_0(\zeta_m r) \right. \tag{4.52}$$
$$\left. - K_0(\zeta_m r) \right] \sin(\zeta_m z)$$

where M_m is defined as:

$$M_m = \frac{I_0(\lambda_m r)}{\left[\frac{K_1(\zeta_m \xi)}{I_1(\zeta_m \xi)} I_0(\zeta_m r) - K_0(\zeta_m r) \right]} L_m \tag{4.53}$$

Now, from the energy conservation principle at the interface, one has:

$$\frac{\partial \theta_1(r,z)}{\partial r} = \frac{\partial \theta_2(r,z)}{\partial r} \tag{4.54}$$

Due to the subdivision of region 2, one gets:

$$\frac{\partial \theta_{1a}(r,z)}{\partial r} = \frac{\partial \theta_{2a}(r,z)}{\partial r} + \frac{\partial \theta_{2b}(r,z)}{\partial r} \tag{4.55}$$

Differentiating and substituting the temperature solutions (Equations (4.25) and (4.39) into Equation (4.54), the following expression is obtained:

$$\sum_{m=1}^{\infty} L_m \lambda_m I_1(\lambda_m \omega) \sin(\lambda_m z)$$
$$= \sum_{m=1}^{\infty} M_m \zeta_m \left[\frac{K_1(\zeta_m \xi)}{I_1(\zeta_m \xi)} I_1(\zeta_m \omega) \right.$$
$$\left. - K_1(\zeta_m \omega) \right] \sin(\zeta_m z) \tag{4.56}$$
$$+ \sum_{m=1}^{\infty} N_m \eta_m \left[\frac{Y_0(\eta_m \omega)}{J_0(\eta_m \omega)} J_1(\eta_m \omega) \right.$$
$$\left. - Y_1(\eta_m \omega) \right] \sinh(\eta_m z)$$

Ordering the terms of Equation (4.56) and applied the orthogonally properties we can be rewrite as

$$\underbrace{\sum_{n=1}^{\infty} N_n \left[\frac{Y_0(\eta_n\omega)}{J_0(\eta_n\omega)}J_1(\eta_n\omega) - Y_1(\eta_n\omega)\right]\sinh(\eta_n z)}_{f(z)}$$
$$= \sum_{m=1}^{\infty} \hat{L}_m \sin(\lambda_m z) \tag{4.57}$$

where the following parameter is defined:

$$\hat{L}_m = \frac{\sum_{n=1}^{\infty} N_n\left[\frac{Y_0(\eta_n\omega)}{J_0(\eta_n\omega)}J_1(n\omega) - Y_1(\eta_n\omega)\right]\int_0^\omega \sinh(\eta_n z)\sin(\lambda_m z)dz}{\int_0^\omega \sin^2(\lambda_m z)dz}, \tag{4.58}$$

where,

$$\hat{L}_m$$
$$= \left\{\lambda_m I_1(\lambda_m\omega)\right.$$
$$\left. - \frac{I_0(\lambda_m r)\left[\frac{K_1(\zeta_m\xi)}{I_1(\zeta_m\xi)}I_1(\zeta_m\omega) - K_1(\zeta_m\omega)\right]}{\left[\frac{K_1(\zeta_m\xi)}{I_1(\zeta_m\xi)}I_0(\zeta_m r) - K_0(\zeta_m r)\right]}\right\} L_m \tag{4.59}$$

Finally, the matching of Equation (4.58) with Equations (4.59) and (4.53) yields:

$$L_m = \frac{\sum_{n=1}^{\infty} N_n\left[\frac{Y_0(\eta_n\omega)}{J_0(\eta_n\omega)}J_1(n\omega) - Y_1(\eta_n\omega)\right]\int_0^\omega \sinh(\eta_n z)\sin(\lambda_m z)dz}{\lambda_m I_1(\lambda_m\omega) - \frac{I_0(\lambda_m r)\left[\frac{K_1(\zeta_m\xi)}{I_1(\zeta_m\xi)}I_1(\zeta_m\omega) - K_1(\zeta_m\omega)\right]}{\left[\frac{K_1(\zeta_m\xi)}{I_1(\zeta_m\xi)}I_0(\zeta_m r) - K_0(\zeta_m r)\right]}\int_0^\omega \sin^2(\lambda_m z)dz}, \tag{4.60}$$

4.2.1.2 Hollow cylinder

Considering now the hollow cylinder region 3 (see Figure 37). The temperature T is modeled using Laplace´s equation:

$$\frac{\partial^2 T}{\partial r^2} + \frac{1}{r}\frac{\partial T}{\partial r} + \frac{\partial^2 T}{\partial z^2} = 0 \tag{4.61}$$

Figure 42 shows the schematic of problem 3.
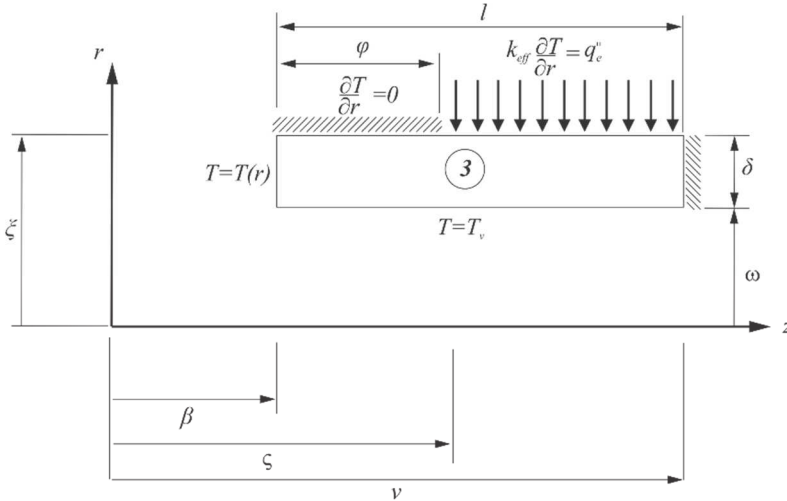
Figure 42 - Schematic mathematical model of the thermal problem 3.

As the boundary condition at $z = \beta$, $r = \omega$ and $r = \xi$ are non-uniform, the superposition method can be used to solve this problem. Therefore, the problem is divided in three (3a, 3b and 3c), with uniform boundary conditions, as shown in Figure 43.
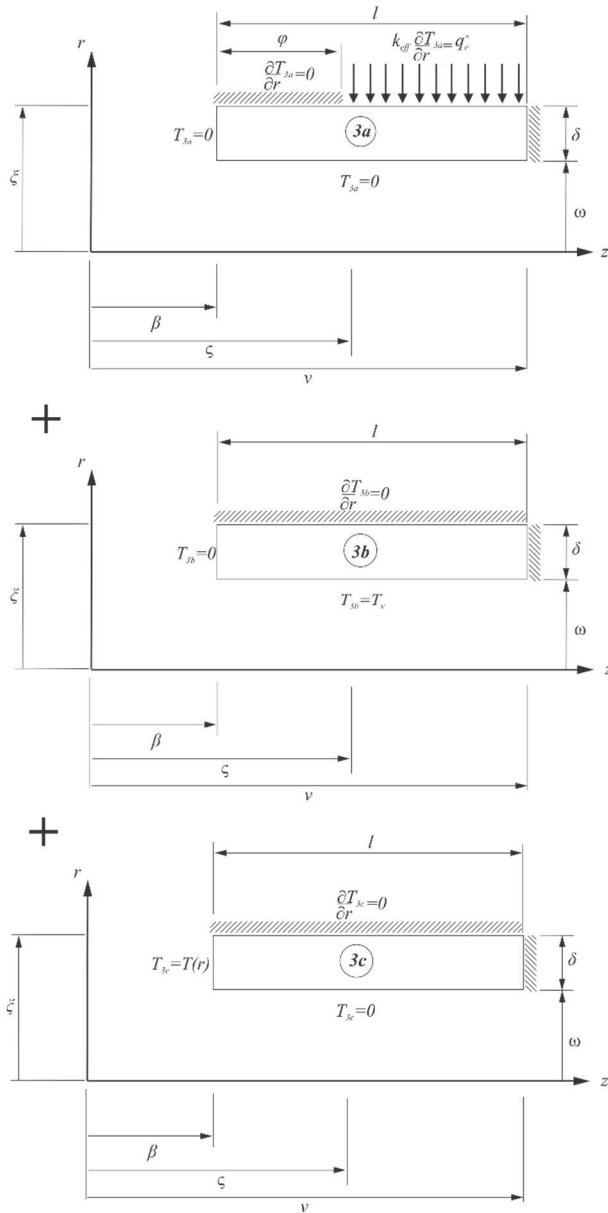
Figure 43 - Schematics of the superposition solution for the thermal problem 3.

The formulation of the Problem 3a (see Figure 43) is therefore:

$$\frac{\partial^2 T_{3a}}{\partial r^2} + \frac{1}{r}\frac{\partial T_{3a}}{\partial r} + \frac{\partial^2 T_{3a}}{\partial z^2} = 0 \quad in \; \omega < r < \xi \, , \beta < z < \upsilon \quad (4.62)$$

Subjected to the boundary conditions:

$$\frac{\partial T_{3a}(r,z)}{\partial r} = \begin{cases} 0, & \beta < z < \varsigma \\ \dfrac{q_e''}{k_{eff}}, & \varsigma < z < \upsilon \end{cases} at\, r = \xi \qquad (4.63)$$

$$T_{3a}(\omega, z) = 0 \qquad\qquad (4.64)$$

$$T_{3a}(r, \beta) = 0 \qquad\qquad (4.65)$$

$$\frac{\partial T_{3a}(r, \upsilon)}{\partial z} = 0 \qquad\qquad (4.66)$$

Solutions found for this boundary conditions show indeterminations in the solution due to the hyperbolic function when the eigenvalues become infinity. Therefore, in the solutions presented below, the boundary condition in $z = \beta$ was displaced to $z = 0$ and new dimensions $l = \upsilon - \beta$ and $\varphi = \varsigma - \beta$ were defined for the problems 3a, 3b and 3c. However, the information of original problem is conserved. Using the separation of variables method, the general solution for this problem is:

$$Z = A\cos(\vartheta_n z) + B\sin(\vartheta_n z) \qquad (4.67)$$

$$R = CJ_0(\vartheta_n r) + DY_0(\vartheta_n r) \qquad (4.68)$$

where the eigenvalues are given by:

$$\vartheta_n = \frac{(2n-1)\,\pi}{2}\frac{1}{l} \qquad\qquad (4.69)$$

Therefore, the solution for the temperature distribution for problem 3 is:

$$T(r,z)_{3a} = \sum_{n=1}^{\infty} O_n \left[-\frac{K_0(\vartheta_n\omega)}{I_0(\vartheta_n\omega)} I_0(\vartheta_n r) \right.$$
$$\left. + K_0(\vartheta_n r) \right] \sin(\vartheta_n z) \tag{4.70}$$

With

$$O_n = \frac{\frac{q_e''}{k_{eff}}}{\vartheta_n \left[-\frac{K_0(\vartheta_n\omega)}{I_0(\vartheta_n\omega)} I_1(\vartheta_n\xi) - K_1(\vartheta_n\xi) \right]} \frac{\int_\varphi^l \sin(\vartheta_n z)dz}{\int_0^l \sin^2(\vartheta_n z)dz} \tag{4.71}$$

The problem 3b, which schematic is given in Figure 43 is formulated as follows:

$$\frac{\partial^2 T_{3b}}{\partial r^2} + \frac{1}{r}\frac{\partial T_{3b}}{\partial r} + \frac{\partial^2 T_{3b}}{\partial y^2} = 0 \quad in\ \omega < r < \xi , \beta < z < \upsilon \tag{4.72}$$

$$\frac{\partial T_{3b}(r,z)}{\partial r} = 0 \ at\ r = \xi \tag{4.73}$$

$$T_{3b}(\omega,z) = T_\upsilon \tag{4.74}$$

$$T_{3b}(r,\beta) = 0 \tag{4.75}$$

$$\frac{\partial T_{3b}}{\partial z} = 0 \ at\ z = \upsilon \tag{4.76}$$

The general solution for this problem is:

$$Z = Acos(\chi_n z) + Bsin(\chi_n z) \tag{4.77}$$
$$R = CI_0(\chi_n r) + DK_0(\chi_n r) \tag{4.78}$$

where the eigenvalues χ_n is calculated from the following equation:

$$\chi_n = \frac{(2n-1)}{2}\frac{\pi}{l} \tag{4.79}$$

Substituting the boundary conditions (equations (4.73), (4.74), (4.75) and (4.76) and combining the equations (4.77), (4.78) and (4.79) the following temperature distribution is obtained:

$$T(r,z)_{3b} = \sum_{n=1}^{\infty} P_n \left[\frac{K_1(\chi_n\xi)}{I_1(\chi_n\xi)} I_0(\chi_n r) + K_0(\chi_n r) \right] \sin(\chi_n z) \tag{4.80}$$

where

$$P_n = \frac{T_v}{\left[\frac{K_1(\chi_n\xi)}{I_1(\chi_n\xi)} I_0(\chi_n\omega) + K_0(\chi_n\omega)\right]} \frac{\int_0^l \sin(\chi_n z)\, dz}{\int_0^l [\sin(\chi_n z)]^2\, dz} \tag{4.81}$$

Finally, problem 3c, which schematic is given in Figure 43 is formulated as follows:

$$\frac{\partial^2 T_{3c}}{\partial r^2} + \frac{1}{r}\frac{\partial T_{3c}}{\partial r} + \frac{\partial^2 T_{3c}}{\partial z^2} = 0 \quad in \; \omega < r < \xi, \beta < z < v \tag{4.82}$$

$$\frac{\partial T_{3b}(\xi, z)}{\partial r} = 0 \tag{4.83}$$

$$T_{3c}(\omega, z) = 0 \tag{4.84}$$

$$T_{3c}(r, \beta) = T(r) \tag{4.85}$$

$$\frac{\partial T_{3c}(r, v)}{\partial z} = 0 \tag{4.86}$$

The general solution for this problem is:

$$Z = A cosh(Ш_n z) + B sinh(Ш_n z) \tag{4.87}$$

$$R = C J_0(Ш_n r) + D Y_0(Ш_n r) \tag{4.88}$$

where the eigenvalues $Щ_n$ are calculated from transcendental equation:

$$\frac{Y_o(Щ_n\omega)}{J_o(Щ_n\omega)} = \frac{Y_1(Щ_n\xi)}{J_1(Щ_n\xi)} \tag{4.89}$$

Substituting the boundary conditions (Equations (4.83) (4.84), (4.85) and (4.86)) and combining the Equations (4.87), (4.88) and (4.89) the following temperature distribution is obtained:

$$T(r,z)_{3c} = \sum_{n=1}^{\infty} Q_n \left[-\frac{Y_0(Щ_n\xi)}{J_0(Щ_n\xi)} J_0(Щ_n r) + Y_0(Щ_n r) \right] \cosh\big(Щ_n(z-l)\big) \tag{4.90}$$

where

$$Q_n = \frac{1}{\cosh(Щ_n l)} \frac{\int_{\omega}^{\xi} T(r) \left[-\frac{Y_0(Щ_n\xi)}{J_0(Щ_n\xi)} J_0(Щ_n r) + Y_0(Щ_n r) \right] r dr}{\int_{\omega}^{\xi} \left[-\frac{Y_0(\chi_n\xi)}{J_0(\chi_n\xi)} J_0(Щ_n r) + Y_0(Щ_n r) \right]^2 r\, dr} \tag{4.91}$$

4.2.1.3 Energy balance

As already mentioned, a well-designed evaporator must assure that most of the energy delivered to the evaporator is used to evaporate the working fluid in the liquid-vapor interface in the wick. This means that the heat should not flow to any other LHP component, especially the compensation chamber, where the heat leakage would increase the liquid temperature and so its pressure, decreasing the pressure drops along the LHP sections, which would, eventually prevent LHP operation or its start up. The present model provides a tool to verify, from the total energy delivered to the evaporator, the amount that is transferred to the liquid-vapor meniscus (conducted through the porous media hollow cylinder) and the heat lost to the compensation chamber (through the plug solid cylinder).

In steady state conditions, a simple heat balance within the evaporator establishes that the total energy delivered to the evaporator. This heat energy can be split into the one transferred to the meniscus interface $q_r|_{r=\omega}$ (domain 3) and the other lost to the compensation chamber q_β (passing through the interface between the porous media and the compensation chamber, $q_z|_{z=\beta}$), which gives:

$$q_e = q_r|_{r=\omega} + q_z|_{z=\beta} \tag{4.92}$$

Fourier Equation can be used to determine the heat transferred at both these interfaces, using the space derivatives of the temperature distribution expressions, obtained from the analytical models (Equations (4.70) and (4.80)), which is integrated along these surfaces. Actually, the heat leakage to the compensation chamber can be calculated by two means: considering the interface of the two cylinders or integrating the temperature distribution (Fourier law) along the cross-section area of the solid cylinder, at any point z_i.

The heat transfer in $z = z_i$ is

$$q = q_1 + q_2, \tag{4.93}$$

where q_1 and q_2 are heat that flow through each subdomain 1 and 2 respectability.

$$q_1 = \int_0^\omega k_{eff} \frac{\partial \theta_1}{\partial z}\bigg|_{z_i} 2\pi r dr \tag{4.94}$$

$$q_1 = 2\pi k_{eff} \sum_{m=1}^{\infty} \lambda_m L_m cos(\lambda_m z_i) \int_0^\omega I_0(\lambda_m r) r dr \tag{4.95}$$

and

$$q_2 = q_{2a} + q_{2b} \tag{4.96}$$

$$q_2 = 2\pi k_{eff} \int_\omega^\xi \left.\frac{\partial \theta_{2a}}{\partial z}\right|_{z_i} rdr + 2\pi k_{eff} \int_\omega^\xi \left.\frac{\partial \theta_{2b}}{\partial z}\right|_{z_i} rdr \qquad (4.97)$$

resulting in:

$$q_{2a} = 2\pi k_{eff} \sum_{m=1}^\infty \zeta_m M_m cos(\zeta_m z_i) \int_\omega^\xi \left[\frac{K_1(\zeta_m \xi)}{I_1(\zeta_m \xi)} I_0(\zeta_m r)\right.$$
$$\left. + K_0(\zeta_m r)\right] I_0(\zeta_m r) rdr \qquad (4.98)$$

$$q_{2b} = 2\pi k_{eff} \sum_{m=1}^\infty \eta_m N_m cosh(\eta_m z_i) \int_\omega^\xi \left[-\frac{Y_0(\eta_m \xi)}{J_0(\eta_m \xi)} J_0(\eta_m r)\right.$$
$$\left. + Y_0(\eta_m r)\right] rdr \qquad (4.99)$$

Similarly, the heat transferred in $z = \beta$ is the sum of q_{3a} and q_{3b} and q_{3c}, or:

$$q_\beta = \int_\omega^\xi k_{eff} \left.\frac{\partial \theta_{3a}}{\partial z}\right|_\beta 2\pi rdr$$
$$+ \int_\omega^\xi k_{eff} \left.\frac{\partial \theta_{3b}}{\partial z}\right|_\beta 2\pi rdr \qquad (4.100)$$
$$+ \int_\omega^\xi k_{eff} \left.\frac{\partial \theta_{3c}}{\partial z}\right|_\beta 2\pi rdr$$

where

$$q_{3a} = 2\pi k_{eff} \sum_{n=1}^\infty \vartheta_n O_m cos(\vartheta_n 0) \int_\omega^\xi \left[-\frac{K_0(\vartheta_n \omega)}{I_0(\vartheta_n \omega)} I_0(\vartheta_n r)\right.$$
$$\left. + K_0(\vartheta_n r)\right] rdr \qquad (4.101)$$

$$q_{3b} = 2\pi k_{eff} \sum_{n=1}^{\infty} \chi_n P_n cos(\chi_n 0) \int_{\omega}^{\xi} \left[\frac{K_1(\chi_n \xi)}{I_1(\chi_n \xi)} I_0(\chi_n r) \right.$$
$$\left. + K_0(\chi_n r) \right] r dr \tag{4.102}$$

$$q_{3c}$$
$$= -2\pi k_{eff} \sum_{n=1}^{\infty} Щ_n Q_n sinh(Щ_n l) \int_0^l \left[\frac{Y_0(Щ_n \xi)}{J_0(Щ_n \xi)} J_0(Щ_n r) \right.$$
$$\left. - Y_0(Щ_n r) \right] r dr \tag{4.103}$$

Now, the heat transferred in the liquid vapor meniscus interface is also determined from the problem 3a, 3b an 3c:

$$q_\omega = \int_\beta^\upsilon k_{eff} 2\pi\omega \left. \frac{\partial \theta_{3a}}{\partial r} \right|_\omega dz$$
$$+ \int_\beta^\upsilon k_{eff} 2\pi\omega \left. \frac{\partial \theta_{3b}}{\partial r} \right|_\omega dz \tag{4.104}$$
$$+ \int_\beta^\upsilon k_{eff} 2\pi\omega \left. \frac{\partial \theta_{3c}}{\partial r} \right|_\omega dz$$

which gives:

$$q_{3a} = 2\pi\omega k_{eff} \sum_{n=1}^{\infty} \vartheta_n O_m \left[-\frac{K_0(\vartheta_n \omega)}{I_0(\vartheta_n \omega)} I_1(\vartheta_n \omega) \right.$$
$$\left. - K_1(\vartheta_n \omega) \right] \int_0^l sin(\vartheta_n z) dz \tag{4.105}$$

and,

$$q_{3b} = 2\pi\omega k_{eff} \sum_{n=1}^{\infty} \chi_n P_n \left[\frac{K_1(\chi_n \xi)}{I_1(\chi_n \xi)} I_1(\chi_n \omega) \right.$$
$$\left. - K_1(\chi_n \omega) \right] \int_0^l sin(\chi_n z) dz \tag{4.106}$$

and,

$$q_{3c} = 2\pi\omega k_{eff} \sum_{n=1}^{\infty} Щ_n Q_n \left[\frac{Y_0(Щ_n\xi)}{J_0(Щ_n\xi)} J_1(Щ_n\omega) \right.$$
$$\left. - Y_1(Щ_n\omega)\right] \int_0^l \cosh(Щ_n(z-l))dz \tag{4.107}$$

In the following section, the temperature field for a wick evaporator structure is determined using the set of equations developed in this section. The heat leak and heat used to evaporate the working fluid are also determined. A wick structure coupled to condenser, and liquid and vapor lines are modeled for one operation condition.

4.2.2 Pressure distribution models

The hydraulic behavior of the porous structure is modeled aiming the development of a tool for designing LHP wicks which are able to promote the working fluid pumping and phase change along the loop (see Figure 44). The following hypothesis were adopted:

- The liquid-vapor phase change happens only at the interface between liquid and vapor, in the wick structure, according to Faghri (1995). It is considered that the heat supplied to the evaporator reaches the liquid-vapor interface due to the high thermal conductivity of the solid matrix in the porous media Flórez *et al.* (2013).
- All the heat transferred by the wick structure to the liquid-vapor interface is used for the working fluid phase change; therefore, the evaporation thermal resistance is much smaller than the conductance thermal resistance through the sintered porous media.
- The fluid has uniform velocity within the compensation chamber.
- The working fluid is incompressible.
- Gravity effects are negligible.
- The fluid that flows within the wick structure is laminar and has Reynolds number Re < 1 (DYBBS; EDWARDS, 1984), therefore Darcy´s equation is applied. The Reynolds number is based on the average velocity within the pore and its characteristic dimension is the pore diameter.

Similar to the temperature distributions, the pressure field is also obtained from the solution of Laplace's Equation, which results from the

mass conservation principle and the Darcy law applied for each component of the coordinate system (BEJAN, 2013; FAGHRI, 1995).
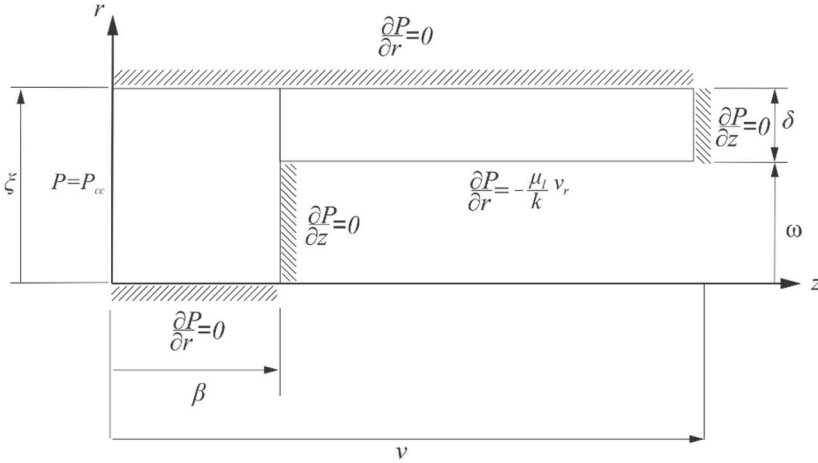
Figure 44 - Sketch of the evaporator hydraulic model.

The velocity is assumed to be

$$V = \hat{e}_r V_r + \hat{e}_\theta V_\theta + \hat{e}_k V_z, \qquad (4.108)$$

The Darcy law can be written, in vector notation, as:

$$V = -\left(\frac{\bar{\bar{k}}}{\mu}\right)\nabla P, \qquad (4.109)$$

Where ∇P is the gradient of pressure, expressed in cylindrical coordinates as

$$\nabla P = \hat{e}_r \frac{\partial P}{\partial r} + \hat{e}_\theta \frac{1}{r}\frac{\partial P}{\partial \theta} + \hat{e}_k \frac{\partial P}{\partial z} \qquad (4.110)$$

$\bar{\bar{k}}$ is the permeability tensor and μ is the dynamic viscosity of the fluid. Substituting the Equation (4.110) into the Equation (4.109) and matching with the Equation (4.108)(4.115) , one can have:

$$\hat{e}_r V_r + \hat{e}_\theta V_\theta + \hat{e}_k V_z = -\left(\frac{\bar{\bar{k}}}{\mu}\right)\left(\hat{e}_r \frac{\partial P}{\partial r} + \hat{e}_\theta \frac{1}{r}\frac{\partial P}{\partial \theta} + \hat{e}_k \frac{\partial P}{\partial z}\right) \quad (4.111)$$

The velocity components of fluid can be obtained from the Darcy´s Law. For an isotropic medium, the tensor of the permeability becomes a zeroth order tensor (scalar):

$$V_r = -\left(\frac{k}{\mu}\right)\frac{\partial P}{\partial r}, V_\theta = -\left(\frac{k}{\mu}\right)\frac{1}{r}\frac{\partial P}{\partial \theta}, V_z = -\left(\frac{k}{\mu}\right)\frac{\partial P}{\partial z} \qquad (4.112)$$

Substituting the Equation (4.112)(4.119) components of velocity in the following conservation of mass equation in cylindrical coordinates one gets:

$$\frac{\partial \rho}{\partial t} + \frac{1}{r}\frac{\partial(\rho r V_r)}{\partial \theta} + \frac{1}{r}\frac{\partial(\rho V_r)}{\partial \theta} + \frac{\partial(\rho V_z)}{\partial z} = 0 \qquad (4.113)$$

resulting in a steady state Laplace equation for the pressure field, for the wick structure,

$$\frac{\partial^2 P}{\partial r^2} + \frac{1}{r}\frac{\partial P}{\partial r} + \frac{\partial^2 P}{\partial z^2} = 0 \qquad (4.114)$$

As the geometry is non-uniform (solid and hollow cylinders), the problem is split into two, one hollow and one solid cylinder, as shown in Figure 45. The solid cylinder is also divided into two regions (problems 4 and 5), to accommodate the non-uniform boundary condition at $z = \beta$.

4.2.2.1 Hydraulic pressure distribution for solid wick structure

The solution of the bidimensional Laplace equation requires four boundary conditions. Figure 45 shows these boundary conditions for the solid cylinder, which are: prescribed compensation chamber pressure P_{cc} at z = 0, hermetic conditions (no pressure gradient) at the evaporator case wall, $r = \xi$, symmetry condition at r = 0. Two different boundary conditions for the solid cylinder are observed, $z = \beta$: for $0 < r < \omega$, $\partial P/\partial z = 0$ and, for $\omega < r < \xi$, a pressure gradient condition, obtained from the Darcy´s equation, where the liquid velocity is given by equation (4.4), is applied.

The hydraulic problem for the solid cylinder region is expressed as

$$\frac{\partial^2 P}{\partial r^2} + \frac{1}{r}\frac{\partial P}{\partial r} + \frac{\partial^2 P}{\partial z^2} = 0 \quad in \ 0 < r < \xi, 0 < z < \beta \qquad (4.115)$$

which is subjected to the following boundary conditions:

$$\frac{\partial P(0,z)}{\partial r} = 0 \ a \qquad (4.116)$$

$$\frac{\partial P(\xi,z)}{\partial r} = 0 \qquad (4.117)$$

$$P(r,0) = P_{cc} \qquad (4.118)$$

$$\frac{\partial P}{\partial z} = 0 \ \text{for} \ 0 < r < \omega \ \ and \ \ \frac{\partial P}{\partial z} = -\frac{\mu_l u}{k}\text{for} \ \omega < r < \xi \quad (4.119)$$
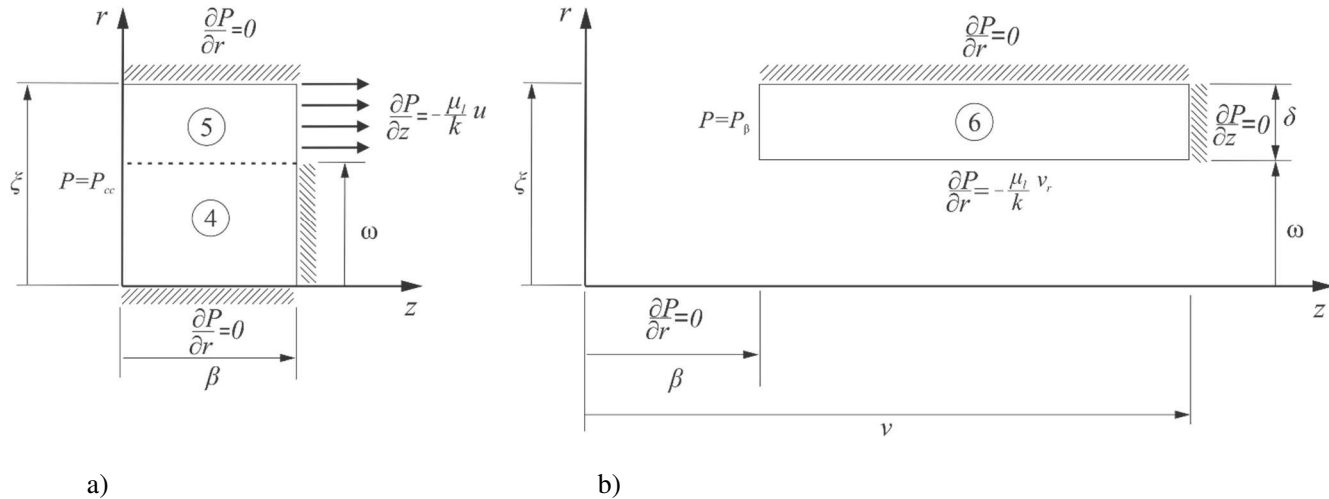
Figure 45 - Decomposition process of the hydraulic problem into two cylindrical geometries. a) Porous media plug, b) Evaporation section.

As already mentioned, the solid cylinder is divided into two regions, so that only one uniform boundary conditions is applied. However, even with this strategy, problems 4 and 5 still have two non-homogeneous boundary conditions, at $z = 0$ and at $z = \beta$. To reduce one of these non-homogeneities and so to be able to solve this problem using the separation of variable's method, the parameter Φ, which means the pressure difference relative to the compensation chamber pressure, is introduced:

$$\Phi = P - P_{cc} \qquad (4.120)$$
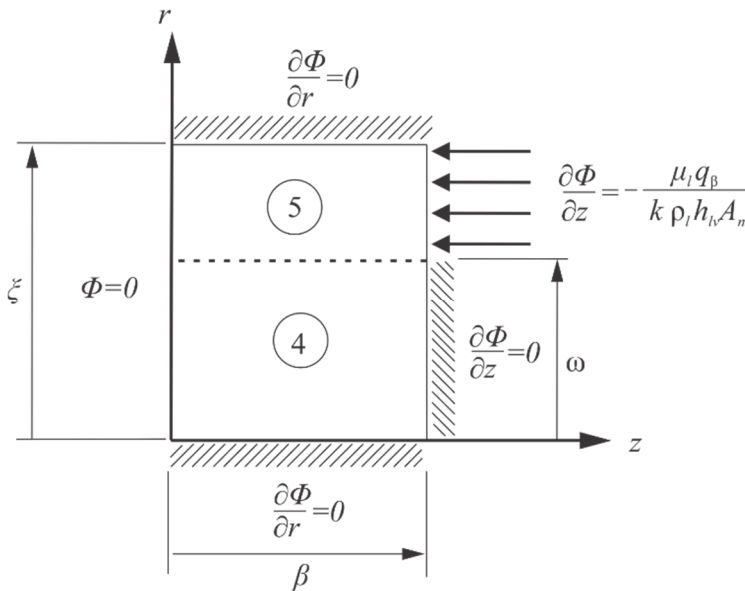
Figure 46 - Schematic of the hydraulic problem divided for subdomains 4 and 5 in terms of the new variable Φ.

Therefore, the problem given by Equations (4.115) to (4.126), in terms of the variable Φ as present in Figure 46 is formulated as:

$$\frac{\partial^2 \Phi}{\partial r^2} + \frac{1}{r}\frac{\partial \Phi}{\partial r} + \frac{\partial^2 \Phi}{\partial z^2} = 0 \quad in \; 0 < r < \beta, 0 < z < \xi \qquad (4.121)$$

subjected to the boundary conditions

$$\frac{\partial \Phi(0,z)}{\partial r} = 0 \tag{4.122}$$

$$\frac{\partial \Phi(\xi,z)}{\partial r} = 0 \tag{4.123}$$

$$\Phi(r,z) = 0 \tag{4.124}$$

$$\frac{\partial \Phi}{\partial z} = 0 \text{ at } 0 < r < w \text{ and } \frac{\partial \Phi}{\partial z} = \frac{\mu_l q_\beta}{k \rho_l A_n h_{lv}} \text{at } w < r < \xi \tag{4.125}$$

The non-homogeneous boundary condition given by Equation (4.125) is obtained using Equation (4.119), where the velocity is $u = \dot{m}/\rho_l A_n$ in which $\dot{m} = q_\beta/h_{lv}$ and q_β is the heat flux that cross the boundary in $z=\beta$.
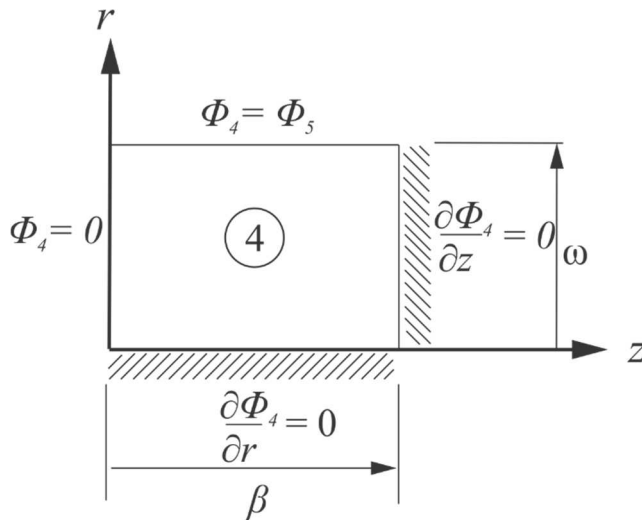
Figure 47 - Sketch of the evaporator hydraulic model for subdomain 4.

Figure 47 presents the subdomain 4 in details. The mathematical formulation of this problem is:

$$\frac{\partial^2 \Phi_4}{\partial r^2} + \frac{1}{r}\frac{\partial \Phi_4}{\partial r} + \frac{\partial^2 \Phi_4}{\partial z^2} = 0 \text{ in } 0 < r < \xi, 0 < z < \beta \tag{4.126}$$

which is subject to the following boundary conditions:

$$\frac{\partial \Phi_4}{\partial r} = 0 \; at \; r = 0, \tag{4.127}$$

$$\Phi_4(\omega, y) = \theta_{5a}(\omega, y) \tag{4.128}$$

$$\Phi_4(0, y) = 0 \tag{4.129}$$

$$\frac{\partial \Phi_4(\beta, y)}{\partial z} = 0 \tag{4.130}$$

The general solution for this problem is:

$$Z = A\cos(\tau_m z) + B\sin(\tau_m z) \tag{4.131}$$

$$R = CI_0(\tau_m r) + DK_0(\tau_m r) \tag{4.132}$$

Combining the equations, it yields:

$$\Phi_4(r, z) = \sum_{m=1}^{\infty} R_m I_0(\tau_m r)\sin(\tau_m z) \tag{4.133}$$

where

$$\tau_m = \frac{(2n-1)}{2}\frac{\pi}{\beta} \tag{4.134}$$
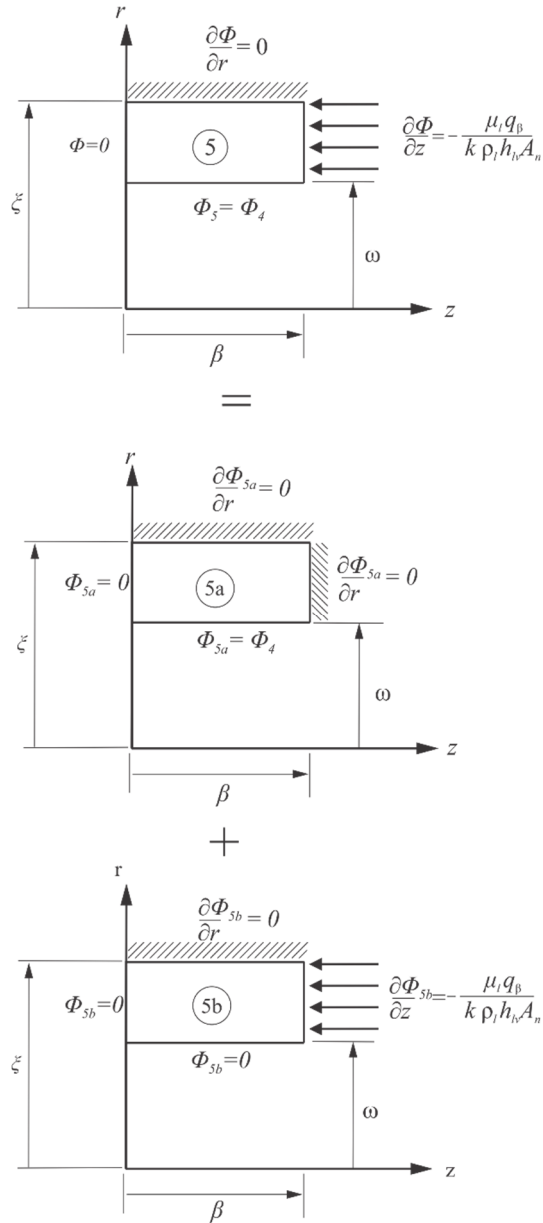
Figure 48 - Schematics of the hydraulic problem 5 divided into subdomains5a and 5b.

On the other hand, problem 5 presents two non-homogeneous boundary conditions, as one can see in Figure 48. Therefore, in order to solve this problem using the separation of variables method, the problem is divided into two other problems, named 5a and 5b, with just one non-homogeneous boundary condition each.

Figure 48 presents the subdomain 5a. The mathematical formulation of this mass problem is

$$\frac{\partial^2 \Phi_{5a}}{\partial r^2} + \frac{1}{r}\frac{\partial \Phi_{5a}}{\partial r} + \frac{\partial^2 \Phi_{5a}}{\partial z^2} = 0 \quad in \ \omega < r < \xi, 0 < z < \beta \quad (4.135)$$

$$\frac{\partial \Phi_{5a}(\xi, z)}{\partial r} = 0 \qquad\qquad (4.136)$$

$$\Phi_{5a}(\omega, z) = \Phi_4(\omega, z) \qquad\qquad (4.137)$$

$$\Phi_{5a}(r, z) = 0 \qquad\qquad (4.138)$$

$$\frac{\partial \Phi_{5a}(r, \beta)}{\partial z} = 0 \qquad\qquad (4.139)$$

whose general solution gives:

$$Z = A cos(\gamma_m z) + B sin(\gamma_m z), \qquad\qquad (4.140)$$

$$R = C I_0(\gamma_m r) + D K_0(\gamma_m r), \qquad\qquad (4.141)$$

Applying the boundary conditions and combining the solutions one gets:

$$\Phi(r, z)_{5a} = \sum_{m=1}^{\infty} S_m \left[\frac{K_1(\gamma_m \xi)}{I_1(\gamma_m \xi)} I_0(\gamma_m r) \right.$$
$$\left. - K_0(\gamma_m r) \right] sin(\gamma_m z) \qquad\qquad (4.142)$$

where

$$\gamma_m = \frac{(2m - 1)}{2}\frac{\pi}{\beta} \qquad\qquad (4.143)$$

In Figure 48, the subdomain 5b and its boundary conditions are presented. The mathematical formulation of this problem is:

$$\frac{\partial^2 \Phi_{5b}}{\partial r^2} + \frac{1}{r}\frac{\partial \Phi_{5b}}{\partial r} + \frac{\partial^2 \Phi_{5b}}{\partial z^2} = 0 \quad in \; \omega < r < \xi, 0 < z < \beta \quad (4.144)$$

$$\frac{\partial \Phi_{5b}(\xi, z)}{\partial r} = 0 \tag{4.145}$$

$$\Phi_{5b}(\omega, z) = 0 \tag{4.146}$$

$$\Phi_{5b}(r, 0) = 0 \tag{4.147}$$

$$\frac{\partial \Phi_{5b}(r, \beta)}{\partial z} = \frac{q''_\beta}{k_{eff}} \tag{4.148}$$

The general solution for this problem is:

$$Z = A cos(\varphi_m z) + B sin(\varphi_m z) \tag{4.149}$$

$$R = C J_0(\varphi_m r) + D Y_0(\varphi_m r) \tag{4.150}$$

Substituting the boundary condition into the last two equations, yields:

$$\frac{Y_0(\varphi_m \omega)}{J_0(\varphi_m \omega)} = \frac{Y_1(\varphi_m \xi)}{J_1(\varphi_m \xi)} \tag{4.151}$$

which is a transcendental equation, where the η_m values correspond to the eigenfunctions.

$$\Phi(r, z)_{5b} = \sum_{n=1}^{\infty} U_m \left[-\frac{Y_0(\varphi_m \omega)}{J_0(\varphi_m \omega)} J_0(\varphi_m r) + Y_0(\varphi_m r) \right] sinh(\varphi_m r) \tag{4.152}$$

where

U_m

$$= \frac{\frac{q_\beta''}{k_{eff}}}{\varphi_m \cosh(\varphi_m \beta)} \frac{\int_\omega^\xi \left[-\frac{Y_0(\varphi_m \omega)}{J_0(\varphi_m \omega)} J_0(\varphi_m r) + Y_0(\varphi_m r)\right] r \, dr}{\int_\omega^\xi \left[-\frac{Y_0(\varphi_m \omega)}{J_0(\varphi_m \omega)} J_0(\varphi_m r) + Y_0(\varphi_m r)\right]^2 r \, dr} \quad (4.153)$$

The Fourier series coefficients are obtained considering the interface pressure equilibrium, for be applied in the interface $r = w$, $0 < z < \beta$, or:

$$\Phi(r,z)_{5a} = \Phi(r,z)_4 \quad (4.154)$$

Substituting the solution of the subdomain 5a and 4 in Equation (4.161) one gets:

$$\sum_{m=1}^{\infty} R_m I_0(\tau_m r) \sin(\tau_m z)$$
$$= \sum_{n=1}^{\infty} S_m \left[\frac{K_1(\gamma_m \xi)}{I_1(\gamma_m \xi)} I_0(\gamma_m r)\right. \quad (4.155)$$
$$\left. - K_0(\gamma_m r)\right] \sin(\gamma_m z)$$

The coefficient S_m can be solved applying the orthogonally principle, resulting in the equation:

$$S_m = \frac{I_0(\tau_m r)}{\left[\frac{K_1(\gamma_m \xi)}{I_1(\gamma_m \xi)} I_0(\gamma_m r) - K_0(\gamma_m r)\right]} R_m \quad (4.156)$$

To determine other parameter R_m, the following condition still needs to be applied in the interface $r = w$, $0 < z < \beta$:

$$\frac{\partial \Phi_4(r,z)}{\partial r} = \frac{\partial \Phi_5(r,z)}{\partial r} \quad (4.157)$$

which can be written as:

$$\frac{\partial \Phi_{4a}(r,z)}{\partial r} = \frac{\partial \Phi_{5a}(r,z)}{\partial r} + \frac{\partial \Phi_{5b}(r,z)}{\partial r} \quad (4.158)$$

Again, substituting subdomains 5 and 4 solutions in the Equation (4.165), one obtain:

$$\sum_{m=1}^{\infty} R_m \lambda_m I_1(\tau_m \omega) \sin(\tau_m z)$$

$$= \sum_{m=1}^{\infty} S_m \left[\frac{K_1(\gamma_m \xi)}{I_1(\gamma_m \xi)} I_1(\gamma_m \omega) \right.$$

$$- K_1(\gamma_m \omega) \right] \sin(\gamma_m z) \qquad (4.159)$$

$$+ \sum_{m=1}^{\infty} U_m \left[\frac{Y_0(\varphi_m \omega)}{J_0(\varphi_m \omega)} J_1(\varphi_m \omega) \right.$$

$$- Y_1(\varphi_m \omega) \right] \sinh(\varphi_m z)$$

The Equation (4.159) can be arranged as an expanded Fourier series of a function $f(z)$:

$$\underbrace{\sum_{\widehat{m}=1}^{\infty} U_m \left[\frac{Y_0(\varphi_{\widehat{m}} \omega)}{J_0(\varphi_{\widehat{m}} \omega)} J_1(\varphi_{\widehat{m}} \omega) - Y_1(\varphi_{\widehat{m}} \omega) \right] \sinh(\varphi_{\widehat{m}} z)}_{f(z)} =$$

$$\sum_{m=1}^{\infty} \hat{R}_m \sin(\tau_m z), \qquad (4.160)$$

Applying, the orthogonally properties, the R_m coefficients of the Fourier series can be determined by:

$$\hat{R}_m = \frac{\sum_{\widehat{m}=1}^{\infty} U_{\widehat{m}} \left[\frac{Y_0(\varphi_{\widehat{m}} \omega)}{J_0(\varphi_{\widehat{m}} \omega)} J_1(\varphi_{\widehat{m}} \omega) - Y_1(\varphi_{\widehat{m}} \omega) \right] \int_0^{\omega} \sinh(\varphi_{\widehat{m}} z) \sin(\tau_m z) dz}{\int_0^{\omega} \sin^2(\tau_m z) dz}, \qquad (4.161)$$

where

$$\hat{R}_m = \left\{ \lambda_m I_1(\tau_m \omega) - \frac{I_0(\tau_m r) \left[\frac{K_1(\gamma_m \xi)}{I_1(\gamma_m \xi)} I_1(\gamma_m \omega) - K_1(\gamma_m \omega) \right]}{\left[\frac{K_1(\gamma_m \xi)}{I_1(\gamma_m \xi)} I_0(\gamma_m r) - K_0(\gamma_m r) \right]} \right\} R_m, \qquad (4.162)$$

Substituting equation (4.162) into equation (4.161) one finds:

$$R_m = \frac{\sum_{\widehat{m}=1}^{\infty} U_{\widehat{m}} \left[\frac{Y_0(\varphi_{\widehat{m}}\omega)}{J_0(\varphi_{\widehat{m}}\omega)} J_1(\varphi_{\widehat{m}}\omega) - Y_1(\varphi_{\widehat{m}}\omega)\right] \int_0^\omega \sinh(\varphi_{\widehat{m}}z)\sin(\tau_m z)dz}{\left\{\lambda_m I_1(\tau_m\omega) - \frac{I_0(\tau_m r)\left[\frac{K_1(\gamma_m\xi)}{I_1(\gamma_m\xi)}I_1(\gamma_m\omega) - K_1(\gamma_m\omega)\right]}{\left[\frac{K_1(\gamma_m\xi)}{I_1(\gamma_m\xi)}I_0(\gamma_m r) - K_0(\gamma_m r)\right]}\right\} \int_0^\omega \sin^2(\tau_m z)dz}, \quad (4.163)$$

4.2.2.2 Hydraulic pressure distribution for hollow wick structure

Figure 49 shows the hydraulic model for the hollow cylinder.
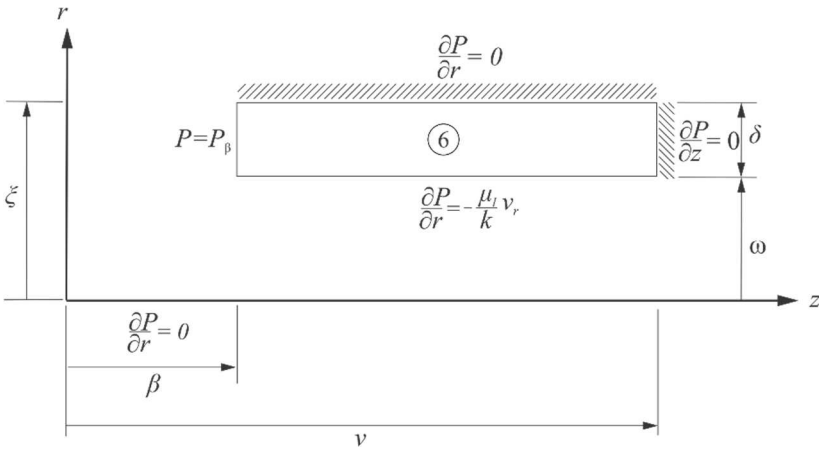
Figure 49 - Schematic of the hydraulic problem in the domain 6.

The mathematical formulation of problem 6 is

$$\frac{\partial^2 P}{\partial r^2} + \frac{1}{r}\frac{\partial P}{\partial r} + \frac{\partial^2 P}{\partial z^2} = 0 \quad in \quad \omega < r < \xi, \beta < z < \upsilon, \qquad (4.164)$$

and the following boundary conditions:

$$\frac{\partial P(\omega, z)}{\partial r} = -\frac{\mu_l}{k}u \qquad (4.165)$$

$$\frac{\partial P(\xi, z)}{\partial r} = 0 \; at \; r = \xi \qquad (4.166)$$

$$P(r, \beta) = P_\beta \qquad (4.167)$$

$$\frac{\partial P}{\partial z} = 0 \ at \ z = v \tag{4.168}$$

To homogenize boundary conditions and simplify the problem under study, the parameter Φ, which is the pressure difference relative to the compensation chamber pressure is adopted (see Figure 50), where:

$$\Psi = P - P_\beta, \tag{4.169}$$
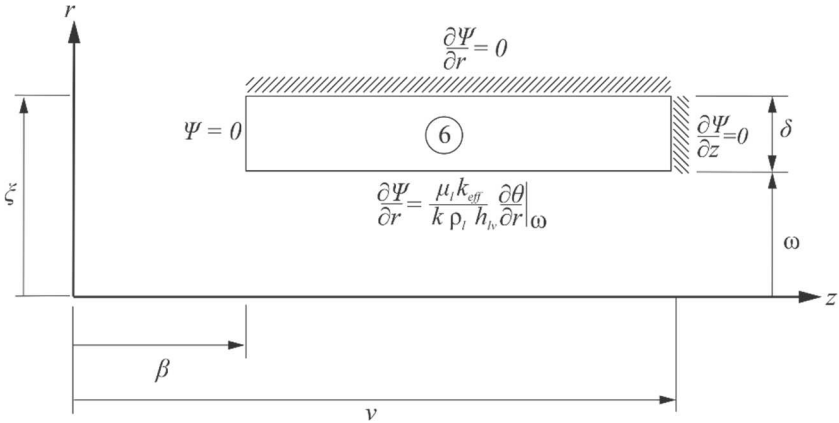
Figure 50 - Schematics of the hydraulic problem in the domain 6 in function of the new variable Ψ.

Therefore, the Laplace Equation takes the form:

$$\frac{\partial^2 \Psi_6}{\partial r^2} + \frac{1}{r}\frac{\partial \Psi_6}{\partial r} + \frac{\partial^2 \Psi_6}{\partial z^2} = 0 \quad in \, \omega < r < \xi, 0 < z < \beta \tag{4.170}$$

$$\frac{\partial \Psi_6(\omega, z)}{\partial r} = \Gamma \frac{\partial T}{\partial r} \tag{4.171}$$

$$\frac{\partial \Psi_6(\xi, z)}{\partial r} = 0 \tag{4.172}$$

$$\Psi_6(r, \beta) = 0 \tag{4.173}$$

$$\Psi_6(r, v) = 0 \tag{4.174}$$

where:

$$\Gamma = -\frac{\mu_l k_{eff}}{k \rho_l h_{lv}} \tag{4.175}$$

The boundary condition represented by Equation (4.171) is obtained substituting the velocity as $v = \dot{m}/\rho_l A_n$ and $\dot{m} = q_\omega/h_{lv}$ in the original boundary condition given by Equation (4.165), where $\dot{m}$ is the mass flow ratio, ρ is the density of liquid, q_ω is the heat flow that cross the boundary at $r = \omega$. q_ω can be calculated by the temperature gradient in $r = \omega$, obtained from solution of the temperature field. This boundary condition allows the coupling between pressure and temperature fields (DEMIDOV; YATSENKO, 1994; FAGHRI, 1995; SANTOS, 2010).

The general solution for the mathematical problem presented in Figure 50 is:

$$Z = A\cos(\epsilon_n z) + B\sin(\epsilon_n z) \tag{4.176}$$

$$R = CI_0(\epsilon_n r) + DK_0(\epsilon_n r), \tag{4.177}$$

where:

$$\epsilon_n = \frac{(2n-1)\,\pi}{2}\frac{1}{l} \tag{4.178}$$

and:

$$\Psi(r,z)_6 = \sum_{n=1}^{\infty} W_n \left[\frac{K_1(\epsilon_n \xi)}{I_1(\epsilon_n \xi)} I_0(\epsilon_n r) + K_0(\epsilon_n r) \right] \sin(\epsilon_n z) \tag{4.179}$$

with:

$$W_n = \frac{\Gamma}{\epsilon_n \left[\frac{K_1(\epsilon_n \xi)}{I_1(\epsilon_n \xi)} I_1(\epsilon_n \omega) - K_1(\epsilon_n \omega)\right]} \frac{\int_0^l \left(\frac{\partial \theta}{\partial r}\Big|_\omega\right) \sin(\epsilon_n z)\,dz}{\int_0^l \sin^2(\epsilon_n z)\,dz} \tag{4.180}$$

4.2.3 Summary and application of the thermal model equations

In this section, the temperature field and heat ratio for a wick structure geometry are presented. In Table 9, design LHP geometry parameters and thermophysical properties used to apply the thermal model are shown.

In Table 10 and Table 11, thermal solution equations for the solid and hollow cylinder that compose the wick structure evaporator are

presented. The analytical solution for these equations was implemented in Maple software. The series convergence criteria are achieved when the difference between the heat ratio inlet and output for each domain is less than 0.01 W. Generally, the convergence criterion for Fourier series solution was obtained for 150 terms.

Table 9. Designed LHP geometry parameters and thermophysical properties.

Designed LHP	
Wick geometrical parameter	
Wick Length l	30.22 mm
Wick thickness δ	2.2 mm
Wick Isolated length φ	0.11mm
Wick external radius ξ	5.6 mm
Wick internal radius ω	3.4 mm
Wick bottom length β	7.89 mm
Wick thermophysical properties	
Wick effective thermal conductivity	42.86±0.31 W/m·K
Wick permeability	1.99E-12 m^2
Effective porous radius	24.1 µm
Porosity	53.46±3.87
Loop geometrical parameter	
Evaporator diameter	12.70 mm
Working fluid	Water
Case material	Copper
Fluid charge	2.4 ml
Condenser serpentine and liquid and vapor tube diameter	1.62 mm
Length of tube vapor line	81.6 mm
Length of tube liquid line	252.4 mm
Condenser length	154.0 mm
Heat sink temperature	20 °C

Table 10. Thermal solution equations for wick structure evaporator.

Solid cylinder

$$\theta(r,z)_1 = \sum_{m=1}^{\infty} L_m I_0(\lambda_m r) \sin(\lambda_m z) \tag{4.181}$$

$$\theta(r,z)_{2a} = \sum_{m=1}^{\infty} M_m \left[\frac{K_1(\zeta_m \xi)}{I_1(\zeta_m \xi)} I_0(\zeta_n r) - K_0(\zeta_n r) \right] \sin(\zeta_m z) \tag{4.182}$$

$$\theta(r,z)_{2b} = \sum_{n=1}^{\infty} N_n \left[-\frac{Y_0(\eta_m \omega)}{J_0(\eta_m \omega)} J_0(\eta_m r) + Y_0(\eta_m r) \right] \sinh(\eta_m r) \tag{4.183}$$

$$N_n = \frac{\frac{q_\beta''}{k_{eff}}}{\eta_m \cosh(\eta_m \beta)} \frac{\int_\omega^\xi \left[-\frac{Y_0(\eta_m \omega)}{J_0(\eta_m \omega)} J_0(\eta_m r) + Y_0(\eta_m r) \right] r\, dr}{\int_\omega^\xi \left[-\frac{Y_0(\eta_m \omega)}{J_0(\eta_m \omega)} J_0(\eta_m r) + Y_0(\eta_m r) \right]^2 r\, dr} \tag{4.184}$$

$$M_n = \frac{I_0(\lambda_m r)}{\left[\frac{K_1(\zeta_m \xi)}{I_1(\zeta_m \xi)} I_0(\zeta_m r) - K_0(\zeta_m r) \right]} L_m \tag{4.185}$$

$$L_m = \frac{\sum_{n=1}^{\infty} N_n \left[\frac{Y_0(\eta_n \omega)}{J_0(\eta_n \omega)} J_1(n\omega) - Y_1(\eta_n \omega) \right] \int_0^\omega \sinh(\eta_n z) \sin(\lambda_m z) dz}{\int_0^\omega \sin^2(\lambda_m z)\, dz} \tag{4.186}$$

Hollow cylinder

$$T(r,z)_{3a} = \sum_{n=1}^{\infty} O_n \left[-\frac{K_0(\vartheta_n \omega)}{I_0(\vartheta_n \omega)} I_0(\vartheta_n r) + K_0(\vartheta_n r) \right] \sin(\vartheta_n z) \tag{4.187}$$

$$O_n = \frac{\frac{q_\beta''}{k_{eff}}}{\vartheta_n \left[-\frac{K_0(\vartheta_n \omega)}{I_0(\vartheta_n \omega)} I_1(\vartheta_n \xi) - K_1(\vartheta_n \xi) \right]} \frac{\int_\varsigma^l \sin(\vartheta_n z) dz}{\int_0^l \sin^2(\vartheta_n z) dz} \tag{4.188}$$

$$T(r,z)_{3b} = \sum_{n=1}^{\infty} P_n \left[\frac{K_1(\chi_n \xi)}{I_1(\chi_n \xi)} I_0(\chi_n r) + K_0(\chi_n r) \right] \sin(\chi_n z) \tag{4.189}$$

$$P_n = \frac{T_v}{\left[\frac{K_1(\chi_n \xi)}{I_1(\chi_n \xi)} I_0(\chi_n \omega) + K_1(\chi_n \omega) \right]} \frac{\int_0^l \sin(\chi_n z)\, dz}{\int_0^l [\sin(\chi_n z)]^2\, dz} \tag{4.190}$$

$$T(r,z)_{3c} = \sum_{n=1}^{\infty} Q_n \left[-\frac{Y_0(Щ_n \xi)}{J_0(Щ_n \xi)} J_0(Щ_n r) + Y_0(Щ_n r) \right] \cosh(Щ_n(z-l)) \tag{4.191}$$

$$Q_n = \frac{T_v}{\cosh(Щ_n l)} \frac{\int_\omega^\xi T(r) \left[\frac{Y_0(Щ_n \xi)}{I_0(Щ_n \xi)} I_0(Щ_n r) + K_1(Щ_n r) \right] r\, dr}{\int_\omega^\xi \left[-\frac{Y_0(\chi_n \xi)}{J_0(\chi_n \xi)} J_0(Щ_n r) + K_1(Щ_n r) \right]^2 dz}, \tag{4.192}$$

Table 11. Thermal solution equations for wick structure evaporator.

Heat leak

$$q = q_1 + q_2, \tag{4.193}$$

$$q_1 = 2\pi k_{eff} \sum_{m=1}^{\infty} \lambda_m L_m cos(\lambda_m z_i) \int_0^{\omega} I_0(\lambda_m r) r dr, \tag{4.194}$$

$$q_2 = q_{2a} + q_{2b}, \tag{4.195}$$

$$q_{2a} = 2\pi k_{eff} \sum_{m=1}^{\infty} \zeta_m M_m cos(\zeta_m z_i) \int_{\omega}^{\xi} \left[\frac{K_1(\zeta_m \xi)}{I_1(\zeta_m \xi)} I_0(\zeta_m r) + K_0(\zeta_m r) \right] I_0(\zeta_m r) r dr, \tag{4.196}$$

$$q_{2b} = 2\pi k_{eff} \sum_{m=1}^{\infty} \eta_m N_m cosh(\eta_m z_i) \int_{\omega}^{\xi} \left[-\frac{Y_0(\eta_m \xi)}{J_0(\eta_m \xi)} J_0(\eta_m r) + Y_0(\eta_m r) \right] r dr, \tag{4.197}$$

Heat transfer to active zone

$$q_{\omega} = \int_{\beta}^{\upsilon} k_{eff} 2\pi r \frac{\partial \theta_{3a}}{\partial r} \bigg|_{\omega} dz$$
$$+ \int_{\beta}^{\upsilon} k_{eff} 2\pi r \frac{\partial \theta_{3b}}{\partial r} \bigg|_{\omega} dz \tag{4.198}$$
$$+ \int_{\beta}^{\upsilon} k_{eff} 2\pi r \frac{\partial \theta_{3c}}{\partial r} \bigg|_{\omega} dz$$

$$q_{3a} = 2\pi \omega k_{eff} \sum_{n=1}^{\infty} \vartheta_n O_m \left[-\frac{K_0(\vartheta_n \omega)}{I_0(\vartheta_n \omega)} I_1(\vartheta_n \omega) - K_0(\vartheta_n \omega) \right] \int_0^l \sin(\vartheta_n z) dz \tag{4.199}$$

$$q_{3b} = 2\pi \omega k_{eff} \sum_{n=1}^{\infty} \chi_n P_n \left[\frac{K_1(\chi_n \xi)}{I_1(\chi_n \xi)} I_1(\chi_n \omega) - K_1(\chi_n \omega) \right] \int_0^l \sin(\chi_n z) dz \tag{4.200}$$

$$q_{3c} = 2\pi\omega k_{eff} \sum_{n=1}^{\infty} Щ_n Q_n \left[\frac{Y_0(Щ_n\xi)}{J_0(Щ_n\xi)} J_1(Щ_n\omega) - Y_1(Щ_n\omega)\right] \int_0^l \cosh(Щ_n z) dz$$

(4.201)

In order to solve the equations system, a heat ratio q_β at the interface at z=β and $w < r < \xi$ (subdomain 2 e 3, see Figure 45) is chosen, for which results a temperature distribution $T_\beta(r)$. This solid cylinder temperature distribution $T_\beta(r)$ is used as the prescribed temperature distribution boundary condition for the hollow cylinder (domain 3) and a new heat transfer ratio q_β in the interface at z = β and $w < r < \xi$ is calculated. If the difference between the heat transfer ratio for domains 2 and 3, and the q_β considered in the interface at z = β and $w < r < \xi$ is less than 0.01 W, the convergence is achieved. Otherwise, a new heat ratio q_β is chosen and the procedure is repeated. In Figure 51 and Figure 52, the temperature distributions of the wick structure, which geometry is described in Table 9, are shown. With this temperature distribution, together with the pressure field (to be presented in the following section), one is able to make a thermodynamic analysis of the evaporator wick structure operation.

In Figure 51, one can see that temperature distribution in the solid cylinder presents a close to unidimensional behavior in the r direction. However, in the region close to the coupling with the solid cylinder, the isothermal lines show a bidimensional behavior, evidencing a heat leak to the compensation chamber. One can also see that the temperature distribution due to the boundary conditions in the vapor region are coherent with the physical model (hypothesis) with exception to the left lower region, due to the coupling of two different boundary conditions (insulation in the solid cylinder and prescribed temperature in the hollow cylinder).
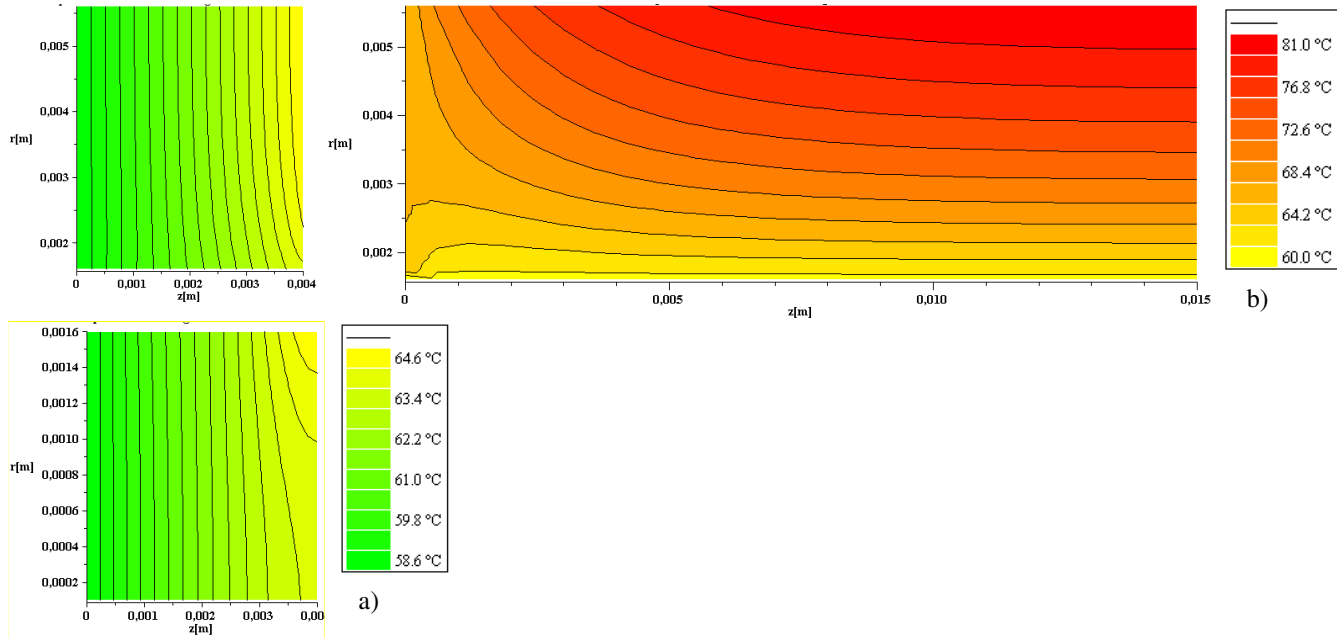
Figure 51 - Contours of temperature field of LHP described in Table 9. (a) Domains 1 and 2, (b) Domain 3
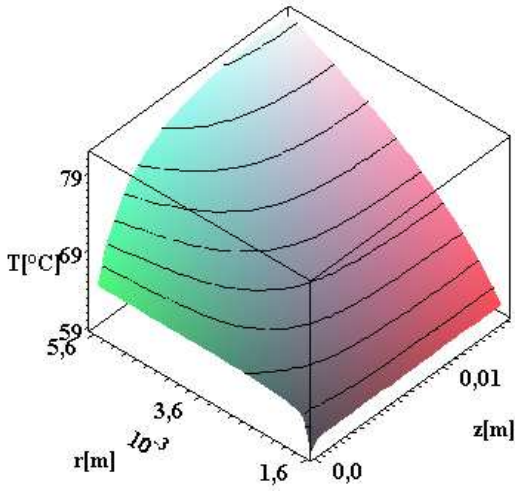
a)
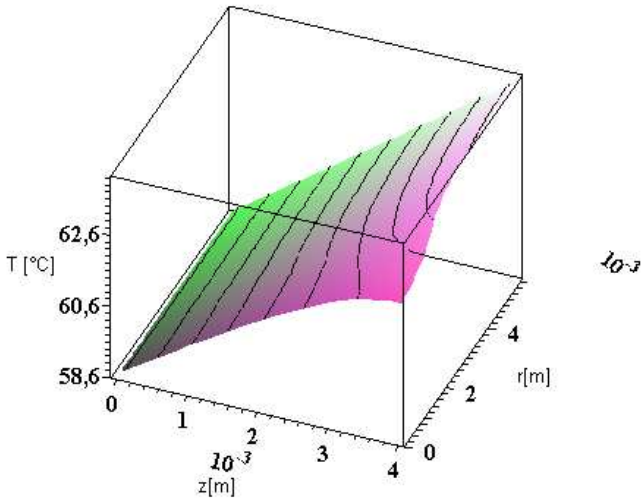
b)

Figure 52 - Surfaces of temperature field of LHP described in Table 9, (a) Domains 1 and 2, (b) Domain 3.

In Figure 52a, at point (β,ω) can be observed that the coupling solution do not satisfy the original boundary condition (prescribed temperature), this behavior can be due to boundary condition of uniform flux in $z = \beta$ in the subdomain 2.

4.2.4 Summary and application of the pressure model equations

In Table 12, the pressure solution equations for both the solid and the hollow cylinder that compose the wick structure evaporator are presented. Similarly, the numerical solution for these equations are obtained using the Maple software. Unlike the thermal solution, the pressure field for each domain is solved separately. The convergence for Fourier series solution was also obtained with 150 terms. In Figure 53 and Figure 54, the field and gradient of pressure to geometry study are shown for all domains. The pressure drop in domain 3 presents the highest pressure drop for this configuration. The pressure drop in the domain 4-5 represents approximately the 30 % of the total pressure drop in the wick. The pressure field coupled to temperature field allows to evaluate the performance of the wick geometry proposed applied in the LHP evaporator. This model will be used in the chapter 5 in order to analysis the thermal and hydraulic performance of the wick structure.

Table 12 Equations summary for solution of pressure field

Solid cylinder

$$\Phi_4(r,z) = \sum_{m=1}^{\infty} R_m I_0(\tau_m r)\sin(\tau_m z) \tag{4.202}$$

$$R_m = \frac{\sum_{\widehat{m}=1}^{\infty} U_{\widehat{m}}\left[\frac{Y_0(\varphi_m \omega)}{J_0(\varphi_{\widehat{m}}\omega)}J_1(\varphi_{\widehat{m}}\omega)-Y_1(\varphi_{\widehat{m}}\omega)\right]\int_0^{\omega}\sinh(\varphi_{\widehat{m}}z)\sin(\tau_m z)dz}{\left\{\lambda_m I_1(\tau_m \omega)-\frac{I_0(\tau_m r)\left[\frac{K_1(\gamma_m \xi)}{I_1(\gamma_m \xi)}I_1(\gamma_m \omega)-K_1(\gamma_m \omega)\right]}{\left[\frac{K_1(\gamma_m \xi)}{I_1(\gamma_m \xi)}I_0(\gamma_m r)-K_0(\gamma_m r)\right]}\right\}\int_0^{\omega}\sin^2(\tau_m z)dz}, \tag{4.203}$$

$$\Phi(r,z)_{5a} = \sum_{m=1}^{\infty} S_m\left[\frac{K_1(\gamma_m \xi)}{I_1(\gamma_m \xi)}I_0(\gamma_m r)\right.$$
$$\left. - K_0(\gamma_m r)\right]\sin(\gamma_m z) \tag{4.204}$$

$$S_m = \frac{I_0(\tau_m r)}{\left[\frac{K_1(\gamma_m \xi)}{I_1(\gamma_m \xi)}I_0(\gamma_m r)-K_0(\gamma_m r)\right]}R_m \tag{4.205}$$

$$\Phi(r,z)_{5b} = \sum_{n=1}^{\infty} U_m \left[-\frac{Y_0(\varphi_m\omega)}{J_0(\varphi_m\omega)} J_0(\varphi_m r) \right.$$
$$\left. + Y_0(\varphi_m r) \right] \sinh(\varphi_m r) \tag{4.206}$$

$$U_m = \frac{\frac{q''_\beta}{k_{eff}}}{\varphi_m \cosh(\varphi_m \beta)} \frac{\int_\omega^\xi \left[-\frac{Y_0(\varphi_m\omega)}{J_0(\varphi_m\omega)} J_0(\varphi_m r) + Y_0(\varphi_m r) \right] r\, dr}{\int_\omega^\xi \left[-\frac{Y_0(\varphi_m\omega)}{J_0(\varphi_m\omega)} J_0(\varphi_m r) + Y_0(\varphi_m r) \right]^2 r\, dr} \tag{4.207}$$

Hollow cylinder

$$\Psi(r,z)_6 = \sum_{n=1}^{\infty} W_n \left[\frac{K_1(\epsilon_n\xi)}{I_1(\epsilon_n\xi)} I_0(\epsilon_n r) + K_0(\epsilon_n r) \right] \sin(\epsilon_n z), \tag{4.208}$$

$$W_n = \frac{\Gamma}{\epsilon_n \left[\frac{K_1(\epsilon_n\xi)}{I_1(\epsilon_n\xi)} I_1(\epsilon_n\omega) - K_1(\epsilon_n\omega) \right]} \frac{\int_0^l \left(\frac{\partial\theta}{\partial r} \Big|_\omega \right) \sin(\epsilon_n z)\, dz}{\int_0^l \sin^2(\epsilon_n z)\, dz}, \tag{4.209}$$
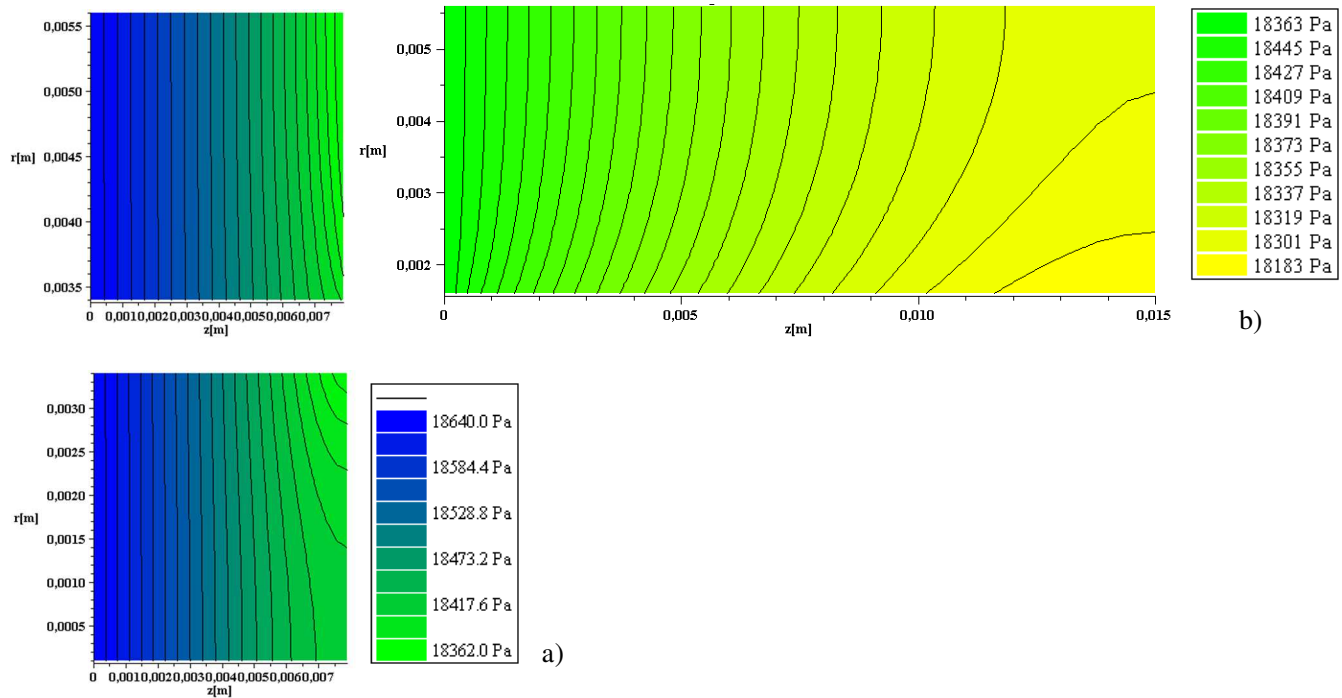
Figure 53 - Contours of pressure field of LHP described in Table 9. (a) Domains 4 and 5, (b) Domain 6.
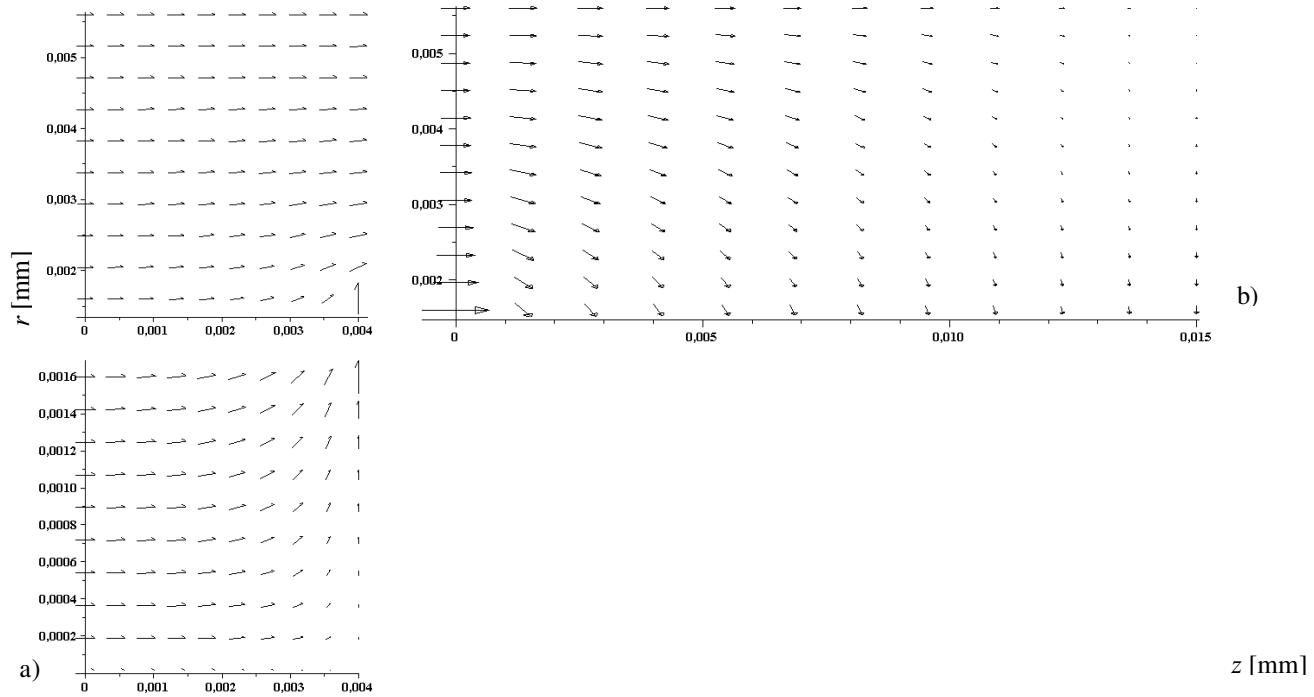
Figure 54 - Pressure gradient of LHP described in Table 20,(a) Domains 4 and 5, (b) Domain 6.

From the temperature and pressure field is possible to determine the thermodynamic state of any point. Using the pressure-temperature curve and applying the thermal equilibrium condition (Equation 2.4) is possible to evaluate if the region of the domain contents vapor. In Figure 55, thermodynamic states for the compensation chamber and the vapor are represented on the curve of saturation on a *P-T* diagram. For any point (*r,z*), its pressure is determined from the pressure field. This pressure represents the local saturation pressure with its corresponding temperature. Sequentially, the temperature for point (*r,z*) is determined from temperature field. Then, the difference of temperature $\Delta T = T(r,z) - T_{sat}$ is determined (where T_{sat} evaluated at pressure $P(r,z)$). This difference of temperature is called as superheating of liquid. If the superheating at any point is higher than the critical superheating, the nucleation boiling can happen and the bubbles are formed inside of wick structure.
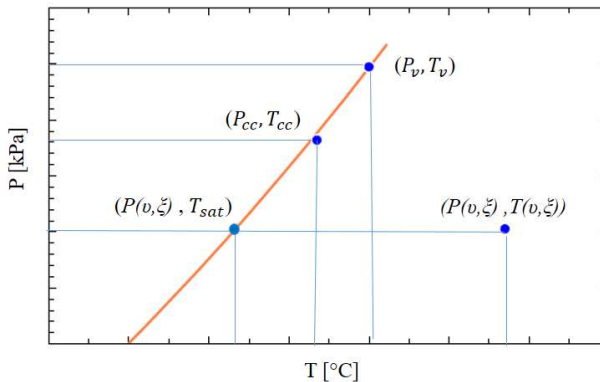
Figure 55 - Analyses of the thermodynamic equilibrium at two states inside of wick evaporator LHP.

The presence of vapor in the wick structure produces an increasing of thermal resistance in the evaporator. When vapor is trapped in the wick structure, it prevents the flow of liquid to the evaporator active zone. In the Figure 51, one can see that the interface between the solid and hollow cylinder is in a critical region for this geometry, where the reduction of transversal area due to vapor formation can increase the pressure drop, reducing the capacity of heat transfer of LHP.

Reay and Kew (2006) present one equation based on the non-homogeneous nucleation theory for commonly wick structures used in the heat pipes HP, expressed as:

$$\Delta T = \frac{3.06\sigma_l T sat}{\rho_v h_{lv} \delta_T} \tag{4.210}$$

where σ_l is the superficial tension, ρ_v is the fluid density, h_{lv} is the heat latent of fluid and δ_T is the thermal boundary layer thickness defined from model of Hsu (1962). This thickness is taken as 25 μm for a typical heat pipe evaporator.

For the geometry analyzed and described in the Table 9, the pressure and temperature on the compensation chamber are 18.6 kPa and 58.7 °C, respectively. For the point (υ,ξ) where the maximum temperature and minimal pressure is achieved by the working fluid, we have that $T(υ,ξ)$=78.02 and $P(υ,ξ)$=18.18 kPa. Here, for a water distillate at a temperature of 58.02 °C, the ΔT_{crit} defined by Equation (4.210) is 9.63°C. On the other hand, the superheating for the point *(υ,ξ)* is 20, thus as $\Delta T > \Delta T_{crit}$, bubbles are formed inside this point. The same evaluation can be made for the geometry and to determine which regions are occupied by bubbles. From this analysis is possible to determine if a geometry proposed for a power load will be affected by the presence partial or total of bubbles that increase the area to mass and heat transfer.

In the chapter 5, same analysis will be applied to the geometry of the wick evaporator studied.

4.3   Loop heat pipe operation model

In the last section, two bi-dimensional mathematical models were proposed to analyze the thermal and hydraulic behavior of the wick structure located within evaporators of LHPs. Obviously, the evaporator is the major component of a LHP and the geometry of the porous media located inside it has major influence in the performance of the device. Therefore, sophisticated detailed models are of prime importance, as the onset of LHP failure (usually by dry-out) commonly starts due to the undesired vapor formation in very specific points or regions of the evaporator.   However, electric analogy steady state simple models may be useful in the determination of LHP operation temperature (usually defined as the compensation chamber temperatures) and of the

maximum the system is able to transfer. Kaya *et al.* (1999) employed thermal circuit analogy models to determine the operation temperature of cylindrical loop heat pipes. Later, Singh *et al.* (2009) also used these models to describe the operation of heat pipe with plane evaporator.
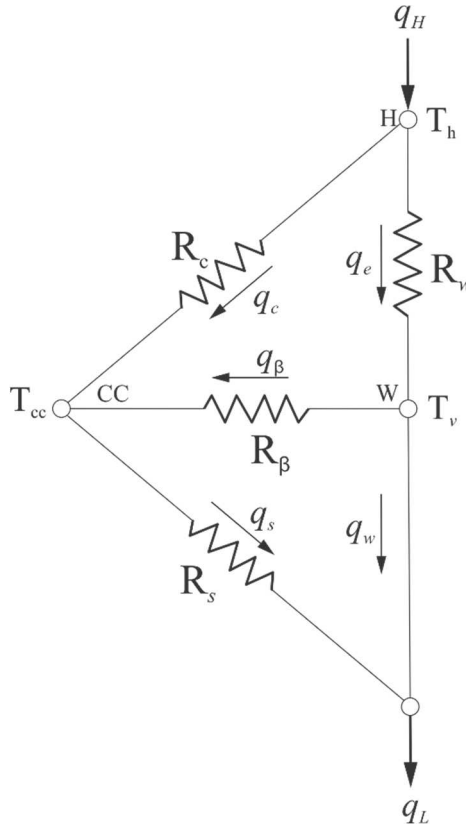
Figure 56 - Sketch of the equivalent thermal circuit of the loop heat pipe.

The sketch of the equivalent thermal circuit of the loop heat pipes proposed in this thesis is present in the Figure 56. In this circuit, the heat q_H, delivered to the evaporator external wall (at temperature T_h) has two different paths to follow. In one path, represented by R_w, heat is delivered to the wick structure and is transferred up to the wick working fluid meniscus, where phase change takes place, at temperature T_v. In the other path, heat is conducted to the compensation chamber through the evaporator casing wall (resistance R_c) at temperature T_{cc}. The heat

transferred in this second path is undesired, and so, considered as a heat loss. However, heat can also be lost to the compensation chamber directly through the wick plug (solid cylinder) through the R_β thermal resistance. Finally, also through the casing and other materials that compose the LHP, heat q_s can be exchanged directly between the compensation chamber and the liquid lines. The vapor and liquid lines are considered adiabatic. The net sensible heat q_L transported by the vapor through the liquid line is eventually removed in the condenser region of the LHP.

Figure 57 shows the evaporator equivalent circuit. The circuit is composed of three thermal resistances: hollow wick radial resistance R_ω, solid wick plug resistance R_β and evaporator case R_c, representing the heat path between the evaporator section and the compensation chamber. In Figure 57, one can be also observe the heat transfer rates at each branch of the circuit. The applied power q_H is delivered to the external wall of the evaporator section: part of the heat is transferred to compensation chamber (heat leak, q_s), through the case wall and wick plug. In order to obtain a good performance from the device, it is expected that this heat leak should be compensated by the working fluid that entering the compensation chamber in subcooled liquid state.
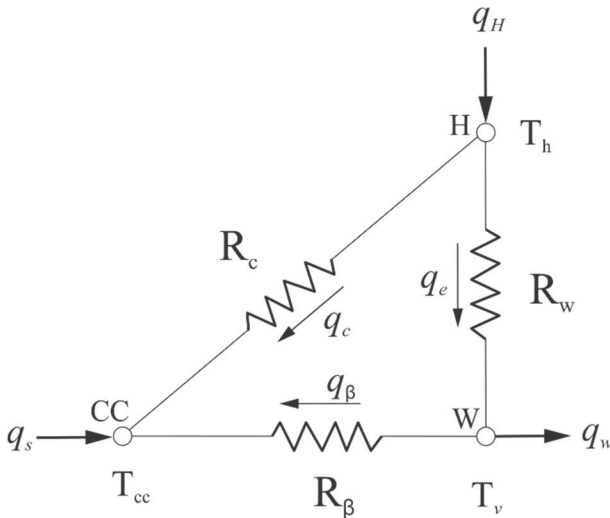
Figure 57 - Sketch of the thermal equivalent circuit of the loop heat pipe evaporator.

An energy balance can be performed at each node of the circuit. For node H one has:

$$q_H = q_c + q_e \tag{4.211}$$

where q_c is the heat transferred through the case and q_e is the heat transferred to evaporation section. Using the thermal resistance analogy equation, this last expression takes the following form, in terms of temperature differences:

$$q_H = \frac{(T_h - T_{cc})}{R_c} + \frac{(T_h - T_v)}{R_\omega} \tag{4.212}$$

where the thermal resistance of evaporation case R_c (unidimensional thermal resistance for a tube) is expressed as

$$R_c = \frac{2\beta + l + l_{cc}}{2\pi[\xi^2 - (\xi+t)^2]k_c}, \tag{4.213}$$

and the thermal resistance of evaporation region (radial thermal resistance for a hollow cylinder) is:

$$R_e = \frac{\ln\left(\frac{\xi}{\omega}\right)}{2\pi l k_{eff}}, \tag{4.214}$$

Likewise, to node W we have:

$$q_e = q_\beta + q_\omega, \tag{4.215}$$

where q_β is the heat transferred from the wick plug to the compensation chamber and q_ω is the net heat used to evaporate the working fluid. Therefore, q_e is given by:

$$q_e = \frac{(T_e - T_{cc})}{R_\beta} + q_\omega \tag{4.216}$$

The thermal resistance of evaporation plug region is expressed as:

$$R_\beta = \frac{\beta}{\pi r_\xi^2 k_{eff}} \tag{4.217}$$

Finally, the energy balance for node CC becomes:

$$q_s = q_c + q_\beta \tag{4.218}$$

where q_s is the sensible heat transferred for subcooling of the liquid that returns from the condenser. The heat q_s is obtained from:

$$q_s = \dot{m}C_p(T_s - T_{cc}) \tag{4.219}$$

where T_s is the compensation chamber returning fluid temperature. This temperature can be obtained by heat transfer analyses in the condenser region. In terms of the thermal resistance, equation (4.216) can be expressed as:

$$q_e = \frac{(T_h - T_{cc})}{R_c} + \frac{(T_e - T_{cc})}{R_\beta}, \tag{4.220}$$

4.4 Liquid and vapor lines pressure drop

The pressure drops, due the friction of vapor and liquid flowing through the lines, are modeled using equations of the form:

$$R_h = f(V, L, D, \mu_\beta) \tag{4.221}$$

Darcy-Weisbach developed the following equation for the calculation of the pressure drop of a fluid flowing in circular tubes in laminar and turbulent regime (CENGEL; BOLES, 2006; FOX; MCDONALD, 2001):

$$\Delta P = f \frac{L}{D} \frac{\rho u^2}{2} \tag{4.222}$$

where f is the Darcy friction factor, which depends on the Reynold number, and D is the internal diameter of pipe while L is the length of the pipe. For smooth channels in laminar regime, the friction factor is expressed as:

$$f = \frac{64}{R_e} \quad R_e < 2300 \tag{4.223}$$

For turbulent regime:

$$f = \frac{0.316}{R_e^{0.25}} \quad R_e > 2300 \tag{4.224}$$

where R_e is the Reynold number based on the diameter.

4.5   Condenser analysis

The condenser is an important component for the performance of LHPs. The condenser should be designed to reject the heat inserted in the LHP in steady state conditions. The condenser pressure drop and the output temperature of the condensate influence the operation temperature of LHP. Therefore, one important parameter is the length of the condenser. This length is used to calculate the pressure drop due to the working fluid phase change and in the transport of subcooled liquid.

In this section, mathematical models are proposed to determine the phase change length in LHP condenser. For modelling purposes, the condenser is considered divided into two regions: the first used to transfer latent heat (and so to cause phase change) and second to transfer sensible heat (and so, to subcool the condensate).

4.5.1 Heat transfer analysis
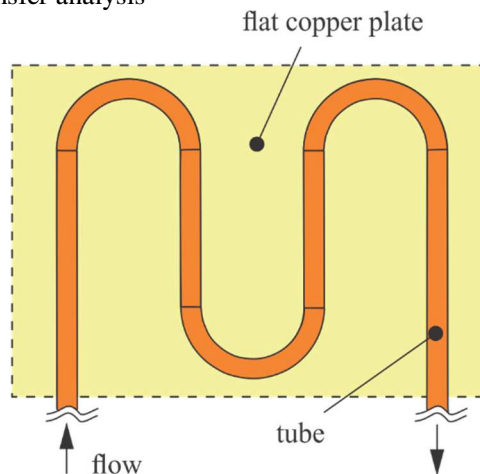
Figure 58 - Schematics of the divisions of the condenser.

The condenser configuration studied in this work consists of a U shaped bent tube, welded on a flat copper plate (see Figure 58), with the working fluid flowing through this tube. The copper plate is attached to an aluminum block. The aluminum block has channels inside, where water flows through it. The temperature of water is controlled by a thermostatic bath. Figure 59 shows a schematic of the tube, the plate cross section and the welding material, which connects them. For modelling purposes, the tube is considered straight, with the external

face subjected to convection heat transferred to the ambient air. A thermal resistance network is constructed to model the heat transfer between the tube and ambient air, as also shown in Figure 59.
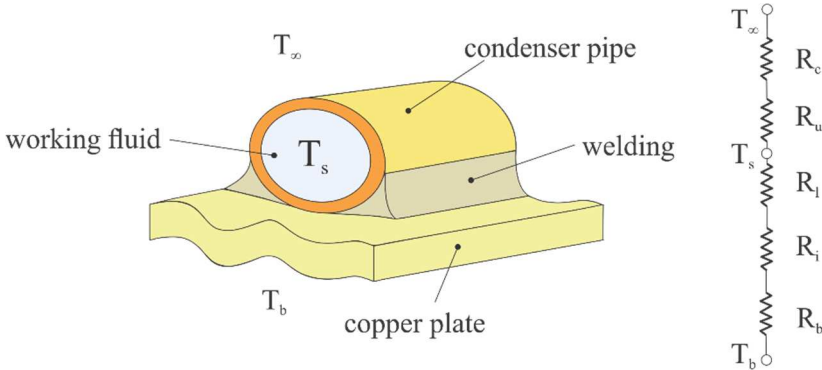
Figure 59 - Condenser latent heat transfer analysis.

To calculate the condenser tube length, where the liquid changes phase, a heat balance over the condenser region is performed:

$$q_{lv} = \bar{h}_D A_i (T_{sat} - T_s) \tag{4.225}$$

where

$$A_i = 2\pi r_i L^{2\phi} \tag{4.226}$$

Where $\bar{h}_D$ is the heat transfer coefficient for phase change in horizontal tube, A_i is the internal area of tube, T_{sat} is the saturation temperature, $L^{2\phi}$ is the length dimension of condenser necessary for the working fluid changes of phase. The heat transfer coefficient is calculated from Chato (1962) as:

$$\bar{h}_D = 0.555 \left[\frac{g\rho_l(\rho_l - \rho_v)k_l^3 h'_{lv}}{\mu_l(T_{sat} - T_s)D_i} \right]^{0.25} \tag{4.227}$$

with

$$h'_{lv} = h_{lv} + \frac{3}{8} C_{p,l}(T_{sat} - T_s) \tag{4.228}$$

where h_{lv} is the vaporization enthalpy, $C_{p,l}$ is the specific heat, g is the gravitational acceleration, ρ_l is the density of fluid in liquid phase, ρv is the density of fluid in vapor phase, k_l is the thermal conductivity of fluid, μ_l is the dynamic viscosity of liquid and D_i is the internal diameter of tube.

From energy conservation balance, the power also can be expressed as:

$$q_{lv} = q_{cond} + q_{conv} \tag{4.229}$$

where q_{lv} is the latent heat, q_{cond} is the heat transferred by conduction through the lower side of the pipe section and q_{conv} is the heat transferred by natural convection in the upper side of section pipe. In terms of thermal resistances, this last equation takes the form:

$$\dot{m}h_{lv} = \frac{(T_e - T_\infty)}{R_{up}} + \frac{(T_e - T_b)}{R_{down}} \tag{4.230}$$

where R_{up} and R_{down} is the equivalent thermal resistance of the upper and lower sides of the tube, respectively. The upper resistance is composed by a conductive and a convection thermal resistance, arrangement in series, or:

$$R_{up} = R_c + R_u \tag{4.231}$$

where

$$R_u = \frac{2\ln(^{r_e}/r_i)}{3\pi k_l L^{2\phi}} \tag{4.232}$$

$$R_c = \frac{1}{\bar{h}A_c} \tag{4.233}$$

With the transversal area defined for case (hollow tube) as

$$A_c = \frac{3\pi}{2} r_e L^{2\phi}, \tag{4.234}$$

where r_e is the external radio of pipe and $L^{2\phi}$ is the length of the condenser necessary for the working fluid changes of phase.

The mean thermal coefficient $\bar{h}$ is obtained from the definition of $N_u = \bar{h}D/k$ where Nu is calculated by the following equation according to Churchill and Chu (1975):

$$N_u = \left\{ 0.60 + \frac{0.387 R_{a_D}^{\;1/6}}{\left[1 + \left(\frac{0.559}{P_r} \right)^{9/16} \right]^{8/27}} \right\}^2 \quad R_{a_D} \leq 10^{12} \qquad (4.235)$$

with

$$R_{a_D} = \frac{g\beta(T_e - T_\infty)D_e^3}{\nu\alpha} \qquad (4.236)$$

where R_{aD} is the Rayleigh number based on external diameter of condenser tube.

On the other hand, the thermal resistance in the down side of the condenser tube is defined as:

$$R_{low} = R_b + R_i + R_l \qquad (4.237)$$

with

$$R_b = \frac{t_b}{2r_i k_{cu} L 2\phi} \qquad (4.238)$$

$$R_i = \frac{2\ln(r_e/r_i)}{\pi k_w L 2\phi} \qquad (4.239)$$

$$R_l = \frac{2\ln(\frac{2r_e + h_w}{2r_i})}{\pi k_w L 2\phi} \qquad (4.240)$$

where R_b, R_l and R_i are the plane, tube wall and welding resistances, respectively.

The output temperature of the condenser is determined from an energy balance in the second region of the tube, where the already condensed working fluid is sub-cooled. The heat balance over the condenser region, where the working fluid is in the liquid phase (see Figure 60), is calculated by:
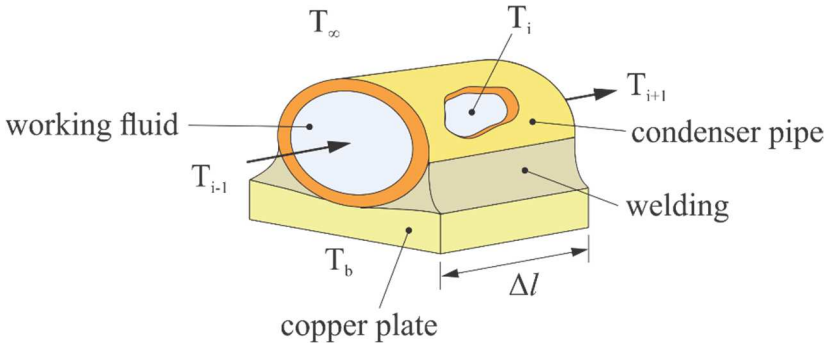
Figure 60 – Condenser sensible heat transfer analysis.

$$q = hA(T_i - T_s) \tag{4.241}$$

Also,

$$\dot{m}C_p(T_i - T_{i+1}) = \frac{(\bar{T} - T_\infty)}{R_{up}} + \frac{(\bar{T} - T_b)}{R_{low}} \tag{4.242}$$

where

$$\bar{T} = \frac{T_i + T_{i+1}}{2} \tag{4.243}$$

4.5.2 Pressure drop

The pressure drop observed in the two-phase flow region represents an important parcel of the total pressure drop observed in the loop heat pipe. After the length of condenser where the liquid changes phase is determined using the thermal model presented in the last section, the pressure drop can be calculated from the literature models. Kandlikar *et al.* (2005) presented several correlations to determine the pressure drop during the condensation. In these works, these authors selected the models of Lockhart and Martinelli (1949), Friedel (1979, 1980) and Chisholm (1973) to calculate de condensation pressure drops, according to the range of validation of each correlation. In order to use these correlations, the following parameters need to be determined.

- Liquid Reynolds number

$$Re_l = \frac{GD(1-x)}{\mu_l} \tag{4.244}$$

- Vapor Reynolds number

$$Re_v = \frac{GDx}{\mu_v} \tag{4.245}$$

- Liquid-only Reynolds number (that is, all fluid flow is in the liquid phase),

$$Re_{lo} = \frac{GD}{\mu_l} \tag{4.246}$$

- Vapor-only Reynold number (that is, all fluid flow is the vapor phase),

$$Re_{vo} = \frac{GD}{\mu_v} \tag{4.247}$$

The single-phase friction factors are calculated using the Churchill and Chu (1975) correlation:

$$f = 8\left[\left(\frac{8}{Re}\right)^{12} + \left\{\left[2.457 \times ln\left(\frac{1}{\left(\frac{7}{Re}\right)^{0.9} + \left(\frac{0.27\varepsilon}{D}\right)}\right)\right]^{16} + \left(\frac{37530}{Re}\right)^{16}\right\}^{-1.5}\right]^{1/12} \tag{4.248}$$

The single-phase pressure gradients are given by:

$$\left(\frac{dP}{dz}\right)_l = \frac{f_l G^2 (1-x)^2}{2D\rho_l} \tag{4.249}$$

$$\left(\frac{dP}{dz}\right)_v = \frac{f_v G^2 x^2}{2D\rho_v} \tag{4.250}$$

$$\left(\frac{dP}{dz}\right)_{lo} = \frac{f_{lo} G^2}{2D\rho_l} \tag{4.251}$$

$$\left(\frac{dP}{dz}\right)_{vo} = \frac{f_{vo} G^2}{2D\rho_v} \tag{4.252}$$

Lockhart and Martinelli (1949) proposed another correlation based on the Martinelli parameter, given by:

$$X = \left[\frac{(dP/dz)_l}{(dP/dz)_v}\right]^{1/2} \tag{4.253}$$

where the two-phase multiplier is given by:

$$\emptyset_l{}^2 = 1 + \frac{C}{X} + \frac{1}{X^2} \tag{4.254}$$

$$C = \begin{cases} Liquid & Vapor \\ 20 \ \text{Turbulent} & \text{Turbulent} \\ 12 \ \text{Laminar} & \text{Turbulent}, \\ 10 \ \text{Turbulent} & \text{Laminar} \\ 5 \ \text{Laminar} & \text{Laminar} \end{cases} \tag{4.255}$$

The two-phase pressure gradient is:

$$\frac{\Delta P}{L} = \emptyset_l{}^2 \left(\frac{dP}{dz}\right)_l \tag{4.256}$$

Friedel (1979, 1980) also proposed a model for the pressure drop determination, based on the parameters E, F and H, evaluated as follows:

$$E = (1 - x)^2 + x^2 \frac{\rho_l f_{vo}}{\rho_v f_{lo}} \tag{4.257}$$

$$F = x^{0.78} \times (1 - x)^{0.24} \tag{4.258}$$

$$H = \left(\frac{\rho_l}{\rho_v}\right)^{0.91} \left(\frac{\mu_v}{\mu_l}\right)^{0.19} \left(1 - \frac{\mu_v}{\mu_l}\right)^{0.7} \tag{4.259}$$

The two-phase mixture density is calculated as follows:

$$\rho_{TP} = \left(\frac{x}{\rho_v} + \frac{1-x}{\rho_l}\right)^{-1} \tag{4.260}$$

The Froude and Weber numbers are calculated as follows, respectively:

$$Fr = \frac{G^2}{gD\rho^2_{TP}} \tag{4.261}$$

$$We = \frac{G^2 D}{\rho_{TP}\sigma} \tag{4.262}$$

The resulting two-phase multiplier is calculated by:

$$\emptyset_{lo}^2 = E + \frac{3.24 \times FH}{Fr^{0.045} We^{0.035}} \tag{4.263}$$

Finally, the two-phase pressure gradient is given by:

$$\frac{\Delta P}{L} = \emptyset_{lo}^2 \left(\frac{dP}{dz}\right)_{lo} \tag{4.264}$$

Another literature model was proposed by Chisholm (1973), where the ratio of the vapor-to-liquid only pressure gradient is given by:

$$Y = \sqrt{\frac{(dP/dz)_{vo}}{(dP/dz)_{lo}}} \tag{4.265}$$

The two-phase multiplier is given by:

$$\emptyset_{lo}^2 = 1 + (Y^2 - 1)\left[Bx^{(2-n)/2}(1-x)^{(2-n)/2} + x^{2-n}\right] \tag{4.266}$$

where the parameter B is given by:

$$B = \begin{cases} \dfrac{55}{\sqrt{G}}, & 0 < Y < 9.5 \\ \dfrac{520}{Y\sqrt{G}}, & 9.5 < Y < 28 \\ \dfrac{15000}{Y^2\sqrt{G}}, & Y > 28 \end{cases} \qquad (4.267)$$

Moreover, n is the power to which the Reynolds number is raised in the friction factor and is given by:

$$n = \begin{cases} 1, & Re_{lo} \leq 2100 \\ 0.25, & Re_{lo} > 2100 \end{cases} \qquad (4.268)$$

The pressure gradient is evaluated as follows:

$$\frac{\Delta P}{L} = \emptyset_{lo}{}^2 \left(\frac{dP}{dz}\right)_{lo} \qquad (4.269)$$

The pressure models presented above will be used to determine the pressure drop in the two-phase section of the condenser of the LHP studied in the chapter 5.

4.6 Conclusions

In this chapter, mathematical models for the temperature distribution of the evaporator and the condenser were proposed as design tools for LHPs. Literature models are also presented and will be used to predict the performance of the LHP in the next chapter. Two approaches were used for the mathematical model development: 2D and 1D. The 2D modeling was proposed to study and determine geometry parameters that will guarantee the correct performance and to allow for the design of the evaporator wick structure of LHP. The temperature and pressure fields allow for the identification of the dimensions of the wick structure able to prevent LHP dry out. From the 1D model approach, a critical theoretical parameter, which allows for the selection of the evaporator geometry and operation mode, was proposed. The analogy between thermal and electrical circuit was used to determine the operation

temperature and heat transfer limits. Several literature models to determine the heat transfer and pressure drops in LHP components, such as evaporator, liquid and vapor lines, were also presented.

5 EXPERIMENTAL AND THEORETICAL ANALISIS OF LHP

In this chapter, an analysis of the geometry design of the wick structure of the loop heat pipe is presented. The thermal and hydraulic 2D models proposed in the last chapter are used to evaluate the influence of geometrical and thermophysical properties of the capillary structure on the performance of the evaporator. A difference of temperature higher than the critical temperature leads to the formation of vapor within the wick structure and increases both the thermal resistance and the operation temperature. Additionally, the heat leak to the compensation chamber increases the temperature of the working fluid, reducing the thermodynamic drive force between evaporator region and the compensation chamber. On the other hand, a large pressure drop in the wick structure reduces the heat transfer capacity of the equipment. Therefore, the geometry design of the wick structure must guarantee the appropriate difference of temperature between the heater and evaporation zone, resulting in a small heat leakage to the compensation chamber, and the minimum pressure drop in the wick structure.

In order to analyze the influence of the geometry parameters in the design of LHPs, the tools developed in chapters 3 and 4 of this work are used to design two LHPs. In the first section, a design procedure is proposed, based on two copper powders with different average particle diameters, selected to be used in the fabrication of the sintered porous media. In the second section, the experimental work developed to validate the hypotheses formulated from the experimental design is presented. In the last section, the 1D model, which is based on the electrical circuit analogy is compared with experimental evaporator operation temperatures.

5.1 Loop heat pipe design methodology

Figure 61 presents the main steps proposed to design an evaporator for a loop heat pipe. Four fundamental aspects are considered: requirements, working fluid, wick structure, and heat and mass transfer.

The fist block shows the requirements of the design divided in two types: geometry and operation. The available area to transfer the heat A_e, and the distance L between the source and heat sink are the geometric requirements or constrictions. The operation temperature T_o and the power transferred q_e are the operational requirements. They are related

to the conditions for safe operation of the electronic device or heat source that need thermal control.

After defining the initial geometry parameters, the working fluid must be selected, according to the operation temperature. In the thermal control of electronic devices, methanol, ethanol and water are frequently used as working fluids. As mentioned in the chapter 2, the working fluid must also be chemically compatible with the wick and case material to avoid the formation of non-condensable gases.

The following steps are used to define the geometrical dimensions of the wick structure. Once the heat transfer area is established according to the application, it is possible to know the minimal active length of the evaporator. Equation (4.15) can be used to establish the critical ratio δ/l and so the thickness of the wick structure. Then, the thermal and pressure fields can be obtained using the 2D-model to determine the temperature distribution and pressure drops in the wick structure and to evaluate the performance of the geometry. As mentioned in chapter 4, the pressure field in the wick structure is coupled with the temperature field by the boundary condition in the evaporation surface. The thermophysical properties can be evaluated from the proposed models or experimental data. The wick structure should provide the heat and mass transfer to the evaporation region and to avoid, as much as possible, heat leakage to the compensation chamber. The 2D-model allows for the analysis of the behavior of wick structure in the worst operation conditions, guaranteeing a safe design for the application of the LHP.

After that the geometrical dimensions are determined, if the temperature distribution and pressure field are well behaved, the loop heat pipe performance can be determined using the 1D-model. According to Maydanik *et al.* (2011b), the failure of these devices occurs when the vapor is produced inside the wick structure. The presence of vapor within the porous media occurs due to the insufficient capillary pumping (able to continuously refill the whole wick structure) and to the superheating of the liquid above the critical temperature. The temperature criterion is evaluated using the 2D model. To determine the capillary limit, all pressure drops in the loop must be calculated, including the pressure drop of the wick structure. The first approximation to determine the fluid inventory is to consider that all heat applied is transferred to evaporation zone. The operation temperature is obtained from the heat balance equation, when the ratio between the total pressure and temperature in the wick is equal to slope of the pressure-temperature curve, at the temperature of operation.
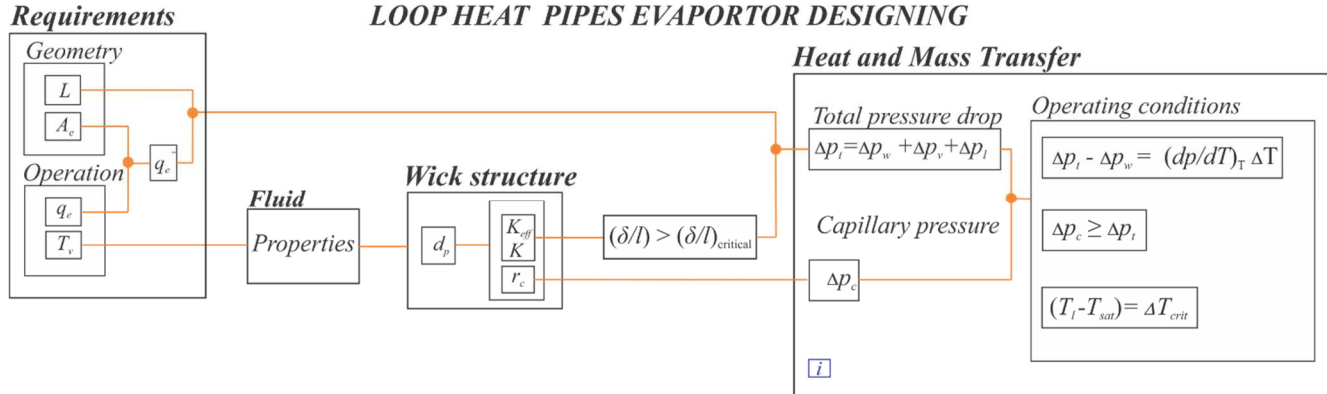
Figure 61 - Design procedure for loop heap pipe.

.

5.5.1 Evaporator active section

From the measurements performed with the defined type of powders and from the models developed, it can be concluded that for an average particle diameter smaller than 20 µm, permeability and effective thermal conductivity are not adequate to be used in the fabrication of the evaporator of a LHP. From this particle type, the permeability begins to decrease and the thermal conductivity increases. Low permeability increases the pressure drop inside of wick structure, thus reduces the heat transfer capacity. On the other hand, high effective thermal conductivity increases the heat leak to compensation chamber, increasing the possibility to form vapor in the compensation chamber. The wick geometry should be designed to provide an equilibrium of the response of this property in the heat and mass transfer, minimizing the pressure drop and heat leak.

The following study has the objective to identify the effects of each one property, comparing two types of powder and the wick parameters geometries (length of bottom β and thickness of the wick active zone δ) on the performance of the LHP evaporator. Therefore, the temperature distribution is obtained from the 2D-model presented in chapter 4 and its maximum temperature and the heat leakage are determined. Table 13 presents a summary of the thermophysical properties of the wick structure, fabricated using powders B and C, measured in the laboratory.

Table 13. Properties of the copper sintered porous media fabricated for the evaporator of the LHP tested.

Properties	Powder B	Powder C
Particle average diameter[µm]	36.59	49.72
Porosity	42.31±2.86	53.46±3.87
Effective thermal conductivity [W/m·K]	59.52±0.46	42.86±0.31
Permeability [m^2]	$8.15 \cdot 10^{-13} \pm 4.09$	$1.99 \cdot 10^{-12} \pm 1.02$
Effective porous radio [µm]	23.04±1.81	21.04±2.2

As already highlighted, the selection of the appropriate wick thickness depends on the material, the geometry of the porous media, and the working fluid selected. The plots of the ratio δ/l, Equation (4.15), as a function of the evaporator temperature are shown in the Figure 62 for a wick structure whose parameters are given by Table 13, and for two different working fluids: water and methanol. In this figure,

the value of δ/l for water at 60 °C is highlighted for both powder structures. These values will be used in the design of the LHP to be tested experimentally in the next section. In the Figure 62, one can see that, as the reference temperature decreases, thicker wick structures are necessary. In addition, one can also observe that methanol requires thinner wicks than water for a same reference temperature.

To understand this behavior, each term of the critical relation δ/l equation (Equation (4.15), here reproduced) are compared, for both working fluids:

$$\overbrace{\left(\frac{\delta}{l}\right)^2}^{geometry} \approx \underbrace{\frac{k_{eff}}{K}}_{wick\ properties} \overbrace{\frac{\mu_l}{\rho_l h_{lv}}}^{fluid\ properties} \underbrace{\left(\frac{dP}{dT}\bigg|_T\right)^{-1}}_{Thermodynamic} \quad , \quad (4.15)$$

One can see that the first term is the similar for both liquids, because, according to Florez et al. (2013), the influence of the liquid in the effective thermal conductivity is negligible The second term corresponds to the working fluid thermophysical properties and, besides the liquid dynamic viscosity and density for water and methanol are not very different, the latent heat of water is approximately twice the latent heat of methanol. This means that more methanol than water is expected to be evaporated for the same heat load. As the evaporated fluid must be replenished, more methanol is expected to be flow through the wick and so higher pressure drops for methanol are expected. Considering only this effect, methanol could need of a thicker wick, for the same heat load. However, this behavior is compensated by the last term, related to the slope of the curve pressure-temperature, which, for water is around four times smaller than methanol´s, for the temperature level analyzed.
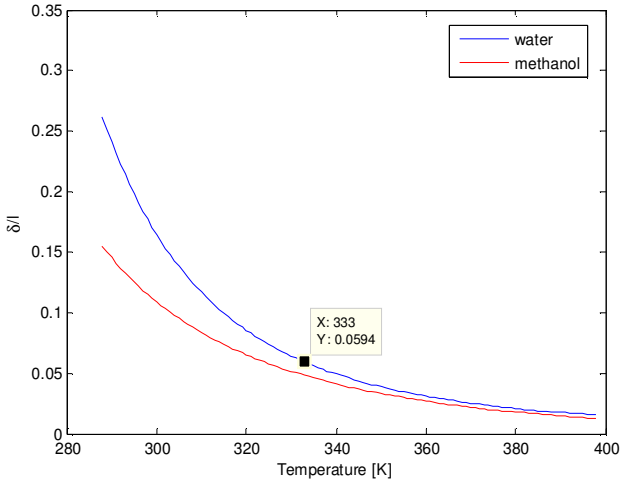
a)
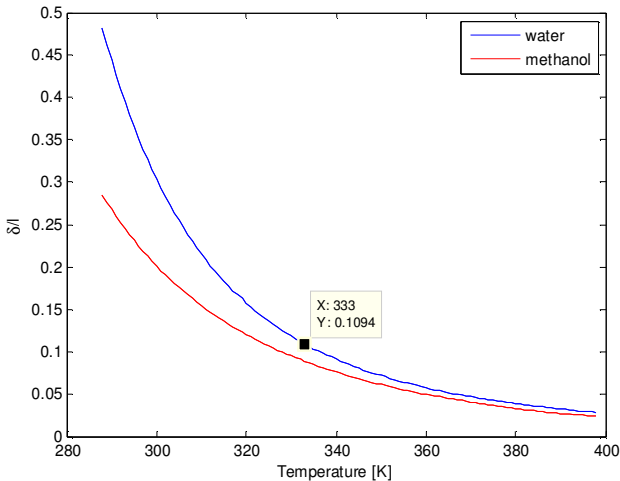
b)

Figure 62 - Ratio of wick thickness to evaporator length (δ/l) as a function of the operation temperature. a) Powder B, b) Powder C.

5.1.2 Design of the tested LHP geometries

The constructed LHP was made of copper and consisted of: an evaporator (with similar geometry to the one shown in Figure 63; a condenser (three-turn coil, made of conventional tubes of 1.62 mm of

internal diameter); a liquid line (straight tube with one elbow and one turn) and a vapor line (straight tube with one elbow). The geometry and dimensions of the LHP are shown in Table 14.

Table 14. LHP geometry parameters.

Designed LHP	
Loop geometrical parameter	
Effective Length l	30.22 mm
Wick external radius ξ	5.6 mm
Evaporator diameter	12.70 mm
Case material	Copper
Condenser serpentine and liquid and vapor tube diameter	1.62 mm
Length of tube vapor line	81.6 mm
Length of tube liquid line	252.4 mm
Condenser length	154 mm
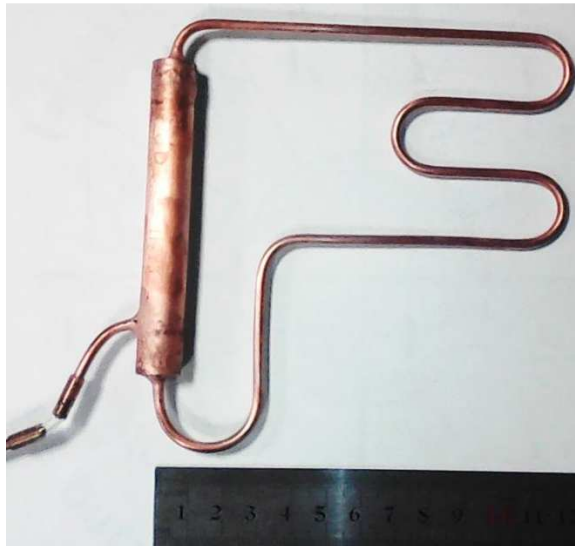
a)
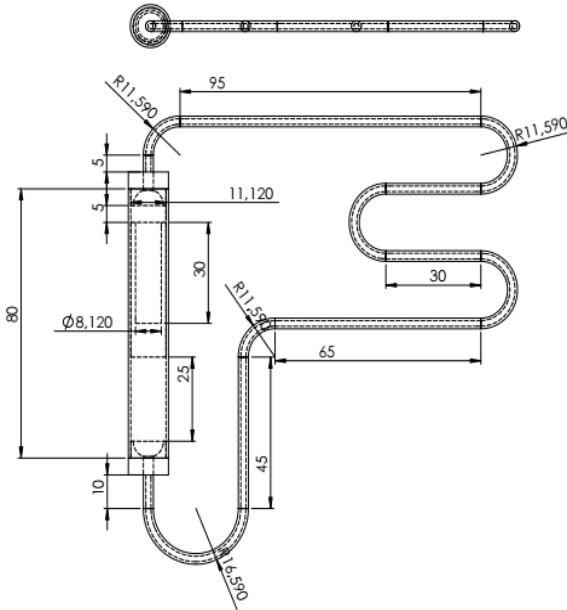
b)

Figure 63 - Tested LHP geometry. a) schematic drawing, b) Photography.

The fabrication process of the LHP used in this work can be divided in several steps:

- Cutting and bending of the tubes for the fabrication of the evaporator, the condenser and vapor and liquid lines, in the required dimensions.
- Machining caps of the evaporator section.
- Cleaning of pieces used in the several components of the LHP using detergent, acetone, trichloroethylene and finally a solution of sulfuric acid at 10 % in volume.
- Fabrication of the wick structure with deposition of powder in the case of the evaporator (see picture of Figure 64). To obtain the designed thickness of the layer in the evaporation section, a steel matrix with the desirable diameter is employed.
- Sintering of copper powder in special electrical furnace, with atmosphere and temperature controlled.
- Assembling and welding of all components using acetylene-oxygen welding. After this step, the external surface is again cleaned with sulfuric acid solution to remove ash. This process

must be carried out carefully in order to avoid that the cleaning solution comes to interior of device.

- Evacuating of the LHP is followed by leak testing using a spectrometer analyzer (see Figure 65). Helium gas is atomized on the external wall of LHP and the spectrometer detects the presence of gas inside of LHP.
- Filling with the working fluid.

Figure 64 - Evaporator LHP preparation for sintered process of copper powder.
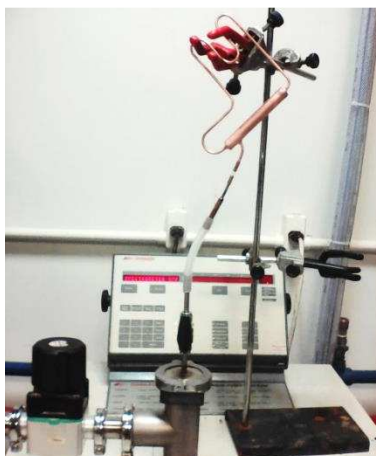
Figure 65 - Leak detection on the LHP with the spectrometer analyzer.

5.1.2.1 Wick geometry evaporator ANOVA analysis

This section presents a two-dimensional temperature distribution analysis of the porous media using the model presented earlier in the chapter 4. Statistical tools are used to study the influence of the geometric parameters on the thermal performance of evaporators of the LHP geometry under study (see Figure 63), with wicks made from the porous media described in Table 10. The values for the maximum temperature T_{max} and the heat leak q_{cc} are used as the response variables. The following parameters were selected for this analysis: the type of sintered porous media based on the different values of powder average particle diameter, ratio between evaporator thickness δ and evaporator length l (δ/l), and ratio between the bottom evaporator length β and evaporator length l, (β/l). Two levels (higher (+) and lower (-)) were selected for each parameter or factor. The levels for the parameter δ (which depends on the fluid, as established by equation (4.15)), were employed in this study, considering water as the working fluid. Table 15 shows the parameter values adopted in this study. The combination of these variable levels results in $2^3 = 8$ experiments of a factorial statistical design. The response variables were obtained for each experiment using the temperature distribution of 2-D model, the total pressure drop and the equilibrium thermodynamic Equation (2.4) presented in chapter 4.

Table 15. Factors adopted for the factorial statistical design.

Factor levels	Factor		
	A = Particle diameter	B = Evaporator thickness-length ratio δ/l	C = Evaporator thickness-length ratio β/l
Low (-)	36.59 μm	$(\delta/l)=(\delta/l)_{crit}$	0.10
High(+)	49.72 μm	$(\delta/l)=1.2*(\delta/l)_{crit}$	0.20

The combination of the parameters for the experimental design performed is presented in the Table 16. One should note that the numerical levels for the factor (δ/l) change according to the characteristic powder diameter. The results, using the models presents in the former chapters, for the maximum temperature T_{max} and heat leak q_{cc} are presented in Table 17.

Table 16. Combination of parameters for the experimental design performed.

Expt. N°.	Factorial effect			Original value		
	A	B	C	Powder	(δ/l)	(β/l)
1	-	-	-	36.59 μm	0.10940	0.10
2	+	-	-	49.72 μm	0.05940	0.10
3	-	+	-	36.59 μm	0.13130	0.10
4	+	+	-	49.72 μm	0.07128	0.10
5	-	-	+	36.59 μm	0.10940	0.20
6	+	-	+	49.72 μm	0.05940	0.20
7	-	+	+	36.59 μm	0.13130	0.20
8	+	+	+	49.72 μm	0.07128	0.20

The influence of each one of the parameters on the responses (T_{max}, q_{cc}) was evaluated using Analysis of Variance (ANOVA) (MONTGOMETY, 1991). The Statistica® software was used for data computation, considering a confidence interval of 95 % (α=0.05 of significance level).

Table 17. Responses for the factorial statistical design.

Expt. N°.	Factorial effect			Responses	
	A	B	C	T_{max} °C	q_{cc}
1	-	-	-	3.45	0.7234
2	+	-	-	8.10	2.0292
3	-	+	-	2.70	0.2845
4	+	+	-	7.01	2.1200
5	-	-	+	3.46	0.1271
6	+	-	+	8.10	0.8070
7	-	+	+	2.65	0.0205
8	+	+	+	7.01	0.6900

The analysis of variance for factorial design with the maximum temperature as response is presented in Table 18. The ANOVA test identified a significant effect ($p < 0.5$) for the factor "powder particle diameter" and ratio δ/l, where p is the probability calculated using Fisher Probability Distribution Function. The parameter β/l showed no

significant effect on T_{max}. These results can also be observed in the Pareto chart presented in Figure 66, where the red line represents the level of significance considered for the analysis (5 %). The significant factors are those that present higher effects than the level of significance.

Table 18. Analysis of variance for maximum temperature.

Factor	Sum of Square	Degrees of Freedom	Mean Square	F	p
(1)Powder	40,32020	1	40,32020	89600,44	0,002127
(2) (δ/l)	1,74845	1	1,74845	3885,44	0,010212
(3) (β/l)	0,00020	1	0,00020	0,44	0,625666
1 by 2	0,04805	1	0,04805	106,78	0,061417
1 by 3	0,00020	1	0,00020	0,44	0,625666
2 by 3	0,00045	1	0,00045	1,00	0,500000
Error	0,00045	1	0,00045		
Total Sum of Square	42,11800	7			
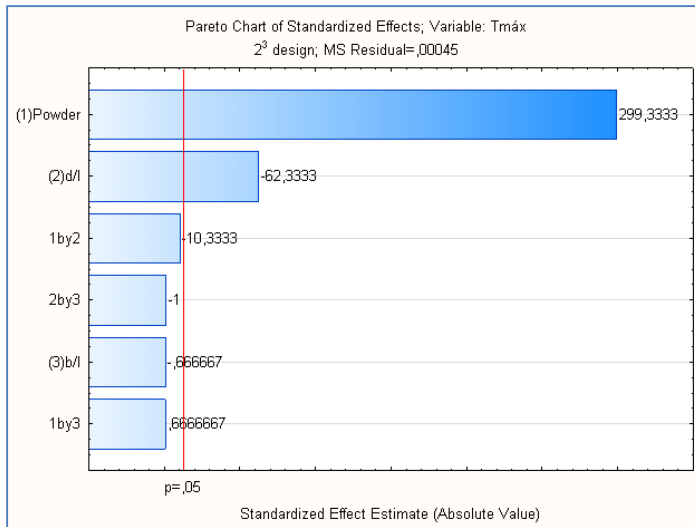
Figure 66 - Pareto Chart of effects for analysis of variance for maximum temperature.

Figure 67 shows two graphs of response surfaces for the maximum temperature as a function of powder type and the ratios δ/l and β/l. The influence of the factors analyzed can be observed form these figures, emphasizing the effect of the powder type and the relations δ/l on the maximum temperature and the lack of effect of the ratio β/l.
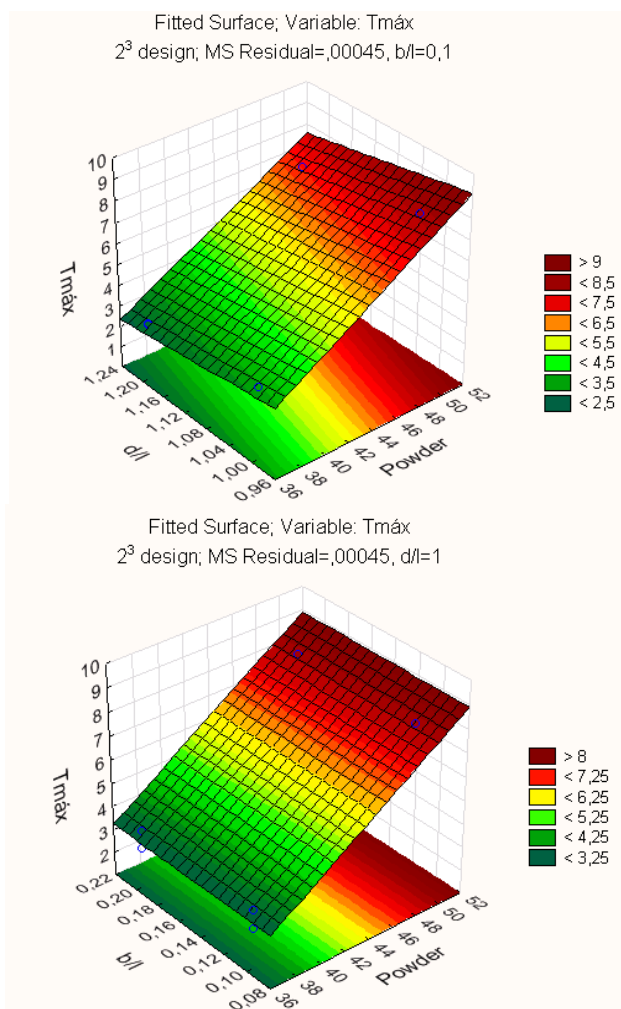
Figure 67 - Response Surface for the maximum temperature as a function of powder type and the ratios δ/l and β/l.

The analysis of variance for factorial design, with the heat leak q_{cc} as response, is presented in Table 19. The statistical analysis with ANOVA identified that the main factors and their interactions are not significant (p > 0.5) on the response heat leak q_{cc}. From this analysis, the best thermal design is the case 7. This design produces the lowest temperature difference and heat leak. From these statistical analyses one can see that a wick evaporator geometry with $1.2 \cdot (\delta/l)$ can be used to guarantee the operation of LHP evaporator. The analyses also show that (β/l) larger than 0.1 is sufficient to separate the evaporation active zone and the compensation chamber.

Table 19. Analysis of variance for heat leak q_{cc}.

| Factor	Sum of Square	Degrees of Freedom	Mean Square	F	p
(1)Powder	2,520798	1	2,520798	69,13210	0,076201
(2) (δ/l)	0,040855	1	0,040855	1,12044	0,481911
(3) (β/l)	1,542207	1	1,542207	42,29454	0,097129
1 by 2	0,033709	1	0,033709	0,92446	0,512498
1 by 3	0,401363	1	0,401363	11,00726	0,186371
2 by 3	0,001938	1	0,001938	0,05314	0,855770
Error	0,036464	1	0,036464		
Total Sum of Square	4,577334	7			

5.2 Experimental work

To evaluate the thermal performance of the first LHP constructed, an experimental setup was designed and built. Controlled thermal energy was provided by four electric cartridge heaters (maximum power generation capacity of 100 W), which were inserted in a thick copper plate, with the low surface machined so the evaporator could accommodate the heater perfectly (see Figure 69). The heaters were fed by a controlled electric energy source equipment. Cooling was provided by means of a small heat exchanger, made of a thick hollow aluminum block, with internally machined grooves, cooled by water from a thermal bath circulated.

A picture of the experimental setup is presented in Figure 68. The experiment control and the thermocouple readings were provided by a data acquisition system and respective software.
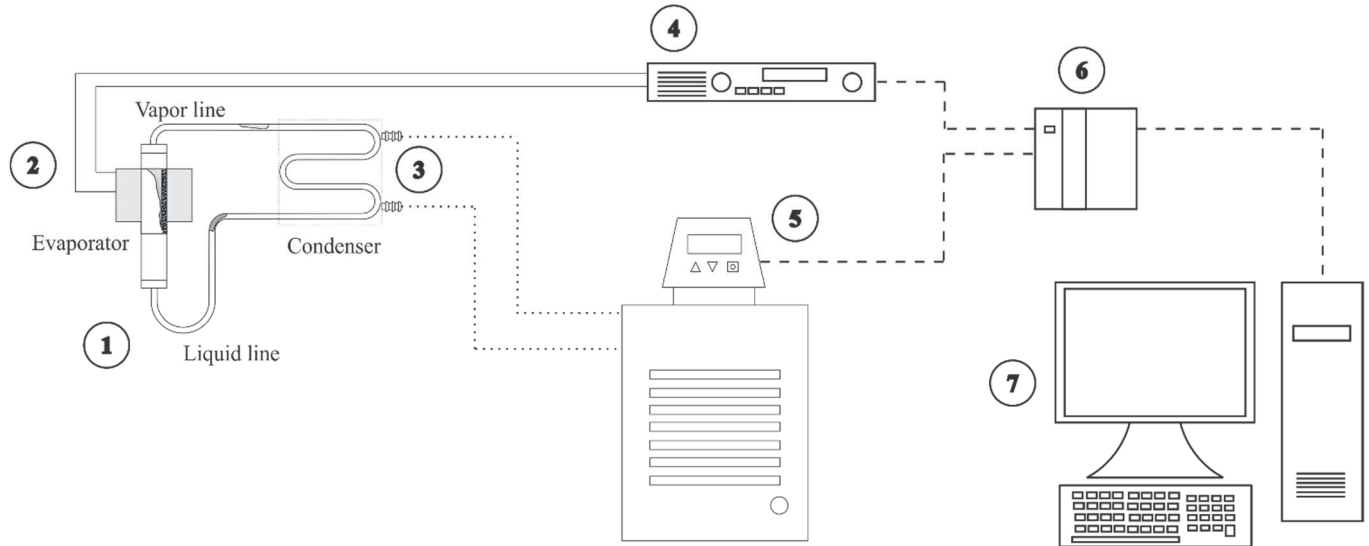
Figure 68 - Experimental setup used in the tests. a) Photography, b) Schematic of test LHP: 1. Sample, 2. Heater, 3. Heat exchanger, 4. Power source, 5. Thermal bath 6. data acquisition system, 7. Computer.
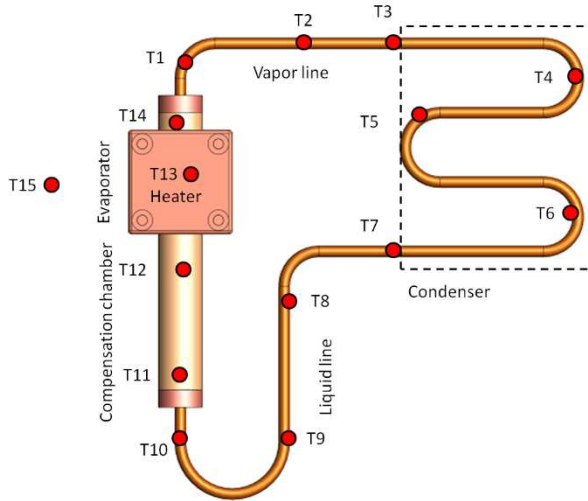
a)
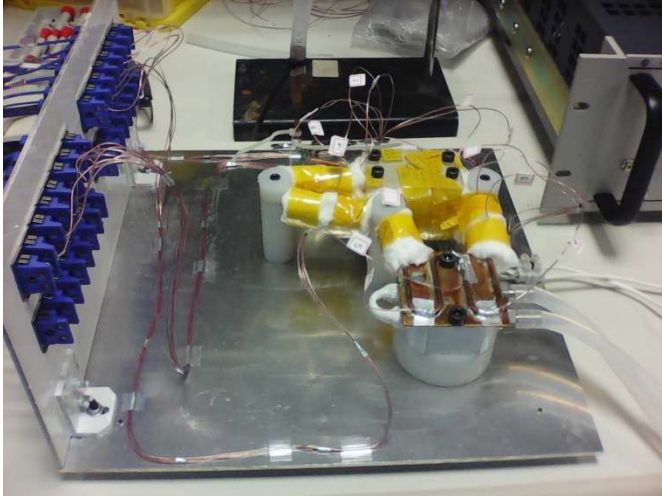
b)

Figure 69 - Tested LHP geometry and thermocouple locations. a) schematic drawing, b) Photography.

Using the Equation (4.15) and the 2D-model developed in the present work, two configurations of LHP evaporators, were designed to

operate with methanol (Case A) and water (Case B). Table 20 presents the geometry of the prototype constructed and tested

Table 20. Designed LHP geometry parameters and thermophysical properties.

Designed LHP		
Wick geometrical parameter		
Wick Length l	30 mm	30.22 mm
Wick thickness δ	1.6 mm	2.2 mm
Wick Isolated length φ	0.11mm	0.11mm
Wick external radius ξ	5.56 mm	5.6 mm
Wick internal radius ω	4.06 mm	3.4 mm
Wick bottom length β	8 mm	7.89 mm
Wick thermophysical properties		
Wick effective thermal conductivity	42.86 ± 0.31 W/m·K	
Wick permeability	1.99×10^{-12} m^2	
Effective porous radius	24.1 μm	
Porosity	53.46 ± 3.87	
Loop geometrical parameter	**Case A**	**Case B**
Evaporator diameter	12.70 mm	12.70 mm
Working fluid	Methanol	Water
Case material	Copper	Copper
Fluid charge	2.4 ml	2.4 ml
Condenser serpentine and liquid and vapor tube diameter	1.62 mm	1.62 mm
Length of tube vapor line	81.6 mm	81.6 mm
Length of tube liquid line	154 mm	154 mm
Condenser length	252.4 mm	252.4 mm
Heat sink temperature	20 °C	20 °C

The LHP was instrumented using 15 thermocouples located according to the schematic of the Figure 69. The uncertainty associated to thermocouple measurement is ±0.7 °C.

Figure 70 shows a plot of the temperature (left vertical axis) and electric power input (right vertical axis) as a function of time, for the LHP Case A, operating in steady state conditions. The steady state conditions are considered achieved when the variations of all the monitored temperatures are smaller than 1°C. The evaporator temperatures (thermocouples T11, T12, T13 and T14, see Figure 69 for location) show obviously, the higher levels, while the condenser

(thermocouples T3, T4, T5, T6 and T7) show lower temperatures. The startup of the device is characterized by the temperatures T1, T2 and T3 sudden increase. One can see that, for the first power input of 5 W, the LHP took around 2000 seconds to start up, which can be observed when the liquid line temperatures (Thermocouples T8, T9 and T10) starts to decrease, which means that the condensate reached the liquid line close to the compensation chamber (in other words, the working fluid cycle is closed). After that, the system operated for the power inputs of 10, 15, 20 and 25 W, showing better performances (the temperature difference between evaporator and condenser decreases), for higher power inputs. After 30 W, the system stopped working. In the next section this limit is analyzed.
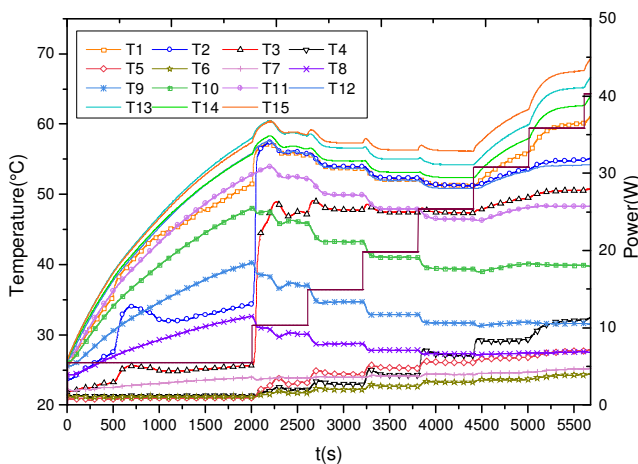
Figure 70 - Thermal behavior of the LHPs described in Table 20, operating with methanol (case A).

The same LHP was then filled with water and tested (Table 20, right column). The thermal behavior of this LHP with water is shown in Figure 71, for the same conditions tested in Figure 70. One can easily see from this plot that the LHP did not work with water. This behavior was expected as the wick thickness was designed for methanol (see Section 5.5.1 explanation), showing that the design tool developed for determination of the wick thickness was correct.
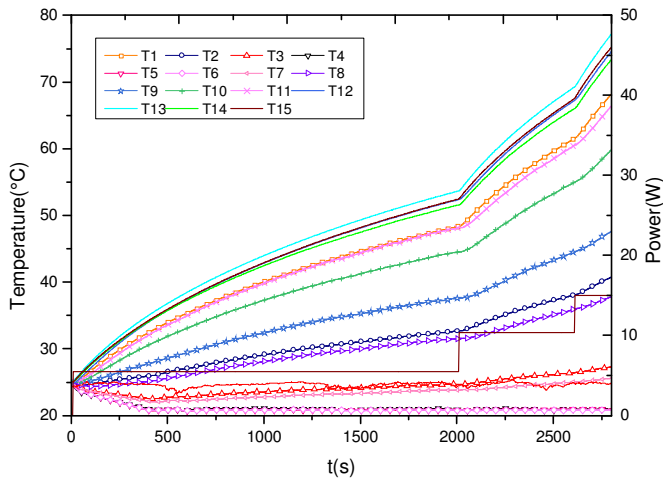
Figure 71 - Thermal behavior of the LHPs described in Table 20, operating with water (case A).

Another LHP was designed to operate with water, as shown in Case B of Table 20. Comparing Cases A and B (see Table 20), one can observe that these LHP's have basically the same geometry configuration, with the major difference being the wick thickness. Figure 72 shows the thermal behavior of Case B. In this figure, one can see that the startup was possible only after the application of 15W after approximately 2500 seconds, when the temperatures T1, T2 and T3 starts a sudden increase. The LHP operated quite well up to 60 W of power input. Actually, the thermal performance of the device increased from 15 to 60 W, which can be observed by the decreasing of the temperature difference between evaporator and condenser. After this power level, the LHP started to show indications that the operational limits were close, as temperature pulses are observed for thermocouple T4, located in the condenser serpentine, near to condenser entry region, showing the presence of vapor. This means that, probably, the condenser is reaching its heat transfer limit before the evaporator. The plots of Figure 70, Figure 71 and Figure 72 show that the proposed model for the determination of the thickness of the porous media, among other usages, gives a good estimative of this parameter and should be used as a design tool for LHPs and heat pipes.
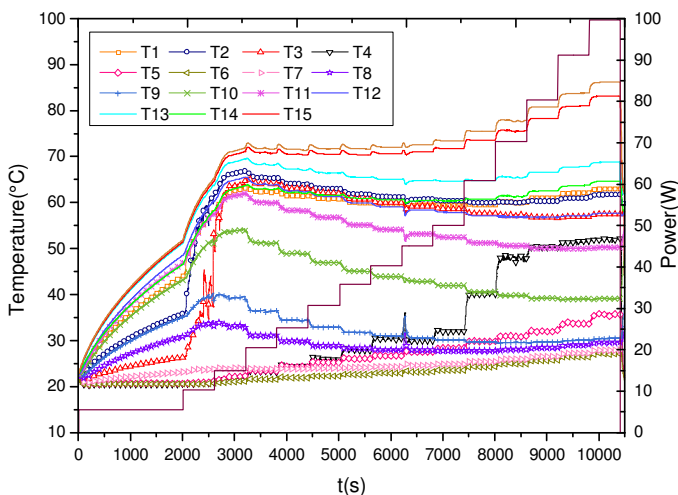
Figure 72 - Thermal behavior of the LHPs described in Table 20, operating with water (case B).

5.3 Validation of the mathematical model

In this section, the temperature distribution obtained by the mathematical model is compared with the numerical simulation results. Commercial software Ansys was used in this study. The physical model sketched in Figure 35 was numerically reproduced. The objective of this model was to obtain results that would be impossible to obtain experimentally, such as the heat fluxes in the boundaries of the porous media and the temperature distribution along the wick. This numerical study is used in the validation of the theoretical model. The simulations were considered converged when the RMS residue (difference in the temperatures for two consecutive iterations for all elements) was less than 1×10^{-6}. Table 21 shows the geometry of the evaporator porous media used in this comparison.

Table 21. Designed LHP geometry parameters and thermophysical properties.

Designed LHP	
Wick geometrical parameter	
Wick Length l	30.22 mm
Wick thickness δ	2.2 mm
Wick Isolated length φ	0.11mm
Wick external radius ξ	5.6 mm
Wick internal radius ω	3.4 mm
Wick bottom length β	7.89 mm
Wick thermophysical properties	
Wick effective thermal conductivity	42.86 ± 0.31 W/m·K
Wick permeability	1.99×10^{-12} m^2
Effective porous radius	24.1 μm
Porosity	53.46 ± 3.87
Thermal conditions	
Temperature of the compensation chamber T_{cc}	58.7 °C
Temperature of evaporator T_v	60 °C
Power input q_e	70 w

The heat leakage were determined theoretically using the heat balance equation, Equation. (4.92) and, numerically, directly with the software results (see Table 22). From this table one can see that the calculation of the power transferred to the meniscus q_ω and the power lost to the compensation chamber q_β was not exactly the same, although the total heat transferred was the same, 70 W. Actually, this difference can be imputed to the discretization error, which is a function of the number of mesh elements employed, as well as the approximation of uniform flux used to couple of solid and hollow cylinder.

The temperature and heat transfer data shown in Table 22 were obtained using 7.81×10^6 mesh elements. To obtain the same precision, around 300 terms of the Fourier series were employed, demanding lower computational processing time than that required for the numerical simulations.

Figure 73 shows the 3D numerical temperature distribution of the wick structure studied. One can see from this figure that the temperature field is basically 2D and that the 2D hypothesis adopted to the analytical model is quite precise.

Table 22. Comparison between numerical and analytical heat powers: q_x (meniscus) and q_y (compensation chamber).

Results	Analytical solution 2D	Numerical simulation
Heat leak q_β	-1.22 W	-1.30 W
Heat transfer to meniscus q_ω	-68.74 W	-68.75 W
Power input q_e	69.96 W	70.05 W
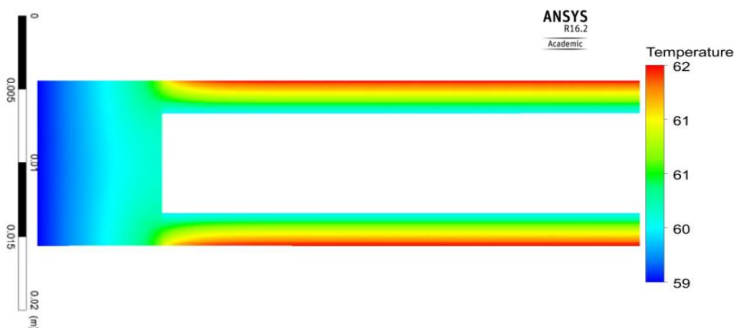
Figure 73 - 3D numerical temperature distribution**.**

The temperature distributions obtained from both numerical and mathematical analysis are shown in Figure 73. One can observe from this figure that the temperature distributions show very similar behaviors. The largest temperature gradients are observed vertically, from the top to the bottom direction (heat delivery surface to the meniscus direction). In the area behind the heated region (right), the temperature field has a quasi-one-dimensional behavior. Two larger direction variations are actually observed in the insulated left region of the evaporator (solid cylinder). Note that the numerical simulation map (upper map in Figure 73) is drawn observing the geometry of the actual wick structure studied. The comparison between theoretical model and numerical simulation results can also be observed from the temperature profile plots, for two porous media cross sections, vertical and horizontal lines shown in Figure 74.

Figure 74 - Cross section position for the plots shown in Figure 35.

Figure 74 shows the comparison between temperatures, obtained from analytical and numerical models, as a function of z at $r = 5.6$ mm and as a function of r at $z = 7.89$ mm. One can see from these plots that the temperature curves are quite similar for $r = 5.6$ mm, considering both temper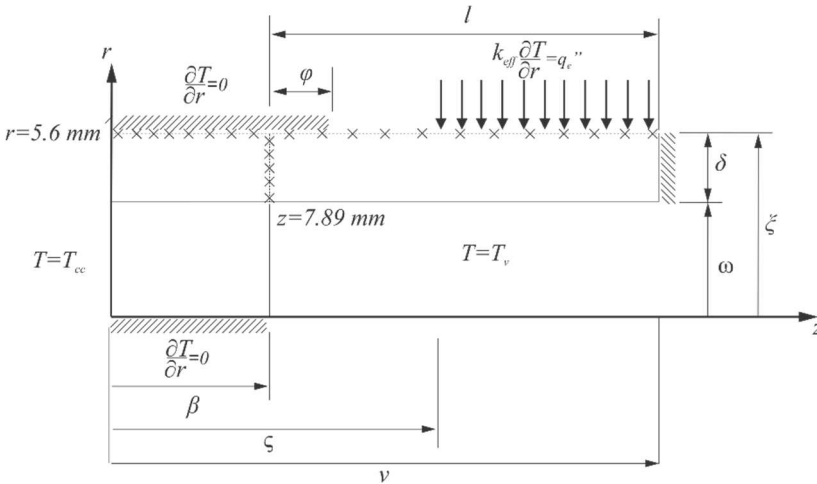ature level and distribution. The average difference between theoretical and numerical simulation models is around 0.9 °C, equivalent to 1.5 % (modulus of the ratio of the difference between maximum theoretical and numerical temperatures and the maximum numerical temperature), showing the good quality of the model. In the other hand, the temperature curves for $z = 7.89$ mm show that the difference between temperatures increase as r increases. The highest difference is 1.51 °C, equivalent to 2.4 %. This difference can be explained by the effect of the hypothesis of uniform heat flux used to couple the two domains, in the analytical solution.

Concluding this section, one can see that the theoretical model was able to reproduce the heat fluxes at the evaporation surfaces, the heat leaks and the temperature distribution along the wick structure. Therefore, the theoretical model can be considered validated, showing that this model can be used in the design of the LHP evaporators.

In the next section, a complete LHP, using the designed evaporator, was constructed and tested. Also, the testing results are discussed.
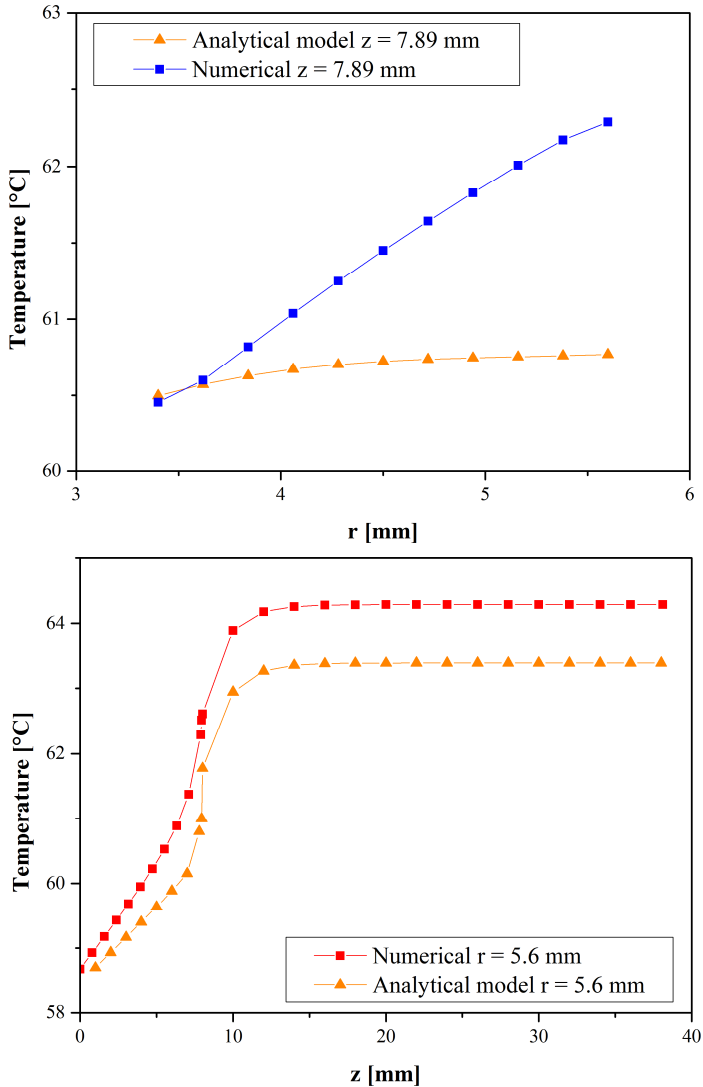
Figure 75 - Comparison between numerical and analytical temperature profiles for radial (above) and longitudinal (below) cross sections, according to positions shown on Figure 74.

5.4 Temperature and pressure fields analysis

This section presents an analysis of the temperature and the pressure fields. Thermal and hydrodynamic responses of the wick geometry shown in Table 20 (case B) is modeled using the equations developed in chapter 4 for a power load of 70 W. The pressure drop in the loop calculated from the pressure models in the condenser, liquid and vapor lines are used to determine the boundary condition for the thermal model. The properties of the working fluid were calculated at 60°C. The objective of the analyses is to evaluate the feasibility of the proposed geometry to operate under the thermal power of 70 W, and to evaluate the presence of vapor bubbles inside the wick structure, the heat leak and pressure a maximum temperature. Figure 76, Figure 77, Figure 78, and Figure 79 present the contours and surfaces of the temperature and pressure field for the wick geometry described in Table 20 (case B).

Figure 76 - Contours of temperature field of LHP described in Table 20, (a) Domains 1 and 2, (b) Domain 3.

(a)

(b)

Figure 77 - Surfaces of temperature field of LHP described in Table 20, (a)
Domains 1 and 2, (b) Domain 3.

Figure 78 - Contours of pressure field of LHP described in Table 20, (a) Domains 4 and 5, (b) Domain 6.
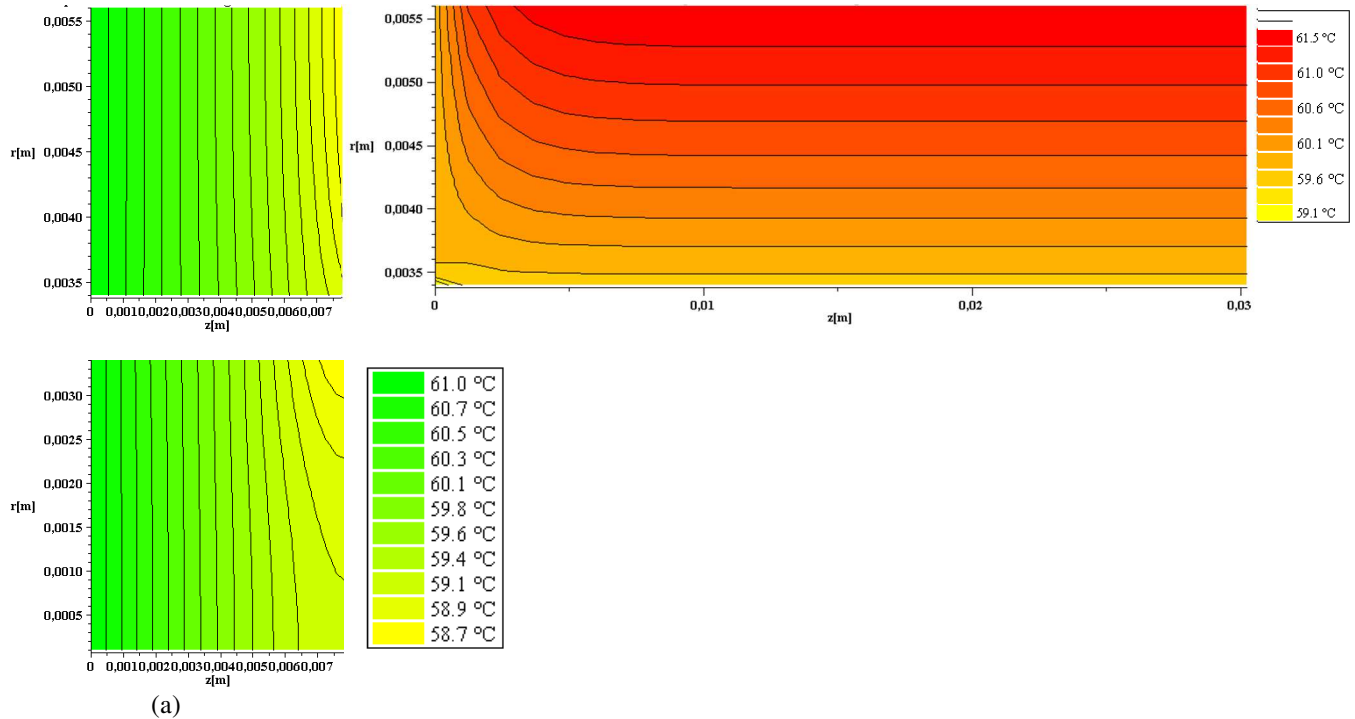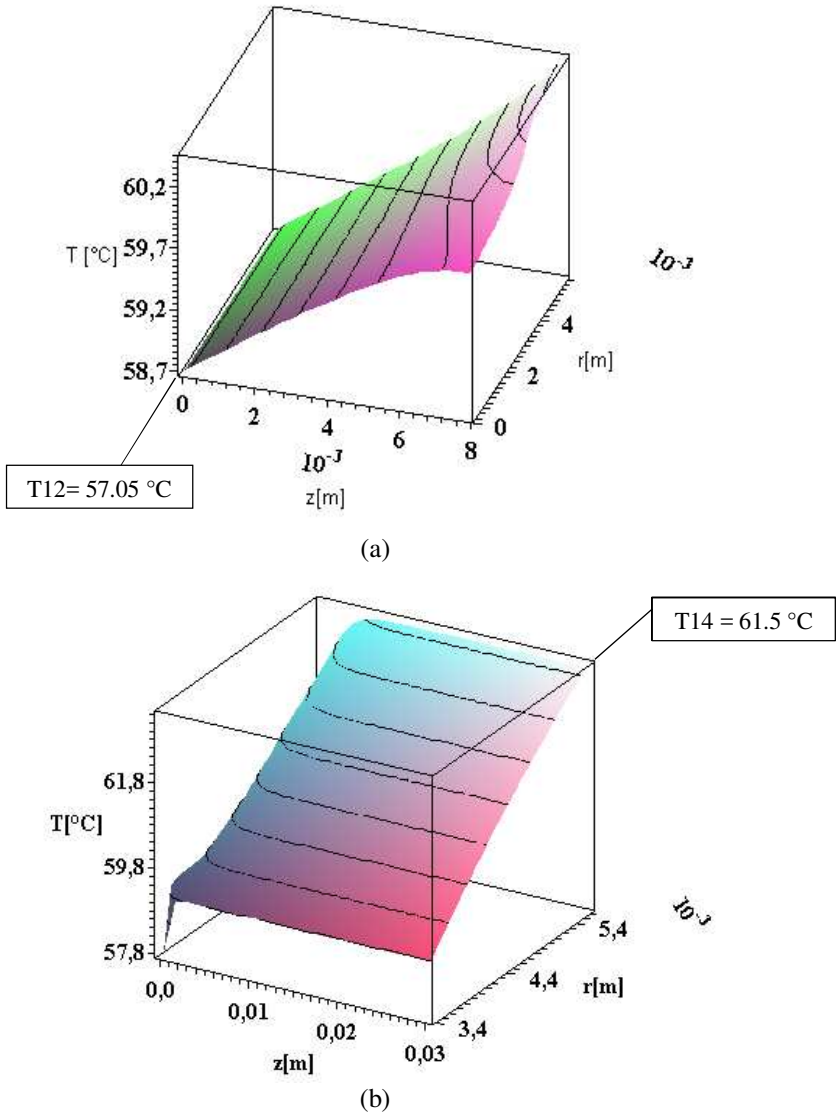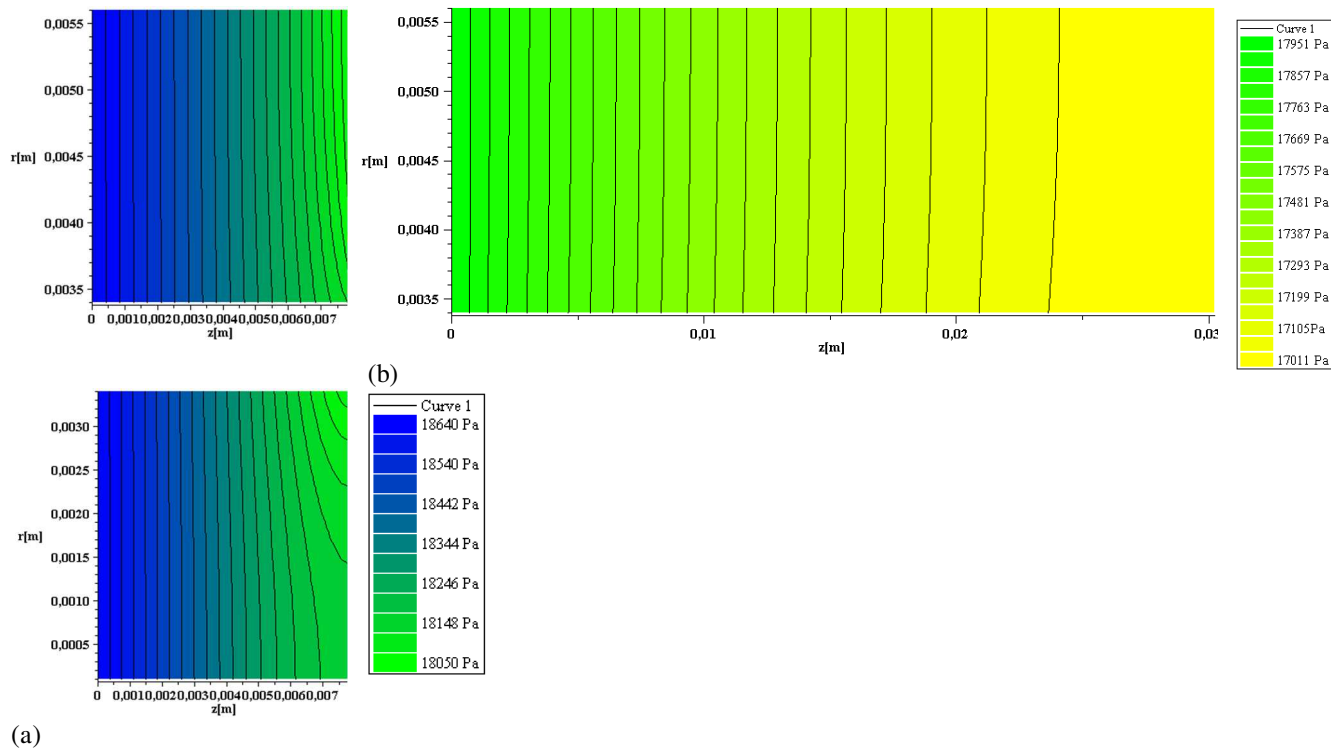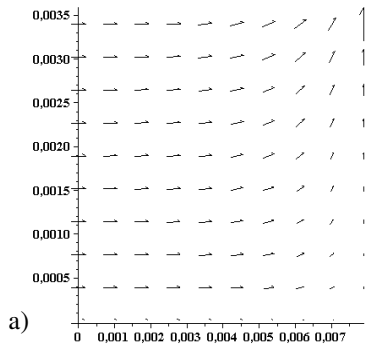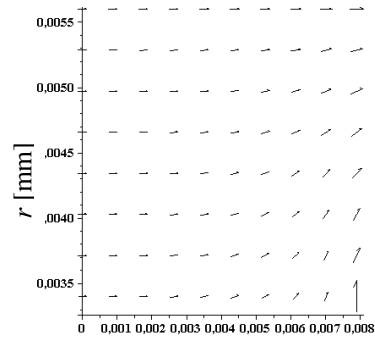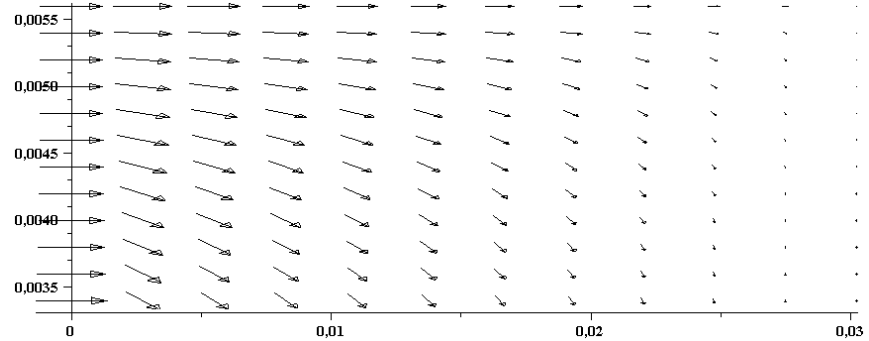
204

Figure 79 – Pressure gradients of LHP described in Table 20, (a) Domains 4 and 5, (b) Domain 6.

The thermodynamic equilibrium was evaluated for a vapor temperature of 60 °C using the Equation (2.4) and for a power input of 70 W. In the interface between the domains 1-2 and 3 for the point (β,ξ), the maximum temperature was 60.43 °C. This value shows that heating at the interface is very low. Therefore, the evaporation in the interface is small for this power load. The heat ratio that crosses the interface at $z=\beta$ and $\omega < r < \xi$ calculated from the equations presented in Table 11 was 0.85 W, which represents only 1.2 % of the total power applied into the heating surface. As shown by the ANOVA analysis, the heat leak is very low due to the strong temperature gradient in the radial direction of the hollow cylinder domain. From the Figure 77a and Figure 77b for the domain 3, one can see that maximum temperature at point (υ,ξ) is 63.4 °C. For the same wick geometry, the contours and gradients of the pressure field are presented in the Figure 78 and Figure 79. As one can see, the highest-pressure drop is in the domain 6 and it is about 64 % of the total pressure for this wick structure evaporator. In Figure 78b, the pressure at point (υ,ξ) is 17.02 kPa.

The total pressure drop should be smaller than the maximum capillary pressure of the LHP under operation. The pressure drop increases with the power load until the pumping capacity is achieved. This condition is called the capillary limit. However, the pressure drop increase is also produced by the presence of vapor inside of the wick structure that blocks the working fluid flow to the evaporative surface. Therefore, it is necessary to evaluate whether the thermodynamic state inside of wick structure is above the critical conditions where vapor is formed. In Figure 80, the thermodynamic state of the compensation chamber, the vapor zone and the point (υ,ξ) of the wick structure are plotted in the P-T diagram for water. From this figure, one can see that the temperature at the point (υ,ξ) is higher than the temperature of saturation corresponding to pressure 17.02 kPa. Hence, the working fluid (water) at this point is a superheated liquid with $(T_l - T_{sat}) = 6.72$ °C. To determine if bubbles can be formed in this condition, the superheating $(T_l - T_{sat})$ should be compared to the superheating criteria. Superheating approach from homogeneous nucleation is very high to initiate the boiling at liquid-solid interface (CAREY, 2007). Usually, the literature presents criteria based on the theory of heterogeneous nucleation, which is the nucleation at the interface between the fluid in metastable state and a solid phase contacting it. The critical difference of temperature using Equation (4.210) for point (υ,ξ) is 10.45 °C.
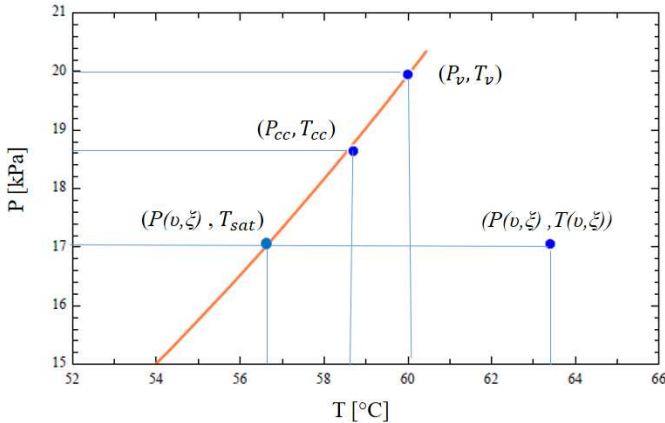
Figure 80 - P-T diagram for thermodynamic analysis of the LHP described in Table 20 (case B).

The thermodynamic analysis of this specific point shows that this wick geometry can operate for a power load 70 W without formation of bubbles inside, according to the criteria calculated by equation (4.210). On the other hand, Maydanik *et al.* (2011b) and Faghri (1995) explain that LHP's may continue to operate if the bubbles leave the wick structure through the liquid phase. Using the temperature and pressure field is possible to determine if a region inside of the wick structure present the formation of bubbles. The blockage of vapor can reduce the working fluid transversal flow area, making the device to achieve the capillary limit.

5.5 Limit and operating temperature

One should remember that the 2D-model (see chapter 4) considered that all heat transfer is through the wick structure. However, the high thermal conductivity of the evaporator case and the strong unidimensional heat transfer behavior observed in the wick geometry allows the application of a 1D model, keeping an acceptable accuracy. The heat leak is the result of two heat transfer paths: the case material and the wick plug. Figure 81 shows the heat loss through the case and through the wick plug. One can see that the heat transfer through the case is larger than the power transferred by the wick plug. The

percentage difference between these parcels decreases as the power input increases. The maximum heat leakage is equivalent to 3.1 % of the power applied. However, the 2D-model temperature fields shows that the temperature difference between the maximum and vapor temperatures is below the critical difference of temperature necessary for the onset of bubbles inside the wick structure, according with the criteria proposed by Reay and Kew (2006).
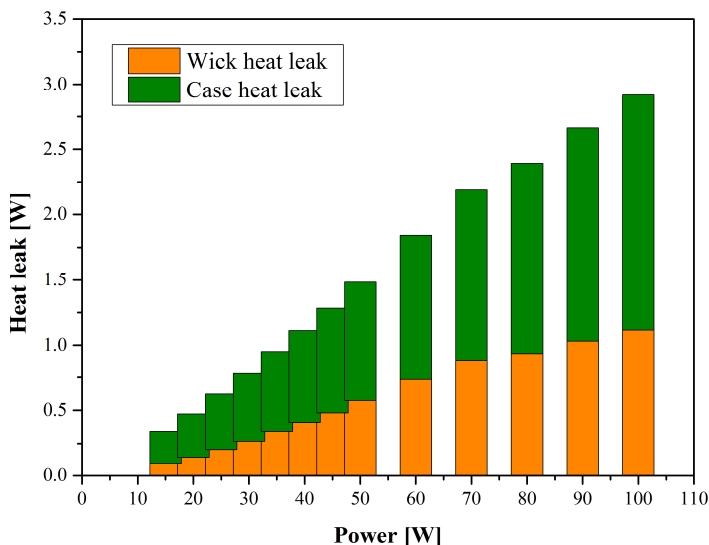
Figure 81 - Heat leaks through the case and through the wick plug (case B).

The pressure drop is other important factor that determines the operation of a LHP. The maximum heat associated to the capillary capacity is called the capillary limit, as mentioned in chapter 2. This section analyzes the pressure drop in the wick structure. In Figure 82, theoretical values of pressure drop are presented as a function of the power load. The total pressure drop was calculated for each load power, considering the properties of distillate water at 60 °C. In this figure, the capillary limit is achieved at 120 W.

In Figure 83, the total pressure drop in the wick structure is presented by three pressure drop portions. A first portion produced by the solid cylinder, identified in the 2D pressure model as subdomain 4-5. The second portion is represented by the number 6, and the third portion is due to the sum of all pressure drops through the liquid and vapor lines and condenser. From Figure 83 it can be seen that the higher pressure

drop is due to the subdomain 6, which represents 47 % of the total pressure drop for LHP studied. On the other hand, the pressure drop due to the plug and flow through the loop (condenser, liquid and vapor lines) are 16 and 37 % of the total pressure drop, respectively.
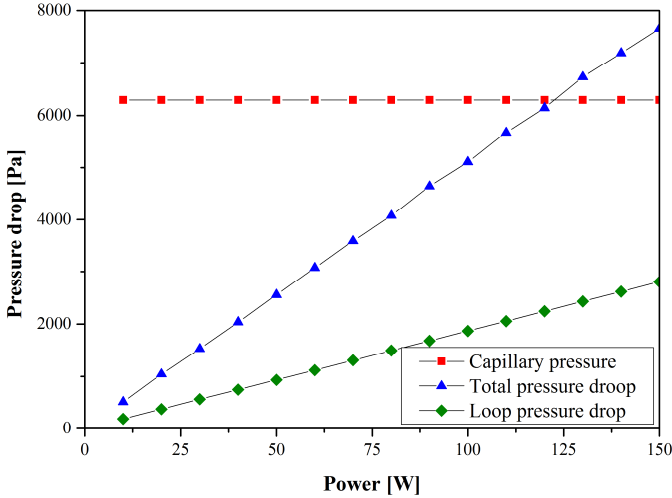
Figure 82 - Thermal behavior of the LHPs described in Table 20, operating with water (case B).
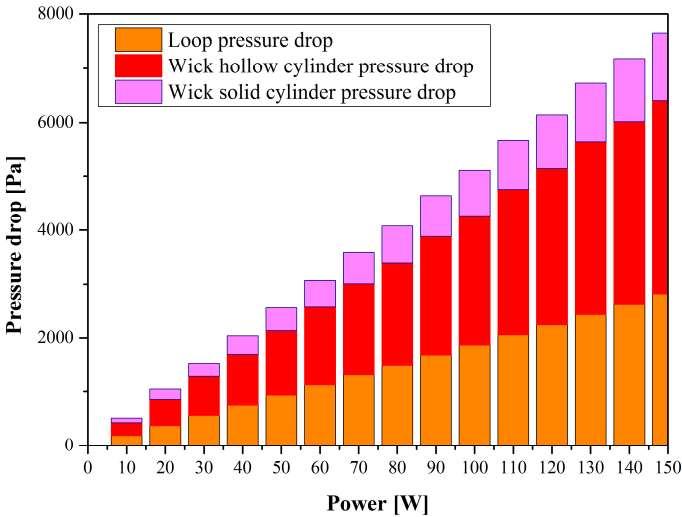
Figure 83 - Total pressure drop LHP described in Table 20, operating with water (case B).

Figure 84 shows a plot of the experimental vapor temperature corresponding to thermocouple T1 (see Figure 69) and the theoretical prediction obtained from 1D-model applied to the LHP studied (case B), against electrical power input. From this figure, one can see that the maximum temperature is 66.37 °C for an applied power of 15 W. After that, the temperature of vapor decreases gradually until a minimum value of 57 °C, for 70 W. According to Ku (1999), this behavior is called as operation under a variable conductance mode. In this power range, the temperature of the heat source remains constant, which is due to the returning liquid from condenser being subcooled enough to compensate the heat leak transferred form evaporation zone.
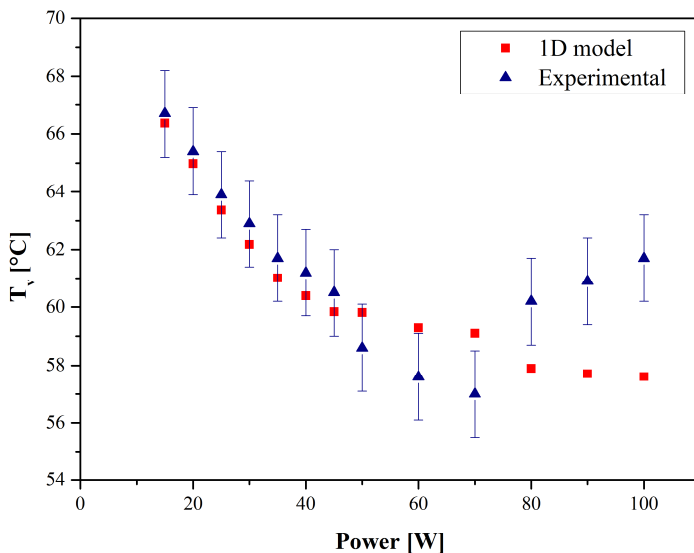
Figure 84 - Comparison between theoretical and experimental values of the LHP evaporator temperature (case B).

For heat transfer, larger than 80 W, the vapor temperature increases. However, the loop heat pipe continues operating. From this power load, the 1D mathematical model does not agree with the experimental data as well as for smaller heat loads. The smaller difference between the theoretical values and experimental data is 0.5 % for transfer rates less than 80 W, while the largest difference is of 6.63 % for heat transfer rates larger than 80 W. the LHP then operates in the constant conductance mode. From this power load, the compensation chamber

achieves its minimum temperature and the condenser is fully solicited by power applied. For this power, the temperature increases linearly with the heat load. The vapor temperature obtained using the 1D-model requires the inlet condensate temperature, which was taken from the experimental measurements of the compensation chamber, i.e., thermocouple T10 (see Figure 69). The condenser outlet temperature value predicted from the model proposed does not show variations with the increase of the heat input, as the inlet temperature was always 20 °C. Therefore, the experimental temperature outlet of condenser increased until the temperature of 25 °C, register by thermocouple 7 (see Figure 72). The heat leak to the liquid line can be explicated by the increase of the temperature of the liquid inlet to the compensation chamber (thermocouple 11, see Figure 72) that is the temperature resultant of the heat transferred by the case and wick structure evaporator. As a result, the 1D model overestimated the real heat transfer capacity of the condenser.

5.6   Condenser validation model

In of chapter 4, a model to predict the temperature distribution of the condenser based on the analogy of electrical circuit was presented. The condenser was divided into two sections, the first section with length $L^{2\phi}$ where happens the phase change and the section with length $L^{1\phi}$ where is transferred the sensible heat. The thermal model of the first section is used to determine the condenser length necessary to reject the heat in the phase change. The mathematical model of the second section allows to calculate the fluid temperature at the outlet of the condenser and to determine the heat sensible transferred. In the Figure 85, the temperature distribution for the condenser for each power load is presented. One can see that the length $L^{2\phi}$ where temperature is constant corresponds to phase change of the fluid working. In the Figure 85, the minimal and maximum length $L^{2\phi}$ were 6.67 mm and 53.8 mm for a load power of 15 and 100 W, respectively. These values represent the 2.64 % and 21.3 % of the length of the condenser. These results can be explained because the high heat transfer coefficient associated to phase change. In the Figure 85 again, one can see also that for a power load of 50 W at 150 mm of length of the condenser, the temperature of the sink was achieved. For this power level, about of 40 % of total length becomes useless. Therefore, the condenser designing can be improved, reducing its length.

In Figure 86, the experimental data of temperature corresponding to thermocouples 3, 4, 5 and 6 (see Figure 69) and the predicted temperatures by condenser model are plotted. The highest difference between the results and theoretical values was 25 % and the smallest was 3 %. The experimental temperature is higher than the predicted value by model and this difference increases after that the applied power load is higher than 50 W, but in general, one can see that the theoretical values accomplishes the behavior of the temperatures. This difference between the temperatures may be reduced using the best approximation to welding resistance, where the heat flux found a constriction. Also, the thermal conductivity of welding can be modified by impurities or trapped gas.
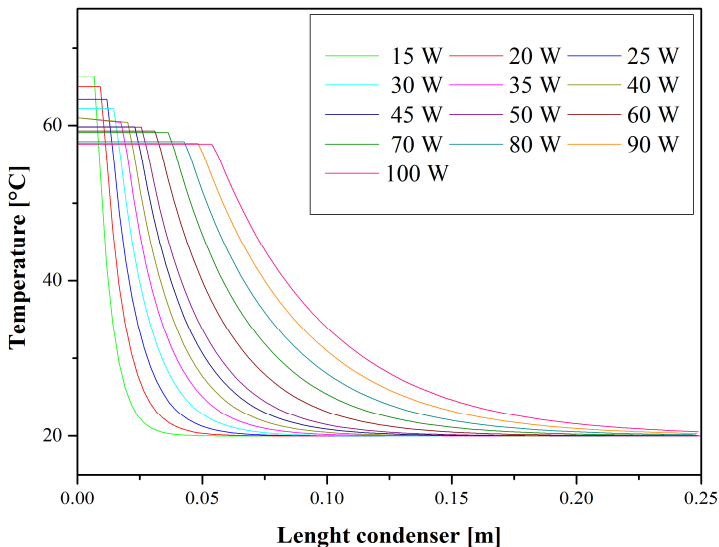
Figure 85 - Temperature distribution of the condenser against power supplied.

Figure 87 presents the thermal resistance of the studied LHP (case B) evaluated for each power applied. This thermal resistance was evaluated taking into consideration of the temperature difference between thermocouples 1 and the average temperature between thermocouples 3, 4, 5, 6, and 7 localized in the condenser. The curve shows that the thermal resistance decreases as the transferred heat power increases. The highest thermal resistance of 4 °C/W represents a non-operating

condition. On the other hand, the lowest thermal resistance observed was 0.21 °C/W. The highest difference between the experimental data and values predicted by the mathematical model was 0.09 °C/W that it is equivalent to 33 %. This thermal resistance value corresponds to power load of 70 W. For power higher than 50 W, the difference between the results and theoretical data increases. The lowest difference was of 2 %.
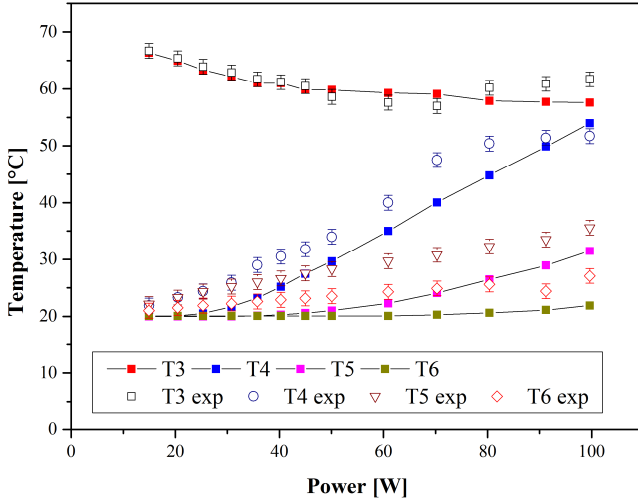
Figure 86 - Comparison between the experimental and condenser model temperatures.
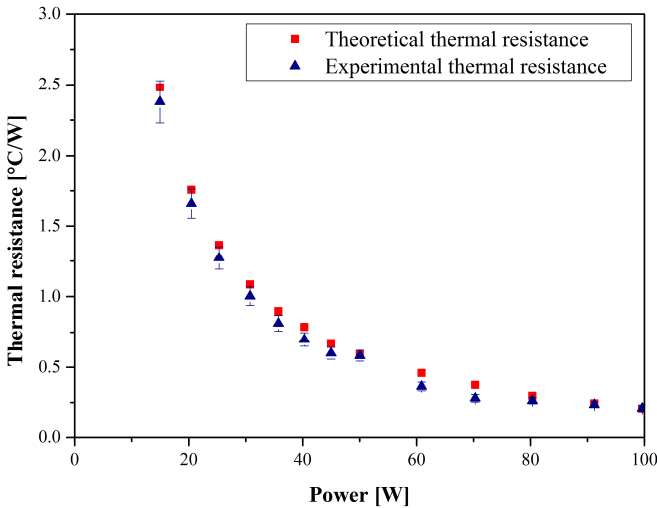
Figure 87 - LHP measured thermal resistance as a function of the power input.

5.7   Working fluid inventory

To determine the better working fluid filling ratio, case B of Table 20 was tested with several different working fluid volumes: 2.4 ml, 2.5 ml, 2.6 ml, 2.7 ml and 2.8 ml. The amount of working fluid inserted in the LHP is controlled using a graduated pipette with 0.05 ml of scale. Also, the LHP was tested for different applied heat power loads.

Table 23 presents the volumes calculated for each section of LHP fabricated (see Figure 63). These values are used in Equations (2.2) and (2.3) to calculate the filling ratio and the compensation chamber size (KU, 1999). The increase of temperature of LHP in the startup can be due to decrease of volume of compensation chamber.

Table 23. Volume of the components of LHP.

Working Fluid load of LHP	
Volume	
Volume of porous (wick structure)	1.53 ml
Evaporator vapor channel	1.09 ml
Vapor line	0.17 ml
Liquid line	0.32 ml
Condenser	0.52 ml
Compensation chamber	3.04 ml

Figure 88, Figure 89 and Figure 90 show plots of temperature (left vertical axis) and electrical power input (right vertical axis) as a function of time, for the same LHP, operating with different volumes of the working fluid (2.4, 2.6 and 2.8 ml at 25 °C, respectively). In Figure 88, one can see that the startup was reached after the application of 30 W, reaching a temperature of 65 °C, as indicated by thermocouple T1 and T2. The comparison of the performance for three filling volumes show that, for an increase of 8.3 % in the working fluid, it is observed an increase in the operation temperature by 15.4 %.

The maximum startup temperature was 77 °C for the LHP operating with a working fluid inventory of 2.8 ml. The experimental results of the Figure 88, Figure 89 and Figure 90 show an increase in the evaporator temperature when fluid inventory is increased. About 5 °C was augmented the evaporator temperature during the startup, for 0.2 ml that equivalent to 8.3 % of increase in the fluid inventory.
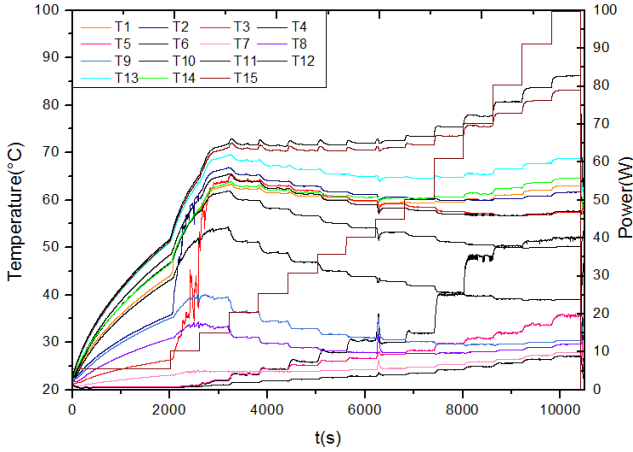
Figure 88 - Temperatures as a function of time for the LHPs described in Table 20, operating with 2.4 ml of water.
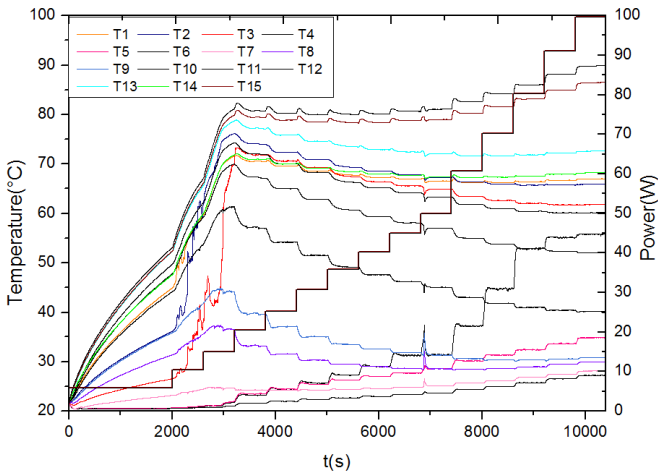
Figure 89 - Temperatures as a function of time for the LHPs described in Table 20, operating with 2.6 ml of water
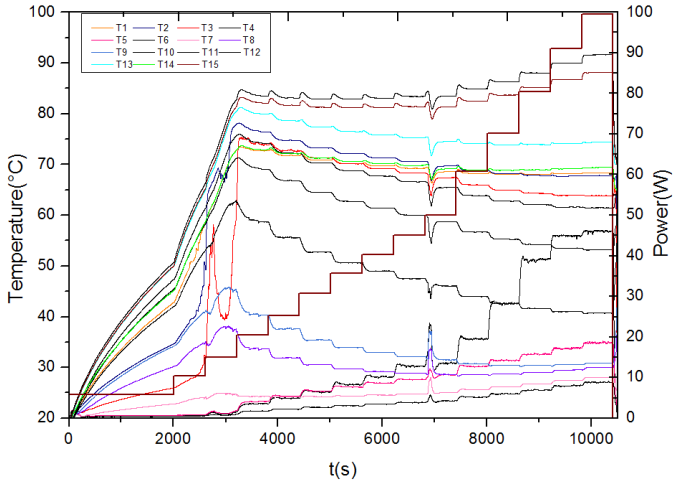
Figure 90 - Thermal behavior of the LHPs described in Table 20, operating with 2.8 ml of water

Figure 91 shows the inventory working fluid volume (in *y*-axis) against the experimental parameters α (fraction of the compensation chamber occupied by vapor) used as input parameters in the equations 2.2 (according to Ku, (1999)) for the determination of the mass of working fluid. These relations should be evaluated in two operation conditions: hot and cool condition. In Figure 91, the inventory working fluid is evaluated for 60 °C, for hot operation conditions. In the Figure 91 again, the inventory volume of working fluid that present the lowest vapor temperature is also plotted. For this inventory volume, where the LHP presented the best behavior, corresponds to a value of the experimental coefficient α = 0.8 for the hot condition (see equation (2.2)). On the other hand, this inventory of working fluid is also equivalent to 30% above of the LHP occupied by liquid volume, i.e. volume of porous wick structure plus liquid line. According to Paiva (2011) and Peterson (1994b), for HP, the fluid work inventory is approximately 10 to 20 % larger than the volume of HP that should be occupied by liquid.
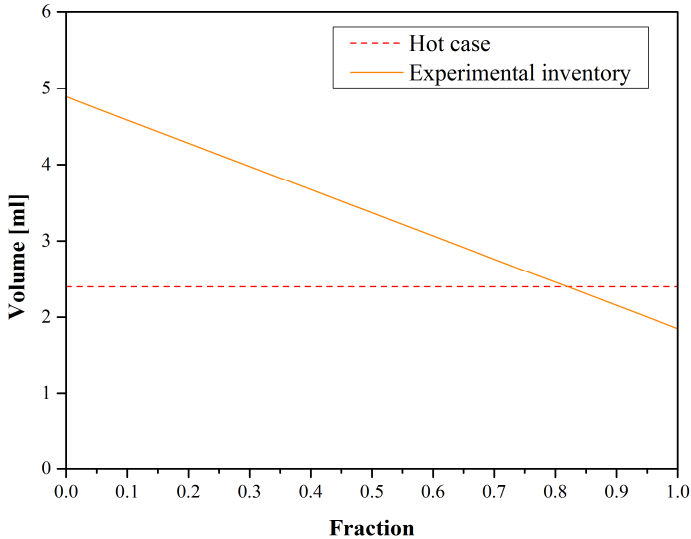
Figure 91 - Inventory working fluid model and experimental data.

5.8 Conclusions

An equation to determine a design criterion for the evaporation zone geometry was proposed and evaluate experimentally. LHP's were tested using methanol and water as working fluids and different geometries satisfy and unperformed critical criteria. Using the 2D-model, an analysis of the of thermal response to variations of the geometry parameters β and δ, regarding the temperature distribution and the heat leak inside the wick structure for the evaporator of the LHP was development. As result of this analysis, one can see that the proposed geometry presents low heat leakage and that the temperature gradient is high in the radial direction of the evaporation zone. Therefore, the wick geometry according to the case of study was modeled using a 1D approach. The experimental operation of the LHP was compared to the predicted temperature by the proposed 1D model showed good agreement. An experimental test to determine the inventory of working fluid was developed and the experimental parameter was determined and compared with other ones proposed in the literature.

6 CONCLUSIONS AND RECOMMENDATIONS FOR FUTURE WORK

In this work, several models for the prediction of the temperature and pressure distribution of the wick structure porous media, for a cylindrical shape LHP evaporator, was developed. The wick structure evaporator study in this thesis is composed by an active zone of evaporation, i.e. a hollow cylinder where heat from the heat source is transferred to surface of evaporation (meniscus) and another solid cylinder that separate the compensation chamber for evaporation zone.

For the thermal model, two approaches were applied for development of the mathematical model: two-dimensional (2D) and one dimensional (1D), while the pressure model only was approach for two-dimensional (2D). The thermal and pressure 2D model coupled allows the determination of the geometry parameters that guarantees the correct performance of the evaporator, i.e., no vapor bubble formation within the porous media. Therefore, the 2D model is a useful tool for the design of the evaporator wick structure of LHP, able to provide a safe operation mode. However, the thermal 2D model does not take into account the heat loss from the evaporator wall, but only through the wick plug. Therefore, based on the 2D results which shows a very close to a one dimensional behavior, a 1D model was developed. Although very simple, this model, which makes use of the analogy between thermal and electrical circuit, allows for accounting the heat transfer losses from the evaporator to the compensation chamber, and so, to predict the actual thermal behavior of the evaporator. The analogy between thermal and electrical circuit was also used to determine the temperature distribution along the LHP condenser. Pressure drop models to single and two phase fluid were also used in liquid and vapor lines and condenser.

The temperature and pressure fields show that the interface between the solid and hollow cylinder is the critical region to both heat and mass transfer. However, when the heat load is increased, temperatures higher than the critical ones in these regions can be reached forming vapor and reducing the transversal area heat transfer and increasing the pressure drop inside of wick structure evaporator. The procedure to evaluate the formation of bubble inside of wick structure was shown, the temperature and pressure were evaluated for a point, and it was compared with one boiling criteria to determine the formation of bobbles inside of wick structure.

Another theoretical expression for the critical parameter, which relates the thermodynamic properties of the working fluid with the thermophysical properties of the porous media, is proposed for the determination of the wick thickness of the LHP evaporator. LHP evaporator were designed and fabricated to evaluate the theoretical criterion. The LHP evaporator project to operate with methanol as working fluid attended the criteria ratio δ/l operating normally. The same LHP was tested with distilled water as working fluid without attend the critical criterion do not work. However, a second design of wick structure evaporator project to operate with water allowed to show that the equation proposed can be used as tool for design of wick LHP evaporator.

To design a wick sintered porous media, with desirable parameters (porosity, permeability, effective porous radio and effective thermal conductivity), models, where the input parameter is the mean particle diameter, were proposed. The sintering process was described using literature models. Experimental apparatus was developed to measure the thermophysical properties and the obtained data were compared with theoretical values, showing a good comparison.

A statistical analysis to determine the main effect of the geometrical parameters and effective thermal conductivity on the thermal response of a wick structure geometry proposed in this thesis was made. Two types of powders were selected to produce four different porous materials with different designs, resulting from the combination of the ratios between the parameters: δ/l and β/l. Where δ is the thickness of the wick structure in the active zone of evaporation, β is the length of bottom wick structure that separates the compensation chamber of evaporation zone and l is the length of the active zone of evaporation. ANOVA method was applied and, for a significance level of 95 %, the analyses showed that the parameters: effective thermal conductivity and ratio δ/l, in the range $\delta/l_{crit} < \delta/l < 1.2\,\delta/l$, have significant effects over the thermal response (temperature and heat leakage) of the evaporator wick.

Experimental tests with a LHP operating with different fluid inventory showed that best mass fluid inventory is related with others proposed in literature for HP. The experimental factor used to determine the inventory fluid base and the compensation chamber dimensions was also determined.

Future Works

From the analyses presented in this thesis, the following future works are proposed:

- To analyze the thermal and pressure criteria based on the powder diameter for the onset of vapor formation at the interface of coupling of the domains 2 and 3. The literature criteria to evaluate the bubble formation in sintered porous media are correlations that use parameters with a wide range.

- To determine the optimal geometry parameters based on the 2D and 1D models proposed in this work. The entropy generation approach can be used as the objective function in an optimization process. The present study provides the temperature and pressure drop to determine the optimal geometry.

- To develop a 2D model for the heat and mass transfer in the transient regime. The start up in the loop heat pipe becomes difficult for low power. A transient modeling can be obtained from the present work, adding the transient term of the energy conservation equation.

- To study the thermophysical properties for several combinations of powder materials with two different average particle diameters. In this work the equation development for thermophysical properties of sintered porous media was based on the average particle diameter. Other system considering the mixture of two particle diameters can be tested, in order to improve its properties.

- To conduct an analytical and/or numerical study of a porous media with two layers with different geometries (porosity permeability, etc.) and effective thermal conductivities. The results should be compared with data resulting from an experimental study.

REFERENCES

AKBARI, M; SISTON, D.; BAHRAMI, M. Laminar Fully Developed Flow in Periodically Converging-Diverging Microtubes. **Heat Transfer Engineering** v. 31, n. 8, p. 628–634, 2010.

ALEXANDER, E. J. Jr. **Structure–property relationships in heat pipe wicking materials**. Ph.D. thesis – North Carolina State University, United States, 1972.

ARPACI, Vedat S.; LARSEN, Poul Scheel. **Convection heat transfer**. [S.l.]: Prentice Hall, 1984. 490 p.

ASHBY, M. F. A First Report on Sintering Diagrams. **Acta Metallurgica** v. 29, p. 275–289, 1981.

ASM. **Properties and Selection: Nonferrous Alloys and Special-Purpose Materials**. [S.l.]: Metals Handbook, 1990. 9 v.

ATABAKI, N.; BALIGA, B. R. Effective thermal conductivity of water-saturated sintered powder-metal plates. **Heat and Mass Transfer** v. 44, p. 85–99, 2007.

BAHRAMI, Majid; YOVANOVICH, M. M.; CULHAM, J. Richard. Effective Thermal Conductivity of Rough Spherical Packed Beds. **International Journal of Heat and Mass Transfer,** 2006.

BAHRAMI, M.; YOVANOVICH, M. M.; CULHAM, J. R. Pressure Drop of Fully-Developed, Laminar Flow in Microchannels of Arbitrary Cross-Section. **Journal of Fluids Engineering** v. 128, n. 5, p. 1036, 2006.

BEJAN, Adrian. **Convection Heat Transfer**. 4. ed. New Jersey: John Wiley and Sons, 2013.

BIRNBOIM, Amikam; OLORUNYOLEMI, Tayo; CARMEL, Yuval. Calculating the thermal conductivity of heated powder compacts. **Journal of the American Ceramic Society** v. 84, n. 6, p. 1315–1320, 2001.

BYON, C.; KIM, S.J. Permeability of mono and bi-dispersed porous media. **EPJ Web of Conferences** v. 45, p. 1018, 2013.

CAO, Yiding; FAGHRI, Amir. Analytical solutions of flow and heat transfer in a porous structure with partial heating and evaporation on the upper surface. **International Journal of Heat and Mass Transfer** v. 37, n. 10, p. 1525–1533, 1994.

CAREY, V. P. **An Introduction to the Thermophysics of Vaporization and Condensation Processes in Heat Transfer Equipment.** 2. ed. [S.l.]: Taylor & Francis, 2007. 645 p.

CARSON, J. K. *et al.* An analysis of the influence of material structure on the effective thermal conductivity of theoretical porous materials using finite element simulations. **International Journal of Refrigeration** v. 26, n. 8, p. 873–880, 2003.

CENGEL, Yunus; BOLES, Michael. **Thermodynamic: an Egineering Approach**. 5. ed. Chicago: The McGraw-Hill Companies, 2006.

CHATO, J. C. **ASHRAE J. Laminar Condensation Inside Horizontal and Inclined Tubes.** [S.l: s.n.], 1962. 52-60 p. 4 v.

CHERNYSHEVA, Mariya A.; MAYDANIK, Yu. 3D-Model for Heat and Mass Transfer Simulation in Flat Evaporator of Copper-Water Loop Heat Pipe. **Applied Thermal Engineering,** 2012.

CHISHOLM, D. Pressure gradients due to friction during the flow of evaporating two-phase mixtures in smooth tubes and channels. **International Journal of Heat and Mass Transfer** v. 16, n. 2, p. 347–358, 1973.

CHURCHILL, Stuart W.; CHU, Humbert H.S. Correlating equations for laminar and turbulent free convection from a vertical plate. **International Journal of Heat and Mass Transfer** v. 18, n. 11, p. 1323–1329, 1975.

COOKE, A. J.; ROWE, R. K. Extension of Porosity and Surface Area Models for Uniform Porous Media. **Journal of Environmental Engineering,** p. 126–136, 1999.

DEMIDOV, A. S.; YATSENKO, E. S. Investigation of Heat and Mass Transfer in the Evaporator Zone of a Heat Pipes Operating by Inverted Meniscus Principle. **International Journal of Heat and Mass Transfer** v. 37, n. 14, p. 2155–2163, 1994.

DUNN, Peter; REAY, David. **Heat Pipes**. 2. ed. New York: Pergamon Press, 1978.

DYBBS, A.; EDWARDS, R. V. A New Look at Porous Media Fluid Mechanics—Darcy to Turbulent. **Fundamentals of Transport Phenomena in Porous Media**. [S.l.]: Bear and Corapcioglu, 1984. p. 199–254.

ENDO, Yoshiyuki *et al*. Analysis of fluid permeation through a particle-packed layer using an electric resistance network as an analogy. **Powder Technology** v. 191, n. 1–2, p. 39–46, 2009.

FAGHRI, Amir. **Heat Pipes Science and Technology**. Washingon USA: Taylor and Francis Group, 1995.

FLOREZ, Juan Pablo M.; MANTELLI, Marcia B. H.; NUERNBERG, Gustavo G. V. Effective Thermal Conductivity of Sintered Porous Media: Model and Experimental Validation. **International Journal of Heat and Mass Transfer** p. 868–878, 2013.

FLOREZ, Juan Pablo M.; NUERNBERG, Gustavo G. V.; PAIVA, Kleber. Multilayer Sintered Porous Media Mini Heat Pipe. In: PROCEEDINGS OF 16TH INTERNATIONAL CONFERENCE, 2012, Lyon, France. **Anais**... Lyon, France: [s.n.], 2012.

FOX, Robert; MCDONALD, Alan. **Introduction to Fluid Mechanics**. 5. ed. New Delhi: John Wiley and Sons, 2001.

FRIEDEL, L. Improved friction pressure drop correlations for horizontal and vertical two-phase pipe flow. 1979, Ispra. **Anais**... Ispra: [s.n.], 1979. p. Paper E2.

FRIEDEL, L. Pressure drop during gas/vapor–liquid flow in pipes. 3. v. 20, p. 352–367, 1980.

GENNES, Pierre-Gilles de; BROCHARD-WYART, Françoise; QUÉRÉ, David. **Capillary and Wtting Phenomena: Drops, Bubbles, Pearls, Waves**. [S.l.]: Springer, 2004.

GERMAN, Randall. **Particle Packing Characteristics**. New Jersey: Metal Powder Industries Federation, 1989.

HOLLEY, Brian; FAGHRI, Amir. Permeability and effective pore radius measurements for heat pipe and fuel cell applications. **Applied Thermal Engineering** v. 26, n. 4, p. 448–462, 2006.

HSU, Y. Y. On the Size Range of Active Nucleation Cavities on a Heating Surface. **Journal of Heat Transfer** v. 84, n. 3, p. 207–213, 1962.

INMETRO. **Avaliação de dados de medição: Guia para a expressão de incerteza de medição - GUM 2008**. Duque de Caxias, RJ: INMETRO/CICMA/SEPIN, 2012. 141 p.

KANDLIKAR, Satish *et al.* **Heat transfer and fluid flow in minichannels and microchannels**. [S.l.]: elsevier, 2005.

KANG, Suk-Joong. **Sintering Densification Grain, Growth and Microstructure**. Oxford - UK: Butterworth-Heinemann Elsevier, 2005.

KAVIANY, Massoud. **Principles of Heat Transfer in Porous Media**. 2. ed. New York: Springer, 1995.

KAYA, T. *et al.* Mathematical Modeling of Loop Heat Pipes. 1999.

KU, Jentung. Operating Characteristic of Loop Heat Pipes. 1999.

LAUNAY, Stéphane; SARTRE, Valérie; BONJOUR, Jocelyn. Analytical Model for Characterization of Loop Heat Pipes. **Journal of Thermophysics and Heat Transfer** v. 22, n. 4, p. 623–631, 2008.

LAWLEY, Alan. **Atomization: The Production of Metal Powders**. Princeton, New Jersey: Metal Powder Industries Federation, 1992.

LI, J; PETERSON, G.P. 3D Heat Transfer Analyses in a Loop Heat Pipe Evaporator with a Fully Saturated Wick. **International Journal of Heat and Mass Transfer** p. 564–574, 2011.

LI, Jinwang; ZOU, Yong; CHENG, Lin. Experimental study on capillary pumping performance of porous wicks for loop heat pipe. **Experimental Thermal and Fluid Science** v. 34, n. 8, p. 1403–1408, 2010.

LOCKHART, R. W.; MARTINELLI, R. C. Proposed Correlation of Data for Isothermal Two Phase Flow, Two Component Flow in Pipes. **Chemical Engineering Process** v. 45, p. 39–48, 1949.

MAYDANIK, Yu. *et al.* Investigation of a Compact Copper-Water Loop Heat Pipe with a Flat Evaporator. **Applied Thermal Engineering** p. 3533–3541, 2011a.

MAYDANIK, Yu. *et al.* Investigation of Compact Copper-Water Loop Heat Pipes with a Flat Evaporator. **Applied Thermal Engineering** p. 3533–3541, 2011b.

MONTGOMETY, Douglas. **Design and Analysis of Experiments**. 3. ed. Canada: John Wiley and Sons, 1991.

NGO, Ich-Long; BYON, Chan. Permeability of microporous wicks with geometric inverse to sintered particles. **International Journal of Heat and Mass Transfer** v. 92, p. 298–302, 2016.

PAIVA, Kleber Vieira de. **Desenvolvimento de novas tecnologias para minitubos de calor: análise teórica e experimental**. Doctoral degree thesis – Federal University of Santa Catarina, 2011.

PAIVA, K.V.; MANTELLI, M.B.H. Wire-plate and sintered hybrid heat pipes: Model and experiments. **International Journal of Thermal Sciences** v. 93, p. 36–51, 2015.

PALAKURTHI, Nikhil Kumar *et al.* Micro-scale simulation of unidirectional capillary transport of wetting liquid through 3D fibrous porous media: Estimation of effective pore radii. **International Journal of Multiphase Flow** v. 77, p. 48–57, 2015.

PETERSON, G.P. **An Introduction to Heat Pipes. Mdeling, Testing and Applications**. New York: Wiley Interscience, 1994a.

PETERSON, G.P. **An Introduction to Heat Pipes. Mdeling, Testing and Applications**. New York: Wiley Interscience, 1994b.

POULIKAKOS, Dimos. **Conduction Heat Transfer**. First ed. New Jersey: Prentice Hall, 1994.

REAY, D. A.; KEW, P. A. **Heat Pipes: Theory, Design and Applications**. 5. ed. Burlington, MA: Elsevier, 2006. 384 p.

SANTOS, Paulo Henrique Dias dos. **Theoretical and Experimental Study of the Application of Ceramic Porous Wick in the LHP and CPL**. Doctoral degree thesis – Federal University of Santa Catarina, Brazil, 2010.

SIEDEL, Benjamin; SARTRE, Valérie; LEFÈVRE, Frédéric. Complete Analytical Model of Loop Heat Pipe with a Flat Evaporator. **International Journal of Thermal Sciences** v. 89, p. 372–386, 2005.

SINGH, Randeep *et al.* Theoretical modelling of miniature loop heat pipe. **Heat and Mass Transfer** v. 46, n. 2, p. 209–224, 2009.

SINGH, Randeep; AKBARZADEH, Aliakbar; MOCHIZUKI, Masataka. Experimental Determination of Wick Properties for Loop Heat Pipe Applications. v. 12, n. 8, p. 759–776, 2009.

SWINKELS, F. B.; ASHBY, M. F. A second report on sintering diagrams. **Acta Metallurgica** v. 29, n. 2, p. 259–281, 1981.

TANG, Yong *et al.* Effect of fabrication parameters on capillary performance of composite wicks for two-phase heat transfer devices. **Energy Conversion and Management** v. 66, p. 66–76, 2013.

THUMMLER, Fritz; OBERACKER, R. **An introduction to Powder Metallurgy**. Ann Arbor: Institute of Materials, 1993.

YANG, Xiaohu; LU, Tian Jian; KIM, Tongbeum. An analytical model for permeability of isotropic porous media. **Physics Letters A** v. 378, n. 30–31, p. 2308–2311, 2014.

YOVANOVICH, M. Michael; SCHEIDER, G. E.; TIEN, C. H. Thermal Resistance of Hallow Spheres Subjected to Arbitrary Flux Over Their Poles. In: 2ND AIAA/ASME THERMOPHYSICS AND HEAT TRANSFER CONFERENCE, 1978, Palo Alto, California. **Anais**... Palo Alto, California: [s.n.], 1978. p.120–134.

APPENDIX A. MEASUREMENT UNCERTAINTIES

The measurement result is composed by a base result and an uncertainty. The measurement uncertainties were determined according to INMETRO (2012). The uncertainties are classified as standard uncertainties type A and standard uncertainties type B. The standard uncertainties of type A are the uncertainties calculated from a group of observations or replications of the measurements. The standard uncertainties of type B are not obtained from observations replicated. They are based on the available information about the variables measured such as, previous measurements, the manufacturer's specifications or data supplied in calibration certificates. In this work, for all variables measured, standard uncertainty type B was considered, using the information available from the equipment manuals.

The standard uncertainty type B of a variable x, $u_B(x)$, is estimated considering the equipment measurement chain. For its calculation, all sources of uncertainty $u_i(x)$ involved in the measurement chain (repeatability, equipment resolution, acquisition system, etc.) were combined as shown in Equation (A.1).

$$u_B^2(x) = u_1^2(x) + u_2^2(x) + \cdots + u_i^2(x) \tag{A.1}$$

The equation above was used for directly measured variables, such as the temperature. When the variables were indirectly measured from other parameters, such as heat flux, the combined standard uncertainty was obtained through the following equation:

$$u_c^2(f) = \sum_{i=1}^{N} \left[\frac{\partial f}{\partial x_i}\right]^2 u^2(x_i) \tag{A.2}$$

where f represents the variable under interest, defined as a function of the variables x_i and $u(x_i)$ are the standard uncertainties of each variable x_i.

The combined uncertainty of each variable must be multiplied by a coverage factor k_p (corresponding to t-Student coefficient) in order to obtain the expanded uncertainty U. The expanded uncertainty is the interval where, for a defined probability, one expects to find the aleatory error component of the measurement process. The coverage factor k_p is an expansion interval of the combined uncertainty, corresponding with the level of probability of the t-Student distribution.

In this thesis, a confidence interval of 95.45 % was used for the calculation of the expanded uncertainty, obtained from the following equation:

$$U(x) = k_p u_c(x) \qquad (A.3)$$

The coverage factor k_p depends on the number of degrees freedom resultant from the combined standard uncertainty. In this work, the standard uncertainty type B of the different variables was considered with infinity degrees freedom. Therefore, for a t-Student distribution with confidence interval of 95.45 % and infinity degrees freedom, the coverage factor is $k_p = 2$. This value was considered for the calculation of the expanded uncertainty of all the variables tested.

The specified information about the uncertainty calculated for each variable tested is presented in the following sections.

A.1. Uncertainty of the temperature

The temperature measurement chain is composed by a Type T (copper-constantan) thermocouple with 0.07 mm diameter connected to a data acquisition system and an extension wire that sends the signal from the data acquisition system to a computer. The temperature readings are processed by LabVIEW 8.6. The summary of the uncertainties involved in the measurement of the temperature is presented in the Table A.1

Table A3. Uncertainties of the temperature measurement chain.

Symbol	Source of uncertainty type B	Value	Distribution	u_i (±)
	Thermocouple Type T	± 1 °C	Rectangular (68 %)	0.577 °C
T	Acquisition data system	± 0.77 °C	Rectangular (68 %)	0.445 °C
	Resolution	± 0.1 °C	Rectangular (68 %)	0.057 °C
u_T	Combined standard uncertainty			0.73 °C
U_T	Expanded uncertainty		t-student (95.45 %)	1.46 °C

The combined standard uncertainty was calculated from the following equation:

$$u_T = \sqrt{u_{thermocouple}^2 + u_{data\ logger}^2 + u_{resolution}^2} \qquad \text{(A.4)}$$

A.2 Uncertainty of the length

The uncertain associated to the measurement of the samples length, when calculating properties such as permeability and effective thermal conductivity were calculated from the caliper uncertainty. According to the manufacturer, the resolution is 0.01 mm. The uncertainty associated to the temperature variations was also calculated, considering an expansion coefficient for stainless steel α = 11.5 µm/m·K at 20 ± 10 °C. The summary of the uncertainty calculated is presented in the Table A.2

Table A4. Uncertainty of length measurement.

Symbol	Source of uncertainty type B	Value	Distribution	u_i (±)
	Error limit from manufacturer	± 0.01 mm	Rectangular (68 %)	5.77 µm
	Resolution	± 0.01 mm	Rectangular (68%)	5.77 µm
	Thermal dilatation	ΔT = 10 °C	Rectangular (68%)	1.16 µm
u_L	Combined standard uncertainty			8.24 µm
U_L	Expanded uncertainty		t-student (95.45 %)	± 16.48 µm

The combined standard uncertainty was calculated from the following equation:

$$u_{TL} = \sqrt{u_{caliper}^2 + u_{resolution}^2 + u_{thermal\ dilatation}^2} \qquad \text{(A.5)}$$

A.3 Uncertainty of the mass

The uncertainty of mass measurement was calculated from the weighing scale uncertainty. According to the manufacturer, the resolution is 0.1 g. A rectangular distribution was considered for the uncertainly of the resolution. The uncertainly of the repeatability was calculated for 15 measures. The summary of the uncertainty calculated is presented in the Table A.3.

Table A5. Uncertainty of the mass measurement.

Symbol	Source of uncertainty type B	Value	Distribution	u_i (±)
	Resolution	± 0.1 g	Rectangular (68%)	0.029 g
	Repeatability	± 0.1 g	-	0.026 g
u_m	Combined standard uncertainty			0.039 g
U_m	Expanded uncertainty		t-student (95.45 %)	0.078 g

The combined standard uncertainty was calculated from the following equation:

$$u_m = \sqrt{u_{repeatability}^2 + u_{resolution}^2} \qquad (A.6)$$

A.4 Uncertainty of the pressure

For the permeability measurements, a digital manometer Zürich-Z10B was used. The uncertainty of the pressure measurements was calculated from the resolution of the display: 100 Pa. A pressure sensor (Omega PX409-015DWUV) was used to measure the gas pressure for the measurements of effective porous radius. The uncertainty calculated for this equipment was 210 Pa.

A.5 Uncertainty of the effective thermal conductivity

The effective thermal conductivity is calculated from other physical quantities, such as temperature, heat flux, cross area and length. Therefore, in order to determine the combined standard uncertainly of the effective thermal conductivity, the following equation was employed:

$$
U_{k_e} = \left[\left(\frac{\partial k_e}{\partial Q} \right)^2 (u_q)^2 + \left(\frac{\partial k_e}{\partial T} \right)^2 (u_T)^2 \right.
$$
$$
\left. + \left(\frac{\partial k_e}{\partial l} \right)^2 (u_l)^2 + \left(\frac{\partial k_e}{\partial A} \right)^2 (u_A)^2 \right]^{1/2}
$$

(A.7)

where K_{eff} is the effective thermal conductivity, u_q, u_T, u_l e u_A are the standard uncertainty for each quantity measured, i.e., heat flux, temperature, length and cross area of the sample, respectively. The following equation was presented by Florez *et al.* (2013) to determine the effective thermal conductivity from the comparative method.

$$
k_{eff} = \frac{l}{\Delta T A} \left[\bar{Q} - \Delta T \left(\frac{1}{R_1} + \frac{1}{R_2} \right) \right]
$$

(A.8)

The term within parentheses in the equation above is assumed as constant and negligible for the uncertainty. The combined uncertainty for the temperature and the length are shown in the Tables A.1 and A.2, respectively. The heat flux uncertainty was calculated from difference between the maximum heat flux measurement in the heat flux meter and the average heat flux.

The cross area of the sample is calculated from the following equation:

$$
A_t = WH
$$

(A.9)

where W and H are the dimensions used to calculate the cross area of the sample. By calculating the partial derivate of Equation (A.9) and substituting into Equation (A.2), one obtains the following equation to determine the combined uncertainty of the cross area.

$$
\partial A_t = [(H)^2 (u_W)^2 + (W)^2 (u_W)^2]^{1/2}
$$

(A.10)

In relation to the measurement made by the thermal conductivity analyzer C-thermal Tci, the manufacturer reports 5 % of the experimental value as uncertainty of the effective thermal conductivity.

A.6 Uncertainty of the thermal resistance of power input

This section presents the procedure to calculate the uncertainty of the thermal resistance of the loop heat pipes tested and the uncertainty of the power input.

From the following equation:

$$R_t = \frac{\bar{T}_{eva} - \bar{T}_{cond}}{P_e} \tag{A.11}$$

Therefore, the combined standard uncertainty of the thermal resistance is calculated as:

$$U_{R_t} = \left[\left(\frac{\partial R_t}{\partial \bar{T}_{eva}} \right)^2 (u_{\bar{T}_{eva}})^2 + \left(\frac{\partial R_t}{\partial \bar{T}_{cond}} \right)^2 (u_{\bar{T}_{cond}})^2 \right.$$
$$\left. + \left(\frac{\partial R_t}{\partial P_e} \right)^2 (u_{P_e})^2 \right]^{1/2} \tag{A.12}$$

where R_t is the thermal resistance of LHP, P_e is the power input, $\bar{T}_{eva}$ e $\bar{T}_{cond}$ are the average temperature in the evaporator and condenser, respectively, $u_{\bar{T}_{eva}}, u_{\bar{T}_{cond}}$ e u_{P_e} are the combined uncertainties, associated to the average temperatures and the power supplied by the cartridge heaters.

The power input is defined as:

$$P_e = Vi \tag{A.13}$$

where V is the voltage and i is the current. The combined standard uncertainty of power input is calculated as:

$$u_{P_e} = \left[\left(\frac{\partial P_e}{\partial V} \right)^2 (u_V)^2 + \left(\frac{\partial P_e}{\partial i} \right)^2 (u_i)^2 \right]^{1/2} \tag{A.14}$$

The voltage uncertainty u_V and the current uncertainty u_i were considered as the lowest division of the display of power source. The voltage uncertainty was 0.1 V and the current uncertainty was 0.01 A.